Analog MIMO spatial filtering

Citation for published version (APA):
Heuvel, van den, J. H. C. (2012). *Analog MIMO spatial filtering*. [Phd Thesis 2 (Research NOT TU/e / Graduation TU/e), Electrical Engineering]. Technische Universiteit Eindhoven. https://doi.org/10.6100/IR724476

DOI:
10.6100/IR724476

Document status and date:
Published: 01/01/2012

Document Version:
Publisher’s PDF, also known as Version of Record (includes final page, issue and volume numbers)

Please check the document version of this publication:

- A submitted manuscript is the version of the article upon submission and before peer-review. There can be important differences between the submitted version and the official published version of record. People interested in the research are advised to contact the author for the final version of the publication, or visit the DOI to the publisher's website.
- The final author version and the galley proof are versions of the publication after peer review.
- The final published version features the final layout of the paper including the volume, issue and page numbers.

Link to publication

General rights
Copyright and moral rights for the publications made accessible in the public portal are retained by the authors and/or other copyright owners and it is a condition of accessing publications that users recognise and abide by the legal requirements associated with these rights.

- Users may download and print one copy of any publication from the public portal for the purpose of private study or research.
- You may not further distribute the material or use it for any profit-making activity or commercial gain
- You may freely distribute the URL identifying the publication in the public portal.

If the publication is distributed under the terms of Article 25fa of the Dutch Copyright Act, indicated by the “Taverne” license above, please follow below link for the End User Agreement:

www.tue.nl/taverne

Take down policy
If you believe that this document breaches copyright please contact us at:

openaccess@tue.nl

providing details and we will investigate your claim.

Download date: 04. Oct. 2023

Analog MIMO Spatial Filtering

Johannes Henricus Cornelus van den Heuvel

Samenstelling promotiecommissie:

voorzitter	
prof.dr.ir A.C.P.M. Backx	Technische Universiteit Eindhoven
promotoren	
prof.dr.ir. P.G.M. Baltus	Technische Universiteit Eindhoven
prof.dr.ir. J.P.M.G. Linnartz	Technische Universiteit Eindhoven Philips Research Eindhoven
leden	
prof. D. Čabrić	University of California, Los Angeles
prof.dr.ir. L. van der Perre	Katholieke Universiteit Leuven Imec
prof.dr.ir. B. Nauta	Universiteit Twente
prof.dr.ir. C.H. Slump	Universiteit Twente
prof.dr.ir. A.H.M. van Roermund	Technische Universiteit Eindhoven

A catalogue record is available from the Eindhoven University of Technology Library.

CIP-DATA LIBRARY TECHNISCHE UNIVERSITEIT EINDHOVEN

Analog MIMO Spatial Filtering / by Johannes Henricus Cornelus van den Heuvel.
- Eindhoven: Technische Universiteit Eindhoven, 2012.
Proefschrift. - ISBN 978-94-6191-123-0
NUR 959
Subject headings: Spatial filters / Array signal processing / Interference suppression / Radiofrequency integrated circuits / MIMO systems / Cognitive Radio / Power demand / Wireless communication / Analog-digital conversion / OFDM modulation.

This research is supported by IOP Generic Communication - Senter Novem program.

Analog MIMO Spatial Filtering

PROEFSCHRIFT

ter verkrijging van de graad van doctor aan de
Technische Universiteit Eindhoven, op gezag van de
rector magnificus, prof.dr.ir. C.J. van Duijn, voor een
commissie aangewezen door het College voor
Promoties in het openbaar te verdedigen
op woensdag 11 januari 2012 om 16.00 uur

door

Johannes Henricus Cornelus van den Heuvel

geboren te Oss

Dit proefschrift is goedgekeurd door de promotoren:

prof.dr.ir. P.G.M Baltus
en
prof.dr.ir. J.P.M.G. Linnartz

Aan Petra, mijn zus, ouders, grootouders en familie

Contents

6 Analog Spatial Filtering in Wideband Cognitive Radio 119

Abbreviations

ACMM	analog complex matrix multiplier
ADC	analog-to-digital converter
AGC	automatic gain control
AOA	angle of arrival
AWGN	additive white Gaussian noise
BB	baseband
BPSK	binary phase shift keying
CMOS	complementary metaloxide semiconductor
CR	cognitive radio
DAC	digital-to-analog converter
dB	decibel
DR	dynamic range
DSP	digital signal processing
DSP	digital signal processor
ENOB	effective number of bits
EFOM	effective figure of merit
FFT	fast Fourier transform
FOM	figure of merit
I	in-phase component
IC	integrated circuit
IEEE	Institute of Electrical and Electronic Engineers
IF	intermediate frequency
IFFT	inverse fast Fourier transform
LAN	local area network
LNA	low noise amplifier

LO	local oscilator
LOS	line-of-sight
LTE	long term evolution
MIMO	multiple-input and multiple-output
MPCO	minimum power cascade optimization
MRC	maximum ratio combining
MTCO	maximum throughput cascade optimization
NLOS	non-line-of-sight
OFDM	orthogonal frequency division multiplexing
PCB	printed circuit board
PLL	phased locked loop
Q	quadrature component
RF	radio frequency
RX	receiver
SD	secure digital
SDHC	secure digital high capacity
SDXC	secure digital extended capacity
SISO	single-input and single-output
SIT	structure independent transform
SPI	serial peripheral interface
SVD	singular value decomposition
TX	transmitter
VGA	variable gain amplifier
VGA	video graphics array
WB	wide band
WiMAX	worldwide interoperability for microwave access
WLAN	wireless local area network
WRAN	wireless regional area network

List of Symbols

Symbol	**Description**	**Unit**
a	complex constant	
$\mathbf{A}$	complex valued matrix	
b_{ADC}	number of ADC bits	
$\mathbf{b}$	complex valued vector	
B	bandwidth containing both negative and positive frequencies	Hz
c	the speed of light in vacuum 3×10^8	m/s
C	capacity	b/s/Hz
C	capacitor	F
CIR	carrier-to-interference ratio	dB
d	distance	m
e	base of natural logarithm e= 2.7183	
f	frequency	Hz
f_c	carrier frequency	Hz
f_s	sample frequency	Hz
F	noise factor	
$\widehat{F}$	power optimal F	
G	gain	dB
$\mathbf{H}$	complex channel-gain matrix	
i	the imaginary number $\sqrt{-1}$	
$\mathbf{I}$	identity matrix	
ICR	interference-to-carrier ratio	dB
Idd	supply current	A
$IIP3$	input referred third order intercept point	dBm

$IP3$	input referred third order intercept point	dBm
$\widehat{IP3}$	power optimal $IP3$	dBm
k	Boltzmann's constant 1.38×10^{-23}	J/K
k	an integer	
K	an integer	
m	an integer	
M	an integer	
$\mathbf{M}$	complex valued matrix	
n	an integer	
$\mathbf{n}$	complex AWGN vector	
N	an integer	
N	noise power	W
NF	noise figure	dB
N_r	number of receive antennas	
N_t	number of transmit antennas	
$OIP3$	output referred third order intercept point	dBm
P	power	Watt
P_r	receiver circuit power	W
R	resistor	Ω
$r(t)$	output signal in the time domain	
$\mathbf{r}$	output signal in the frequency domain	
r	complex constant	
ρ	signal-to-noise ratio	dB
S	received signal power	Watt
S	scattering matrix	
$s(t)$	signal in the time domain	
$\mathbf{s}$	signal in the frequency domain	
SNR	signal-to-noise ratio	dB
SNDR	signal-to-noise-and-distortion ratio	dB
t	time	s
$t_1 ... t_{10}$	short training symbols	
T	a time interval	s
T	absolute temperature	K
T	throughput	b/s/Hz
$\widehat{T}$	maximized T	b/s/Hz

T_1, T_2	long training symbols	
T_{Symbol}	symbol time	s
$\mathbf{U}$	complex valued matrix	
$\mathbf{V}$	complex valued matrix	
Vdd	supply voltage	V
$x(t)$	italic: signal in the time domain	
$\mathbf{x}$	bold: signal in the frequency domain	
$\mathbf{X}$	bold capital: complex valued matrix	
α	a constant	
κ_t	technology constant	
κ_m	power linearity factor	
λ	a constant	
λ	wavelength	m
λ_c	carrier wavelength	m
ω	frequency	rad/s
π	3.14159	
σ	a constant	
τ	a delay time	s
θ	angle	rad
ϕ	phase	^{o}

Chapter 1

Introduction

Modern mobile telecommunication systems have allowed for almost complete freedom of communication. One can communicate almost anything (speech, text, videos, photos, books, etcetera) to virtually anyone, from virtually everywhere to anywhere. This freedom of communication has spurred a revolution in the way people communicate and has contributed to the enormous growth in the amount of information communicated worldwide via telecommunication systems. The need for an ever increasing data rate has resulted in an increase in the number of transmit and receive antennas per mobile user. Where until recently there was one transmit and one receive antenna per individual user, recent communication systems, such as for WLAN IEEE 802.11n and for mobile phones LTE-Advanced, consist of multiple transmit and multiple receive antennas per individual user. Next to an increase in the number of antennas, also the total number of users has increased over time. Due to the increase in the number of users, users are increasingly interfering with one another. The challenges associated with multiple antenna systems and interference mitigation are the main topics of the research presented in this thesis. The mathematical foundation of the theory of communication systems was laid by Claude E. Shannon in 1948 [1]. This work has remained the fundamental theory of communication until this day. In 1998-1999 the theory of wireless communication systems was expanded to include multiple-input multiple-output (MIMO) systems by Telatar [2], and Foschini and Gans [3]. The theory of wireless communication systems tells us the upper bound of what is achievable. However, the theory does not tell us the required effort to attain a communication system that operates near that upper bound.

The research presented in this thesis contains theoretical system modeling considering arguments based on Shannon capacity, and a partial system implementation used for verification of the theory. The system implementation consists of algorithm design, PCB design, and circuit design and implementation in 65 nm CMOS. To obtain a joint optimization of both the radio frequency (RF) front end and the baseband (BB) digital signal processing (DSP), and to fully exploit the benefit of joint optimization, a more in depth investigation into the joint bottlenecks and challenges is conducted. The result of this investigation is used as a starting point for the theoretical system modeling. From the model, novel and key system components are identified, and subsequently designed and implemented. Measurements of a proof-of-concept system implementation confirm the models and the benefit of the approach. The research presented in this thesis was conducted within the framework of the MIMO in a Mass Market project.

To provide the proper context of the research, we will first start this chapter by providing background information on wireless systems. Secondly, the capacity formula as derived by Claude E. Shannon is given to show the limitations of single antenna systems and indicate the benefit of multiple antenna systems. Thirdly, mayor trends in wireless transceivers are introduced which influence our design choices. Fourthly, after introducing the proper context, the MIMO in a Mass Market project in which the research was conducted is explained. Fifthly, the Research described in this thesis and the contributions are listed. The final section of this chapter explains the structure of the thesis.

1.1 Wireless Communication

Wireless transceivers communicate via electro-magnetic waves ranging in the frequency domain from several kHz up to 1 THz. These electro-magnetic waves can

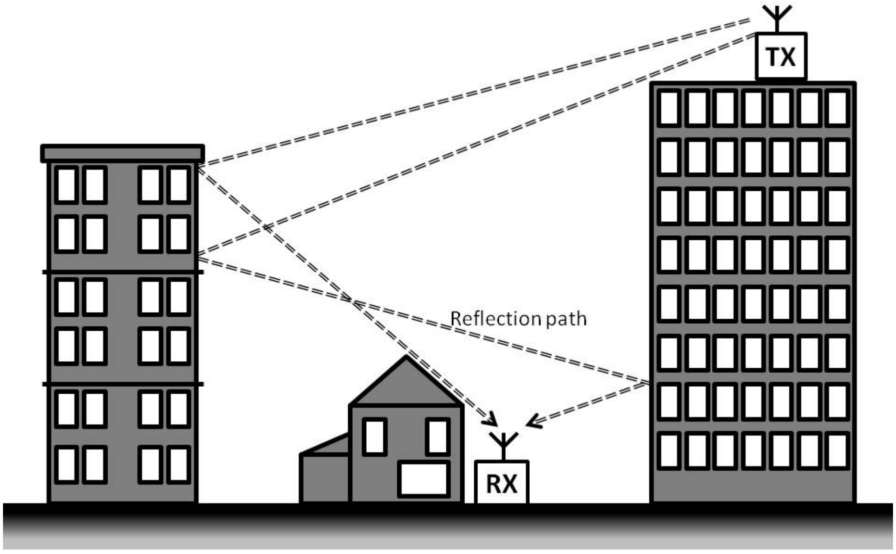

Figure 1.1: Example of an outdoor radio link.

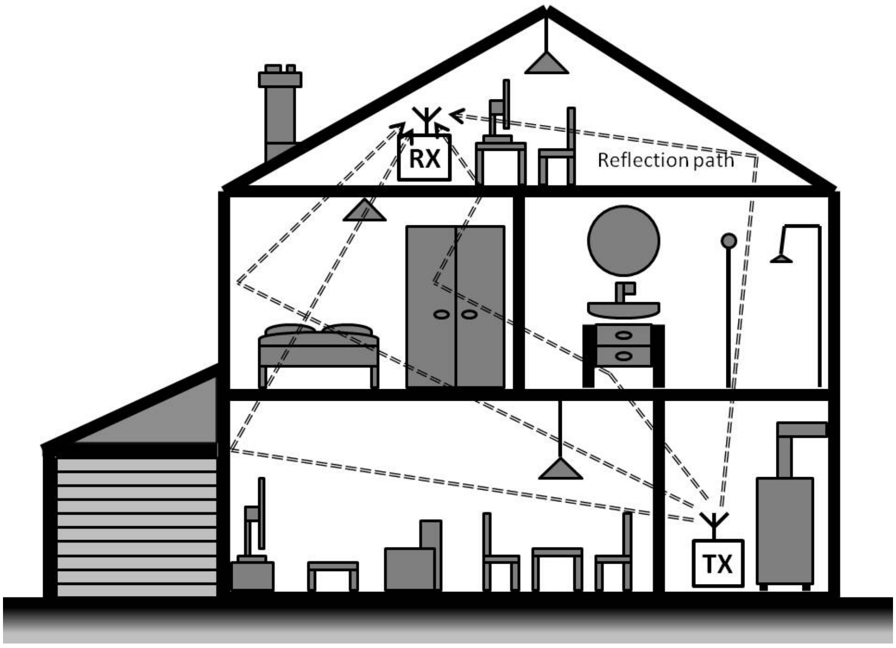

Figure 1.2: Example of an indoor radio link.

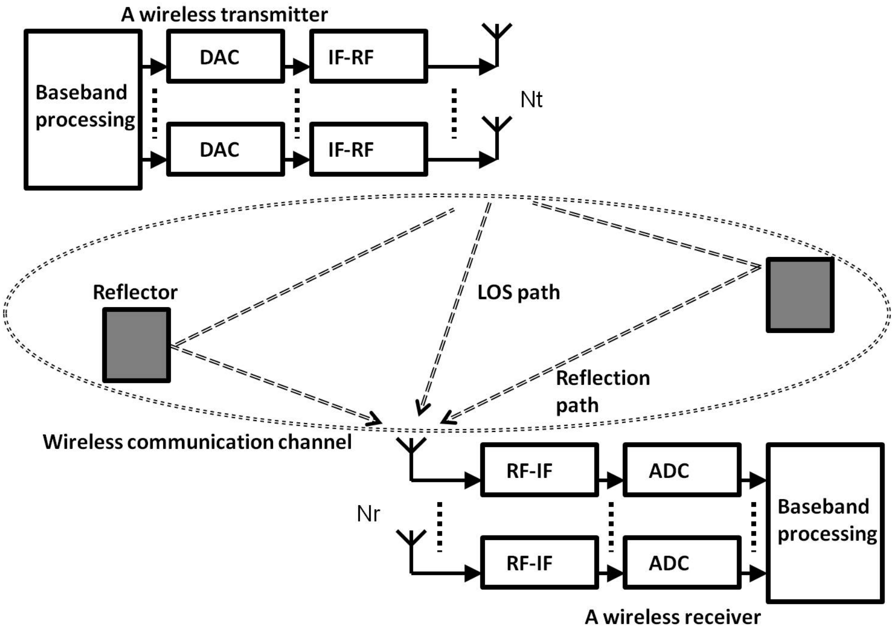

Figure 1.3: A wireless transmitter an receiver.

propagate through several media such as windows, furniture, walls, air, or even entire buildings. Since waves can bounce off of objects, the receiver can receive multiple copies delayed in time of the originally transmitted wave. An example of outdoor and indoor wireless channels is depicted in Figure 1.1 and 1.2, respectively. Here, the transmitter is denoted by TX and the receiver by RX, and several reflected waves are graphically illustrated via arrows. A wireless transceiver consist of several parts as is depicted in Figure 1.3. The digital information meant for transmission, is packaged by the digital BB processing at the transmitter. It is then converted to the analog domain via an digital-to-analog converter (DAC). The analog intermediate-frequency (IF) and RF processing up-converts the low frequency analog signal to radio frequency and transmits the signal via one or more antennas. The transmitted signal reaches the receiver via a wireless channel, which may consist of several reflection paths and a line-of-sight (LOS) path. The receiver picks up the transmitted signal via one or more receive antennas. The RF-IF processing part of the receiver down-converts the received high frequency analog signal to a low frequency signal as such that it can be digitized by the analog-to-digital converter (ADC). The digital baseband processing of the receiver unpacks the received signal to retrieve the transmitted digital information.

1.2 Capacity of Wireless Systems

The amount of information that can be transmitted via telecommunication systems is governed by the Capacity equation [1]. For a single-input and single-output (SISO) system with an additive white Gaussian noise (AWGN) channel, the achievable capacity has been shown to be

$$C = B \log_2 \left(1 + \frac{S}{N} \right). \tag{1.1}$$

Here B is the bandwidth, S the power of the received signal, and N is the variance of the AWGN. Further $N = kTB$ with Boltzmann's constant $k = 1.38 \cdot 10^{-23}$ JK^{-1} and T the temperature in Kelvin.

Traditionally, telecommunication systems increase the capacity by either increasing the available bandwidth B or by increasing the received signal power S. The Friis transmission equation gives the power received by the receiver under idealized conditions, for free space the Friis transmission equation is

$$S = P_T G_T G_R \left(\frac{\lambda}{4\pi D} \right)^2 \tag{1.2}$$

here S is the received signal power, P_T is the transmit signal power, G_T is the transmit antenna gain, G_R is the receiver antenna gain, λ is the wavelength of the transmit frequency and D is the distance between transmitter and receiver. As can be seen in Friis equation, the received signal power S can be increased at the transmitter by either devoting more power towards transmitting or by increasing the antenna gain. The antenna gain at both the transmitter and receiver can be increased by the use of directional antennas. Along with the current trend for larger bandwidth there is a shift to an ever higher carrier frequency as lower frequency bands become increasingly congested. Unfortunately, since $f = 1/\lambda$, the received power for a fixed distance is decreasing with the square of the frequency. The result is that as the carrier frequency is increasing, the distance that can be covered is decreasing, at similar transmit power and at similar antenna gains. To counteract the decrease in transmit distance one can increase the antenna gain proportional to the carrier frequency increase. For single antenna systems this can be achieved by using highly directional antennas. Another option is to use multiple antennas and constructively combine their transmitted and received signals. Increasing the amount of antennas increases the effective antenna area, allowing for more energy to be received and transmitted at different locations in space. In Section 3.3 it is shown that modern multiple-input and multiple-output (MIMO) systems can exploit the spatial domain as an additional degree of freedom to create parallel communication paths to vastly increase the channel capacity when compared to traditional SISO systems.

1.2.1 MIMO

An increased effective antenna gain via multiple antennas opens up a new degree of freedom in the Capacity equation, since most wireless communication channels are selective in the spatial domain. The spatial selectivity stems either from the spatial distribution of the antennas, and/or the existence of reflective surfaces. MIMO systems seek to exploit this additional degree of freedom in order to increase the achievable capacity [2] [3] [4]. The same frequency band is reused to transmit independent information along separate spatial streams.

1.3 Trends in Wireless Transceivers

In wireless communication systems we can identify several long term trends

- Increase in communication bandwidth
- Migration to higher frequency bands
- Communication over shorter distances
- Decrease in transmit power

- Increase in number of antennas
- Increase in number of standards
- Increase in the number of wireless devices in a mobile device
- Creation of generic platforms for several standards
- Increase in number of users
- Increase in functionalities of a mobile device requiring more battery power
- Improvements of battery technology, used for mobile size reduction

1.3.1 Migration of RF Frequencies Bandwidths and Distances

The desire for increased data-rates in wireless local area networks (WLAN) and cellular phones (Figure 1.4), has resulted in a subsequent need for additional bandwidth. As lower frequency bands become congested, additional spectral space is used at higher RF frequencies. Currently, this trend still continues with the introduction of e.g. 60 GHz transceivers with up to 7 GHz of available spectral space for the WiGig standard [5]. As was explained in Section 1.2 via (1.2), an increase in carrier frequency results in a smaller transmit distance, when transmit power and antenna gain remains equal. Therefore, next to the migration to higher frequencies, wireless transceivers tend to transmit over shorter and shorter distances. However, there is a benefit to a smaller transmit range. A decrease in the transmit distance allows for smaller cells and thus higher spatial reuse of the same frequency, effectively increasing the data rate per surface area. The current electric infrastructure that enables mobile communication consists of both wired and wireless links. Since the communication distances are becoming shorter, the final stage of the communication to the end user is increasingly becoming wireless. For example, this can be a base station for mobile phones replacing the landlines, a Bluetooth device wirelessly connected to a computer replacing the cable, a wireless DECT telephone system connected to a fixed landline replacing the phone cord, or a wireless internet router connected to the landline of the internet connection

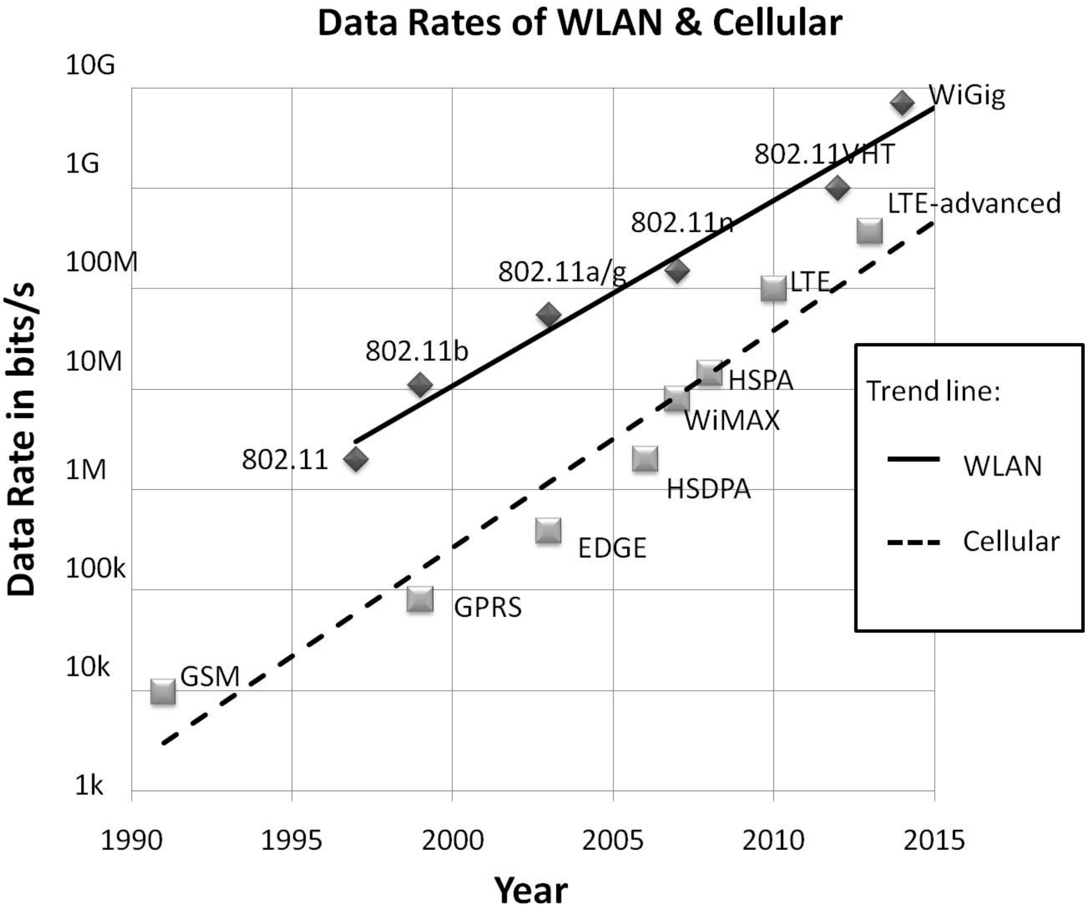

Figure 1.4: Demand for data rate in WLAN and Cellular.

replacing the WLAN cable to the computer. To illustrate the migration to smaller communication distances we listed several well known wireless communication systems and their introduction date:

- 1904 Marconi across the Atlantic
- AM radio (200 km, 2,000,000 watt)
- FM radio (50 km, 50,000 watt)
- 1980 cellular radio (3 km, 10 watt)
- 2000 WLAN (10 meters, 0.1 watt)
- 2010 Body area Networks (1 meter, 0.01 watt)

1.3.2 Multiple Antennas

Similar Band

There are two main drivers behind the use of multiple antennas at the same frequency band. The first reason originates from (1.2), where multiple antennas help to compensate part of the loss of received power at smaller wavelengths by increasing the effective antenna gain. The other reason to use multiple antennas is to exploit the spatial selectivity of the channel to increase the data rate in a limited spectral space, i.e. reuse spectral components across different reflective surfaces in the channel.

A physical explanation of the received power loss due to smaller wavelengths in (1.2) is that it is due to the receive antenna aperture, since at smaller wavelengths antennas are smaller in order to effectively pick up power from an incoming electromagnetic wave. Because the antenna is smaller, the energy they are able to pick up at equal transmit power and distance is decreased as well. This effect can be restrictive at very high carrier frequencies such as for example the 60 GHz ISM band. In order to achieve enough antenna gain to receive enough of the transmitted power over a given distance, multiple antennas can be used [5]. These antennas are combined at RF in the analog domain and use a single receiver chain to process the common analog signal. Due to the limited spectral space of the ISM bands, or limited spectral space owned by mobile operators, it is attractive to use multiple antennas to increase the throughput. This allows for an additional degree of freedom, due to the spatial selectivity of the channel. Examples of standards exploiting spatial selectivity are the IEEE 802.11n standard and LTE advance. In these standards each antenna has its own receiver chain and the antennas are used to send independent information via different reflective surfaces at similar frequencies.

Multiple Bands

Although modern antennas in handheld devices are capable of receiving a multitude of frequency bands there still are several antennas in a handheld connected to different transceivers. The existence of multiple antennas for multiple standards may be due to the desire to use several functionalities simultaneously. A mobile user might be listening to an FM radio station while he is transmitting a photo to another user via a Bluetooth connection.

1.3.3 Multiple Standards and Devices

Next to the trend towards more antennas for a transceiver we observe that new generations of mobile phones and laptops accommodate more and more standards which often have an antenna of their own. This means that there is an increased number of antennas which need to be fitted in a mobile device. One option to reduce the number of antennas is to use an antenna for more than one standard. The standards available in modern handhelds may be, but are not limited to, multi band GSM, GPS, FM-radio, Bluetooth, WLAN, and NFC. With the introduction of new standards such as LTE advanced and WiMAX, the number of supported standards is expected to increase for the foreseeable future.

For size and cost reduction it is desirable to create generic platforms to accommodate several wireless standards in a single transceiver. Standards are often combined when they occupy a similar frequency range. A single transceiver in a mobile device can than service several standards in the same frequency range. Several of these transceivers are placed in a mobile phone or a laptop to allow mobile communication across a plurality of standards. For further cost and size reduction it can be desirable to combine standards operating at different frequency ranges. A downside of generic platforms is that they often require additional dynamic range, frequency range, linearity, and isolation requirements (when compared to single purpose solutions) in order to comply with all the standard requirements, and as such commonly require more battery power. The combined requirements of separate standards can even prove to be prohibitive in creating generic devices. Despite the benefits of antenna sharing, size and cost reduction, the use of generic platforms commonly increases overal power consumption reducing battery lifetime.

1.3.4 Multiple Users

Interference

With the success of mobile communication the number of users has grown rapidly over time. The increase in the amount of users has resulted in an increasing amount of interference and the congestion of limited spectral space. Even when users occupy different frequency bands, part of their transmit power can end up in the band of adjacent users interfering with their transmission. Since more users are present, the chance of a powerful interferer appearing at the antenna is increased. The presence of powerful interference increases the chances of desensitization of a receiver and thus blocking of the desired transmission. To decrease the possibility of blocking due to interference, the interference power levels at which a receiver should still operate is increased in new generations of receivers.

In most receivers a broad band signal is processed at RF by the analog front end, where the desired signal only occupies a small portion of the front end bandwidth. To present the desired signal to the BB ADC, the analog front end amplifies, down-converts, and filters the received RF broadband signal. Therefore, the first stages of the receiver usually contains strong adjacent channel interferers, with a priori not fully known statistical properties [6]. These signals need to be handled with adequate linearity to avoid excessive distortion spill-over into the band of the desired signal [7]. Generally, a higher linearity requirement leads to a higher power consumption of the analog circuit. In conventional RF designs the linearity is fixed and specified for the highest power of the interference at which the receiver should still operate, thus resulting in an overly linear design at all lower values of the interference power, reducing battery lifetime unnecessarily. Most RF designs are based on a set of system specifications, these specifications are determined by standardization [7], and may include packet error rates, sensitivity and modulation. An RF designer then strives to design a receiver at the lowest power possible, for this target [8, 9].

Cognitive Radio

Cognitive radio (CR) promises to vastly improve the efficiency of spectral use. In the concept of CR the radio continuously senses and uses unoccupied channels in a wide band spectrum, alleviating congestion and improving the overall throughput.

In order to adequately receive and reconstruct the transmitted data from the desired signal, both coordinated and random interfering signals need to be filtered. The filtering of interference can occur in combinations of domains, such as time domain filtering, code domain filtering, frequency domain filtering, and spatial domain filtering.

We observe that in most systems the RF front end and ADC handle the interfering users via extra dynamic range (DR) and linearity, which make them power hungry [10]. The DR and oversample frequency of the ADC are a combination of the interference power level with which the receiver needs to cope, both in and out of band, and a trade off with the analog filter drop off [11].

However, modern MIMO systems make it feasible to include spatial filtering techniques in the analog front end. Since the channel is selective in the angular domain, such techniques have the potential to vastly reduce the interference power and thus the DR and linearity requirements of both the RF front end and ADC. Therefore, a spatial filtering technique can be the basis for ultra low-power high data-rate wireless receivers, and has the potential to mitigate the DR requirements of cognitive radios.

1.3.5 Energy Trends

Additional Functionalities

In the first GSM phones the majority of the available battery power was allocated for the wireless GSM transmission. With the recent succes of smart phones, the trend of introducing more and more features next to the core application has continued. Today mobile phones share the scarce battery resource over a plurality of applications. Not the least one is the screen, which requires an ever larger portion of the battery power as its size increases. Further, more wireless application require a portion of the battery power even when they are not used, as they are often set to a standby mode. This trend has resulted in an ever dwindling percentage of battery power availability for the core GSM function and a competition between application for a limited resource, driving the need for ever more power reduction of the individual application.

Available Energy and Phone Size Reduction

At the same time as we have witnessed an increase in the amount of applications in a mobile phone, the energy density of batteries has finally took off. Where battery technology was stagnant for almost 150 years (Section 2.4), the invention of the mobile phone has spurred research in this field resulting in batteries with vastly superior energy densities, of almost an order of magnitude larger than only two decades ago. Compared to the historic trend of battery power technology, this is

Figure 1.5: Smart phones; the Nokia 9110 Communicator (1999) and the iPhone 3G (2008).

a huge acceleration in the field.

Although energy density has gone up considerably, the available energy in a mobile phone has remained near constant over the last two decades (Section 2.3). This is due to the appeal of a small and thin phone to the consumer. So rather than relaxing power requirements and increase battery lifetime, consumers and producers alike have opted for ever smaller, lighter, and thinner phones. Every new battery technology has led to a size reduction, rather than the availability of more energy. Where the first commercially available cellular phone, the Motorola DynaTAC 8000X from 1983 weighed 783 grams, the Nokia 3110 classic from 2007 weighs 87 grams. With the recent succes of smart phones (which are replacing regular mobiles phones) and the subsequent increase in screen and phone size, this weight reduction trend might be slightly reversed or halted for the time being. For example the Apple iPhone 4 from 2010 weighs 137 grams, were the iPhone 3G from 2008 weighs 133 grams. This is because there are two counter acting trends for smart phones, the ongoing miniaturization of applications and the ongoing increase in the number of applications in a mobile phone. Despite these counter acting trends, a similar trend of making phones thinner and lighter over time is observed among smart phones as well, as for example the Nokia 9110 Communicator from 1999 weighs 253 grams (Figure 1.5). In the case of the Nokia 3110 the miniaturization of applications was the dominant driver in weight reduction compared to the Motorola DynaTAC 8000X. In the case of the smart phones weight is reduced slower, as the miniaturization trend is currently offset by the increase in number of applications.

1.4 MIMO in a Mass Market

The aim of the MIMO in a Mass Market project is power reduction of MIMO systems and interference mitigation, without loss in performance. In most wireless communication systems the interface to the landline, such as a wireless router or a basestation, is power plugged thus power consumption is less constricted. On the other hand, the mobile user is limited by the available battery power.

MIMO transceivers take advantage of the existence of multiple reflected waves in wireless channels (Section 3.3). MIMO systems consist of multiple transmit and multiple receive antennas. MIMO systems exploit reflected waves by transmitting different information on the same frequency over separate reflections. Thus exploiting the spatial selectivity of the channel. This allows the transmission of more information than SISO systems.

Current MIMO systems consist of dedicated transmitters and receivers per transmit and receive antenna. Since the average data-rate of MIMO systems scales less than linearly in the number of antennas, the power efficiency of MIMO system is reduced when the number of antennas is increased.

Due to the succes of wireless devices, and their subsequent increase in numbers, they interfere more and more with one another. Traditionally, an increase in interference levels has been handled by increasing linearity and dynamic range of the receiver. Unfortunately, increasing linearity and dynamic range comes at a cost of higher power consumption [7].

The main focus of the MIMO in a Mass Market project is on the receiver circuit power consumption. The motivation to focus on a receiver with a limited availability of battery power is two-fold. In many applications, the mobile user spends significantly more time receiving data than transmitting. Often, the energy consumed in receiving mode is several orders of magnitudes larger than the energy consumed in transmit mode [12] [13], even if the transmitter circuit power consumption is larger than the receiver circuit power consumption when switched on. Secondly, in a short range link, the transmit power can be relatively small. So the transmit power amplifier is no longer the main power consumer. Yet, the receiver front end often needs to recover a weak signal in the presence of strong adjacent channel interference, which requires highly linear, thus power hungry RF designs. In the absence of disruptive new approaches, we expect that this trend will continue for the foreseeable future.

Traditionally the BB and RF of transceivers are optimized separately. The MIMO in a Mass Market project aims at achieving its goals via system optimization over both the RF and BB domain. This joint optimization requires novel architectures and baseband algorithms.

The MIMO in a Mass Market project is sponsored by Senter-Novem under the IOP-Gencom program (IGC05002) and is a collaboration in the framework of 3TU (consisting of the Delft, Eindhoven and Twente universities of technology) and industrial partner Philips Research.

1.5 The Research

As mentioned in the introduction of this chapter, the research presented in this thesis contains theoretical system modeling considering arguments based on Shannon capacity, and a partial system implementation used for verification of the theory. The system implementation consists of algorithm design, PCB design, and circuit design and implementation in 65 nm CMOS. To fully exploit the benefit of a joint optimization of both RF and BB, an in dept investigation into the joint bottlenecks and challenges is conducted. From this investigation, key system components are identified, and novel components are designed and implemented. A proof-of-concept system measurement confirms the models and the benefit of the joint RF-BB optimization approach. The results of the research are listed below.

1.5.1 Scientific Contributions

We showed that mitigating interference as early as possible in the receiver chain is a favorable approach in achieving the objectives of the MIMO in a Mass Market project, as it simultaneously increases interference robustness and decreases power consumption.

We succeeded in setting up a generic framework that leads to system level conclusions. The closed-form solution is used to calculate the optimal transmission rate for a given receiver circuit power and to calculate the maximum achievable receiver efficiency in terms of bits per Joule of receiver energy. Further, the frame-

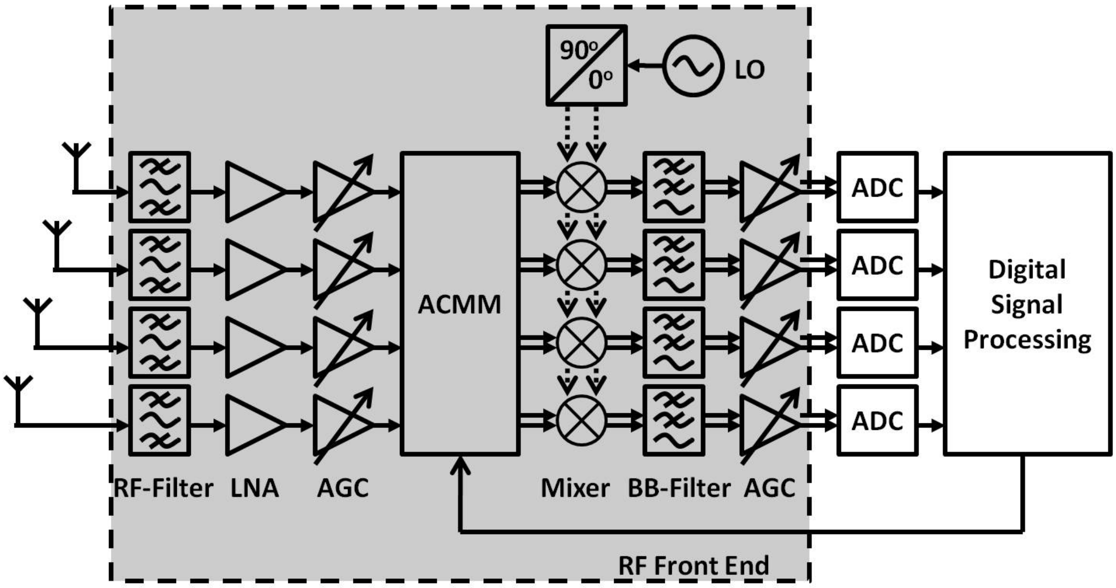

Figure 1.6: System setup of full rank MIMO matrix-beamformer.

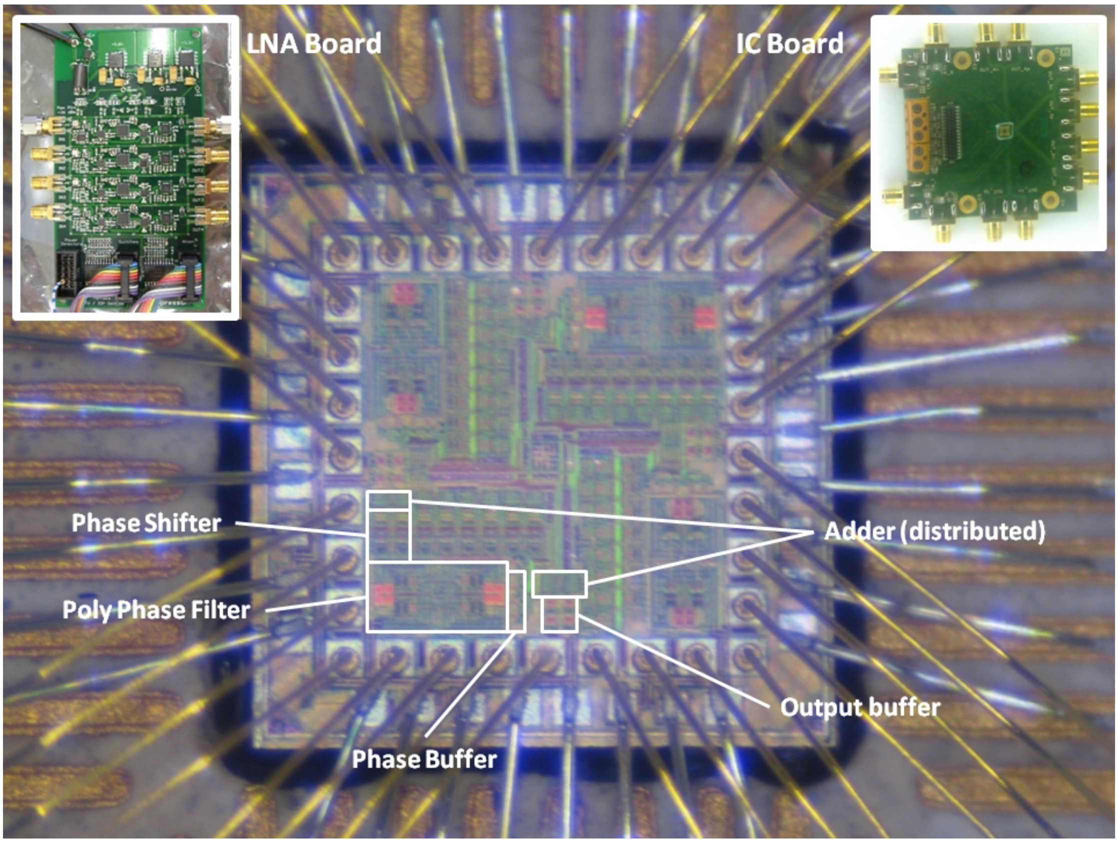

Figure 1.7: ACMM IC Die close up and PCB board of full rank MIMO matrix-beamformer.

work is used to determine when duty cycling is an optimal transmission strategy. Furthermore, we established that the throughput at the highest receiver circuit power efficiency setting converges to an upper limit at high SNR. Via optimizing RF power consumption for maximum throughput, we formalized the relation between interference handling and receiver power consumption [14–16]. An implicit relation between interference and receiver circuit power consumption was reported earlier [6–9, 17], but never formalized in a closed-form solution.

We proposed a full MIMO spatial filtering architecture, depicted in Figure 1.6. This architecture is a full matrix 4×4 beamformer, geared towards interference suppression. The benefit of spatial filtering of interference in vector beam formers had been speculated by D. Cabric [6] for ADC power reduction. We showed that spatial filtering at RF also leads to power reduction of over an order of magnitude in the RF domain [14–16]. Our use of a fully MIMO matrix-beamformer for spatial filtering is new. The benefit of using a matrix structure compared to the classic vector structure is that we still allow multiple spatial streams and maintain full rank, fully benefiting of the MIMO channel capacity. This is in contrast to the classic vector beamformer which performs a rank reduction effectively limiting the throughput to the SISO case with a high gain antenna.

We extended the theoretical benefit of the spatial filtering approach to the cognitive radio in collaboration with prof. D. Cabric from the UCLA Cognitive Reconfigurable Embedded Systems Lab and results have been published in [18]. Numerical results indicate that spatial filtering of undesired users can reduce dynamic range requirements and reduce ADC power consumption up to 90%.

We designed, and are the first to implement and measure, a full rank analog complex matrix multiplier (ACMM) for full matrix-beamforming in 65 nm CMOS (Figure 1.7). The measurements confirmed theoretic expectations reported in [6, 14, 16, 18].

1.6 Structure of the Thesis

Chapter 2 reviews the current state of the art and expected technology trends, which help to identify long-term bottlenecks.

Chapter 3 of the thesis expands the models of Chapter 2, and shows that by exploiting the spatial selectivity of the wireless channel in the RF domain of the MIMO receiver for interference mitigation, there exists potential to vastly reduce receiver circuit power consumption and improve overall interference robustness.

Chapter 4 of the thesis focusses on the relationship between receiver circuit power consumption in RF front ends and interference power levels. Next to the relation between receiver circuit power and interference levels, the optimal throughput for a low power wireless receiver is calculated.

Chapter 5 of the thesis shows the IC design of the analog spatial filter, the ACMM IC in 65 nm CMOS. Further, Chapter 5 shows the implementation of the IC in the receiver via a custom designed PCB, with off-the-shelf components and the custom designed ACMM-IC. Finally Chapter 5 shows the proof of concept measurements.

Chapter 6 focusses on the digital baseband algorithms that are required to obtain an optimal beamforming setting of both a beamformer and the ACMM. Via practical algorithms it is shown that analog beamforming can result in significant ADC power consumption reduction.

Chapter 7 provides the conclusions and recommendations.

Chapter 2

State of the Art MIMO OFDM Systems

2.1 Introduction

As mentioned in the introductory chapter, there are several trends that can be distinguished in wireless communication. Some are obvious to regular users, such as an increase in standards in their mobile phones, and some are less visible such as power consumption trends of individual components that make up the mobile device. In this chapter we will show that in the absence of disruptive new technologies, the RF front end and ADC power consumption are the future bottlenecks of MIMO transceivers in terms of extending battery lifetime. Since interference poses strong dynamic range requirements on the front-end and ADC, mitigating the interference has the potential to vastly reduce the power consumption of the ADC and RF front end. We will focus on the power trends of wireless transceivers and the available energy in battery powered devices. Because battery energy is a scarce commodity in a mobile device, such as a smart phone, reducing the power consumption of wireless transceivers to increase battery lifetime is of prime importance. The power trends of individual components that make up the wireless link are extrapolated to obtain expected development curves. The expected development curves are used to identify the mayor future bottlenecks. Identifying and solving the future bottlenecks is important when designing systems that are supposed to be used in the future.

An obvious shift in mobile communication of the last couple of years, as the smart phone is becoming more popular, is the emphasis that is put on increasing data transfer. Most mobile phones are now connected to the internet, and generate more data traffic than ever before. When planning for communication networks, operators need to account for the number of consumers per unit area in cities and towns. In cities, operators tend to prefer small cell sizes, allowing them to reuse their frequencies more often over the city area and thereby achieve a high data rate per square meter where there are many customers per unit area, as such that each costumer has a high data rate available (examples of such a standard are WiMax and LTE Advanced). In rural areas, relatively long range connections are preferred, even though these generate a low data rate per square meter covered. But, since the number of costumers is relatively small, such systems still achieve a high data rate per costumer. An example is the wireless regional area network (WRAN) function of IEEE802.22. Since more and more people migrate to cities and more people inside cities use smart phones, expectations are that communication distances will decrease, to allow for even denser reuse of precious spectral resources.

Modern MIMO systems exploit spatial diversity of urban propagation environments. MIMO systems reuse the same RF frequencies or spectral resources to transmit different data simultaneously to a single user. This is achieved by exploiting reflective surfaces to open parallel data streams. Since MIMO systems are inherently directional they can also be used in a single base station of, for example, the LTE Advanced standard to beamform on the same frequency to different users without mutual interference, as would have been the case with omnidirectional SISO transmissions.

Current MIMO systems consist of dedicated transceivers per transmit and receive antenna. Thus the power consumption of the ADCs and RF front ends increases linearly in the number of transmit N_t and receive N_r antennas. Unfortunately the increase in average capacity scales less than linearly in the number of antennas. In this chapter we will first introduce the power breakdown and power trends of

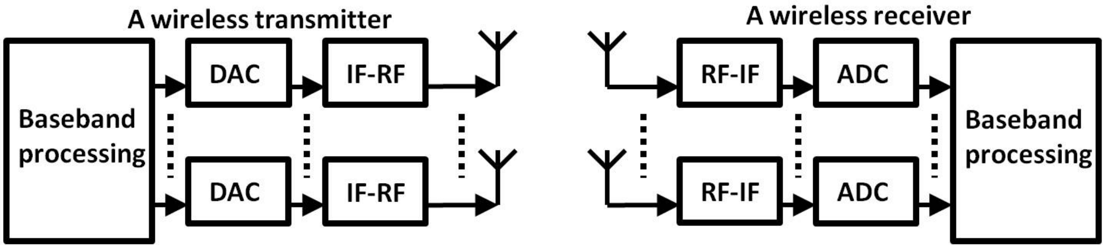

Figure 2.1: A wireless transceiver.

MIMO systems. Then we will discuss several key components that impact the available energy for the MIMO system in mobile devices. Finally we will give an extrapolation of the long term trends of MIMO transceivers. We identify the receiver RF and ADC as the future bottleneck in energy consumption reduction.

2.2 Receiver

A typical transceiver consists of several blocks as is depicted in (Figure 2.1). In common user scenarios, most users spend significantly more time receiving than transmitting [12] [13]. As a result the total energy consumed in the receiver can be orders of magnitude larger than the energy consumed in the transmitter. Moreover, the increase in the number of users poses additional dynamic range requirements on the front end. Unfortunately, the power consumption of the front end scales exponentially in the DR, making the front end more power hungry [9]. To find a reliable power trend for the transceiver we will first start with the power trends of the RF, then the power trend of the analog-to-digital converters is presented and finally the baseband processing trend is given.

2.2.1 RF Front End

Establishing a reliable power trend in RF is difficult due to the multitude of standards and requirements. Despite these difficulties, a commonly used rule of thumb is an order of magnitude power reduction for the same function per decade. Since

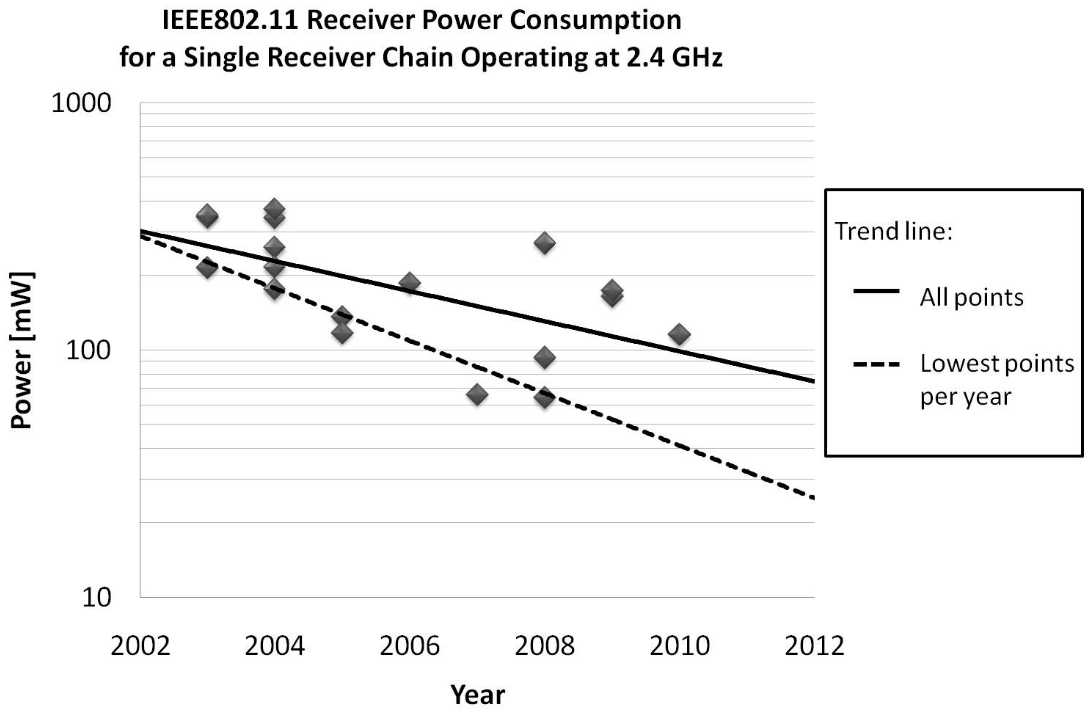

Figure 2.2: *Power consumption of IEEE802.11 receivers over time.*

we are interested in MIMO systems, we will focus on equipment that can operate at 2.4 GHz according to the IEEE 802.11n standard. An additional benefit of limiting ourselves to a single standard is that the receivers need to operate according to a similar specification set, making them easier to compare.

The eighteen data point of the receivers in Figure 2.2 are given by Table 2.1. In Figure 2.2 a straight solid trend line is plotted using all the data points. The angle of the actual power trend line may differ quite a bit from the solid line found here, as every point is slightly biased due to different system requirements. In our data set, later receivers mostly are dual mode receivers operating at different frequencies and as such have to comply to more stringent specifications making them more power hungry than would have been required for a dedicated receiver. This affects te trend line and leads to a lower slope than an order of magnitude per decade. A further limitation of the solid line is the fact that we relate the power consumption back to one receiver chain. MIMO receivers share resources such as the clock and PLL, making the power consumption per chain slightly more favorable and more difficult to compare to a SISO receiver.

Table 2.1: *Data points of Figure 2.2.*

Journal/Conference	**Year**	**Power [mW]**	**Reference**
RFICS	2003	345	[19]
ISSCC	2003	350	[20]
ISSCC	2003	215	[21]
JSSC	2004	260	[22]
JSSC	2004	176	[23]
ISSCC	2004	216	[24]
ISSCC	2004	342	[25]
JSSC	2004	370	[26]
ISSCC	2005	136	[27]
JSSC	2005	117	[28]
JSSC	2006	186	[29]
ISSCC	2007	66	[30]
ISSCC	2008	270	[31]
ISSCC	2008	93	[32]
RFICS	2008	64	[33]
ISSCC	2009	165	[34]
ESSCIRC	2009	174	[35]
RFICS	2010	115	[36]

There are two trends influencing the solid line in Figure 2.2. On the one hand miniaturization helps to decrease power consumption. On the other hand, as mentioned in Section 1.3.3, for size and cost reduction it is desirable to create generic platforms to accommodate several wireless standards in a single transceiver. However, the combining of functionality in one receiver results in more stringent requirements and thus more power consumption than would have been required by a dedicated receiver. Another method is to use only the best data per year for dedicated receivers and plot a line through them, as is indicated by the dotted line. In this line all points are dedicated receivers at 2.4 GHz, further we have omitted data from 2009 and 2010 as those receivers are all dual band. As can be seen in Figure 2.2, the dotted line comes close to one order of magnitude per decade. The dotted line in Figure 2.2 isolates the trend due to miniaturization better than the solid line and confirms the rule of thumb for the power trend in RF of an order of magnitude power reduction for the same function per decade. However, the increase in the number of users, and the subsequent required DR to handle the additional interference, is expected to increase the power consumption of the front end.

2.2.2 ADC

A commonly used rule of thumb for ADC power consumption is given by Walden, and predicts an order of magnitude every decade [37], [38], [39]. Note that this rule of thumb is similar to rule of thumb of the analog RF front end explained in the previous section. Another rule of thumb given by Murmann predicts a factor of two every two years [40], [41], [42]. A problem in accurately predicting trends in ADC power consumption is the choice of FOM and the arbitrary nature of such FOMs. For our own analysis depicted in Figure 2.3 we used the Murmann data set which is available here [43]. As a measure of ADC power consumption, we plotted the Joule per conversion step. To calculate the Joule per conversion step, a common figure of merit as was used by Walden [37], [38], [39] is used,

$$\mathrm{FOM1} = \frac{P}{f_s \cdot 2^{\mathrm{ENOB}}} \tag{2.1}$$

were the effective number of bits (ENOB) is given by

$$\mathrm{ENOB} = \frac{\mathrm{SNDR(dB)} - 1.76}{6.02}. \tag{2.2}$$

Here P is the power dissipation of the ADC, f_s is the sampling frequency of the ADC, and SNDR is the signal-to-noise-and-distortion ratio.

It is important to point out that another FOM than FOM1 is often used to compare the performance of ADCs that are limited by thermal noise. This is mainly the case for very high resolution ADCs (SNDR > 85 dB) [41]. This figure of merit is defined as,

$$\mathrm{FOM2} = \frac{P}{f_s \cdot 2^{2\mathrm{ENOB}}}. \tag{2.3}$$

As can be seen in (2.3) FOM2 scales with twice the ENOB in the denominator when compared to FOM1. FOM2 is often used in literature to compare the performance of e.g. high resolution pipelined ADCs. Even though FOM2 is a more accurate FOM when comparing the performance of very high resolution ADCs, the assumption that the ADC is limited by thermal noise is often pessimistic for real designs. Therefore, the appropriate use of FOM2 depends on both the design and implementation of the considered ADCs. In this section we restrict ourselves to the more universally used FOM1, as was used by Walden [37], [38], [39], but it is important to keep in mind that the accuracy of FOM1 is limited when assessing the performance of thermal noise limited ADCs.

As can be seen in Figure 2.3 the trend line of the power consumption reduction (solid) over the years comes close to the factor of 2 per two years as was predicted by Murmann [40], [41], [42]. It should be noted thought that this is a data set which contains all 302 ADCs from ISSCC and VLSI from 1997 to 2010, each with their own specifications and application areas. Therefore, the resulting power trend does not necessarily hold for all types of ADCs. To find a more accurate power trend for our receiver we have plotted a second trend line (dashed) in Figure 2.3. Since most MIMO receivers use high resolution ADCS, we have only used the 93 data points of ADCs containing 12 or more ENOBs. The trend line of these high resolution ADCs comes very close to Walden's prediction of one order of magnitude per decade. Since we are using high resolution ADCs in MIMO receivers, we will use this trend line in the final section of this chapter. The trend line shows that miniaturization helps to decrease power consumption over time for the same functionality. On the other hand, the increase in the number of users and the subsequent increase in interference, increases the DR requirements of the ADCs in the front end and as such the required number of ENOBs. As can be seen in (2.1) and (2.3) the power consumption of the ADC scales exponential in the number of ENOBs for a given FOM. The increase of the required DR due to interference is counteracting the benefits of miniaturization.

2.2.3 BB Processing

The reduction of power consumption of the baseband processing engine has been governed by Moore's law for the past half century. Moore's law was first reported in 1965 [44], and states that the amount of transistors doubles approximately every two years. Due to reduced power supply voltage and increased transistor

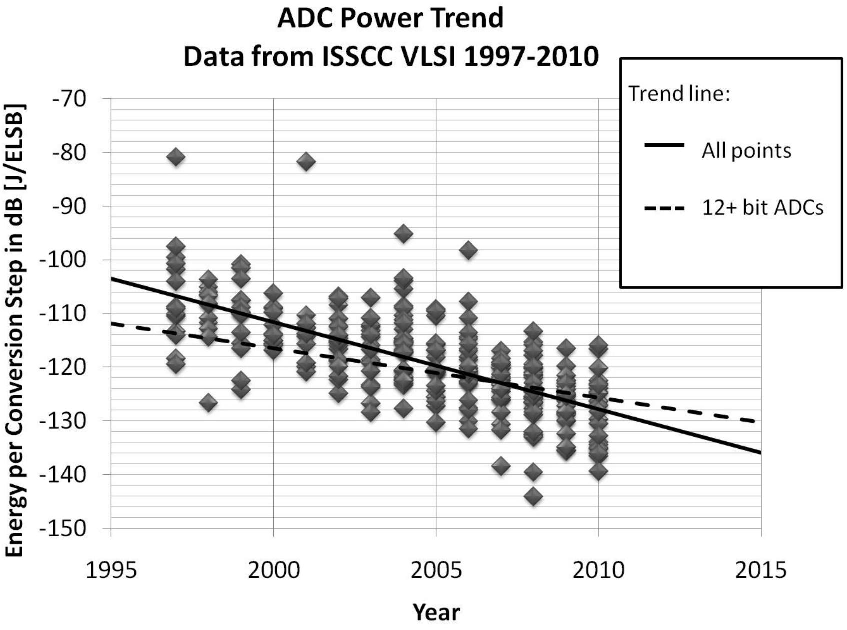

Figure 2.3: *ADC power consumption trend expressed in energy per conversion step.*

switching speed due to size reduction, the power consumption required to perform a certain computational task approximately halves every two years as well. It has been speculated that Moore's law will end in the foreseeable future. A first reason for the end of Moore's law is due to economics [45], as the cost of new manufacturing plants is growing beyond what private companies can afford. This effect is predicted to influence Moore's law from 2015 onwards [45]. Another reason for the predicted end to Moore's law is due to fundamental limits on the physical size of a transistor [46]. The size reduction of transistors will hit the size limit of an individual electron around 2036 [46], bringing an end to the possible size reduction of transistors. For now however, Moore's law is expected to continue in the foreseeable future.

2.3 Batteries

A very important aspect of mobile devices is the energy stored in the battery. The total energy capacity is determined by the battery technology used and the battery

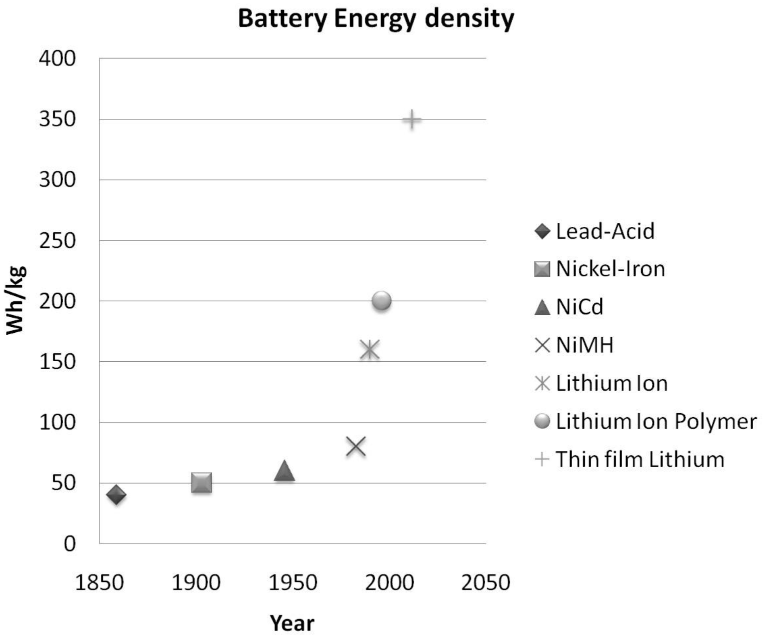

Figure 2.4: *Energy density of mass produced researchable batteries over time.*

size. For the first 150 years of battery technology, the development of energy density was almost stagnant. Only after the successful introduction of mobile phones into the mass market, battery technology finally took off in the 1990s as research budgets for novel battery technology grew (Figure 2.4). In Figures 2.5 and 2.6 the total amount of energy expressed in Wh that is present in mobile phones and smart phones over time is shown. In Figure 2.5 we can see that the amount of available energy in smart phones is more or less constant over time. This is because mobile phone consumers prefer small, thin, light phones. Therefore, every progress in battery technology is used to make the phone more appealing to the costumer by shrinking the phone size. A similar trend can be seen at regular mobile phones, although since the mobile phone and smart phone merged, the amount of energy in a mobile phone slightly increased.

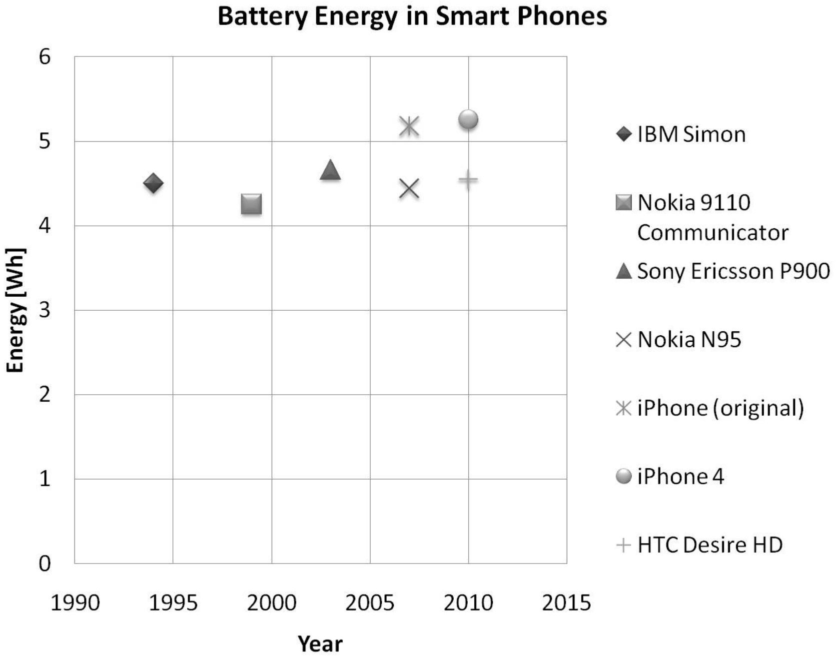

Figure 2.5: *Battery energy of mass produced smart phones over time.*

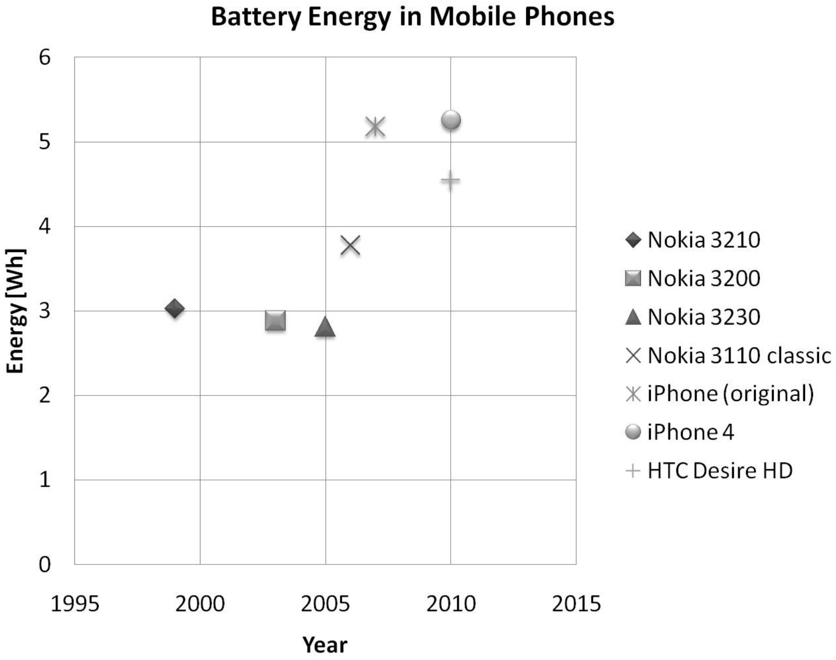

Figure 2.6: *Battery energy of mass produced mobile phones over time.*

2.4 Screen Size

During the same period that the total available energy has remained constant, screen size and subsequently the screens power consumption has steadily increased. Modern mobile screens can consume up to 1 Watt of power. When the available energy is 5 Wh, the screen alone can empty the battery in 5 hours. In Figure 2.7 the screen size over time of smart phones is shown. The same phones of Figure 2.5 are used and their data is listed in Table 2.2. It should be noted that the first smart phone in the list was grey scale and only more modern smart phones have touch screens. In Figure 2.8 the screen size of regular mobile phones is shown over time. The same phones of Figure 2.6 are used and their data is listed in Table 2.3. Since the introduction of the original iPhone in 2007, the smart phone (or personal digital assistent (PDA)) and the regular mobile phone have merged.

The ever increasing screen requires a big share of the available battery power and battery energy. As shown in Figures 2.5 and 2.6, the available battery energy is not expected to go up in the foreseeable future. Rather, phone manufacturers prefer to use battery technology improvements to shrink the size and weight of their phones. However, with the continued introduction of new standards and functionalities into mobile phones and the subsequent demands on hardware, there is continued need to reduce power consumption of existing hardware. On the other hand, emerging technologies such as OLED and E-paper, promise to vastly reduce the power consumption of the screens, leaving the wireless front ends as the major power consumer in the mobile.

2.5 Flash Memory Speed

Another important aspect of mobile devices is the writing speed of the memory, since it would not make sense to invent wireless systems with data rates that are faster than the writing speed of the memory. Currently, most mobile devices use flash memory cards for memory and/or memory expansion. Up until 2010 the flash memory market was highly fragmented, and there were rivaling formats such as

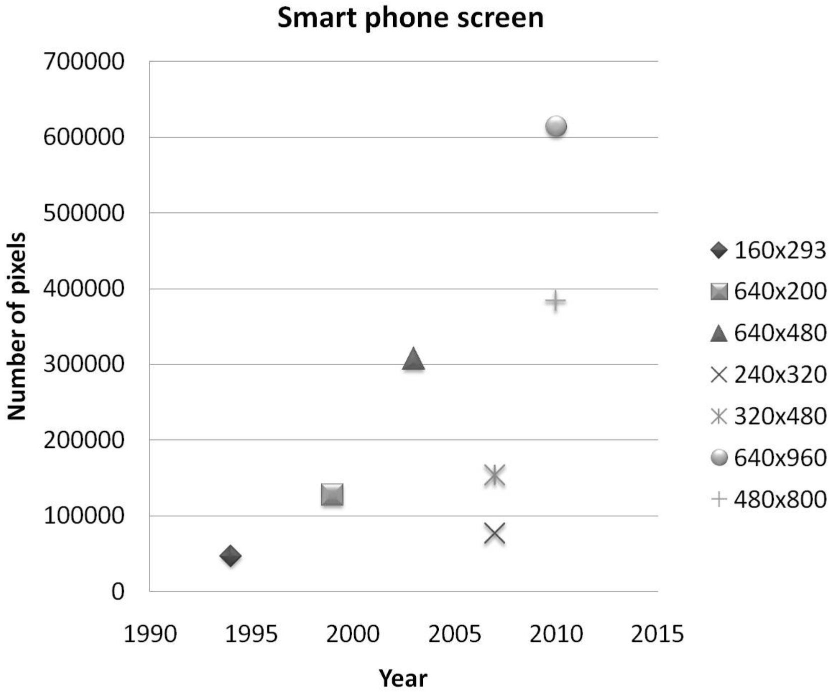

Figure 2.7: *Number of screen pixels in PDAs over time.*

Table 2.2: *Data points of Figure 2.7.*

Phone	**Year**	**Screen size**	**Remarks**
IBM Simon	1994	160x293	B&W
Nokia 9110 Communicator	1999	640x200	Grey scale
Sony Ericsson P900	2003	640x480	VGA touch
Nokia N95	2007	240x320	TFT, 16M colors
iPhone (original)	2007	320x480	VGA touch
iPhone 4	2010	640x960	VGA touch
HTC Desire HD	2010	480x800	VGA touch

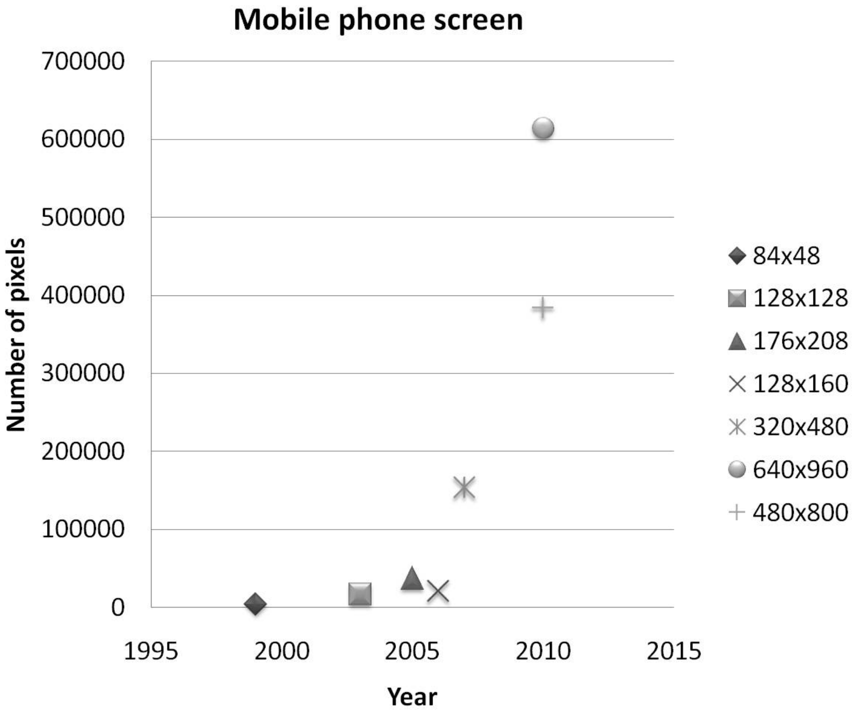

Figure 2.8: *Number of screen pixels in mobiles over time.*

Table 2.3: *Data points of Figure 2.8.*

Phone	**Year**	**Screen size**	**Remarks**
Nokia 3210	1999	84x84	B&W
Nokia 3200	2003	128x128	Grey scale
Nokia 3230	2005	176x208	TFT, 65K colors
Nokia 3110 classic	2006	128x160	TFT, 256K colors
iPhone (original)	2007	320x480	VGA touch
iPhone 4	2010	640x960	VGA touch
HTC Desire HD	2010	480x800	VGA touch

for example the Sony memory stick and the Olympus xD-Card. Since 2010 micro-SD (Secure Digital) has come to dominate the new high-end phones and tablet computers. The follow up of micro-SD is Secure Digital High Capacity (SDHC) which is meant for memory sizes of up to 32 GB. The follow up of SDHC, the Secure Digital Extended Capacity (SDXC) format was unveiled at CES 2009 and will support up to 2TB.

The maximum transfer rate of micro-SD using an Serial Peripheral Interface (SPI) bus is 10 MB/s. For our system, we conclude that higher transfer rates are needed, as the maximum raw data rate of IEEE 802.11n is 600 Mbit/s. The maximum transfer rate of SDXCs, which is planned to follow up the SD 3.0 specification, was announced as 832 Mbit/s, with plans that the SD 4.0 specification shall increase this to 2.4 Gbit/s. At those writing speeds, the writing speed of the memory will not be the bottleneck of our wireless system. Only for a system at the targeted 7 Gbit/s data rate of the 60 GHz band, the memory writing speed of SDXC can potentially become a bottleneck.

2.6 Extrapolations

Based on the power trends of the RF, ADC, and BB processing engine, we can extrapolate the power consumption reduction of the components of a 4x4 MIMO system into the near future. An important aspect to consider when extrapolating, is the fact that although the power consumption of dedicated RF receivers reduces with an order of magnitude per decade, the power consumption of multipurpose front ends does not necessarily follow the same trend line. As can be seen in Figure 2.2 the multipurpose receivers introduced after 2008 consume significantly more power than a dedicated single purpose receiver. Building a MIMO system from multipurpose transceivers may therefore be more power hungry than the values projected here. In the absence of disruptive new technologies, we expect the trends of RF, ADC, and BB to continue in the foreseeable future. Figure 2.9 depicts the expected power trend of MIMO OFDM systems. As can be seen in Figure 2.9 the power consumption of the digital baseband engine is expected to reduce faster than the power consumption of the ADC and RF. In Figure 2.9 it is assumed that the RF and ADC power consumption reduces about one order of magnitude per decade and the BB processing engine follows Moore's law. Further, it is expected that the power consumption of the RF and ADC remains more or less similar in a receiver.

As can be seen in Figure 2.9, the instantaneous power consumption of the IF-RF block of the transmitter is highest. This is because the power amplifier (PA) of the transmitter is required to put a certain amount of transmit power into the air. Due to the required transmit power, the power consumption of the RF of the transmitter is not expected to reduce. However, if we take user scenarios into account, the transmitter is actually only switched on for very short periods of time when compared to the receiver [12] [13]. Thus, the total energy used for receiving is often orders of magnitudes larger than the total energy used for transmitting. To reduce overall power consumption of the transceiver the focus will be on the part that consumes the most energy over time, in our case the receiver chain.

As can be seen in Figure 2.9 the power consumption of a current state of the art 4x4 MIMO system is more than 1 Watt [32] [33]. A typical 4x4 MIMO system can drain a typical smart phone battery in approximately 4 hours. When we extrapolate the power consumption of the components 5 years into the future for unchanged functionality, the power consumption of the receiver will be dominated by the RF and ADC. Although overall power consumption for the same functionality is expected to decrease in 5 years time the overall power consumption is still significant. Moreover, additional DR requirements, due to increased interference resulting from a rise in the number of mobile users, will lead to increased power consumption. A moderate 10 dB increase in DR requirements will lead to a 15 dB increase in front end power consumption [14] and a 5 to 10 dB increase in ADC power consumption [37] [40]. Such a moderate increase in DR requirement would completely offset the benefits of miniaturization, and increase the total receiver power consumption to 3.5 to 4 Watts in 5 years time, instead of the estimated 230mW. Moreover, the continued scarcity of battery recourses continues to require ever lower power consumption of all aspects of the mobile device. As LTE-advanced will use similar MIMO technology as IEEE 802.11n for the handheld market, finding solutions that are inherently low power are of prime importance.

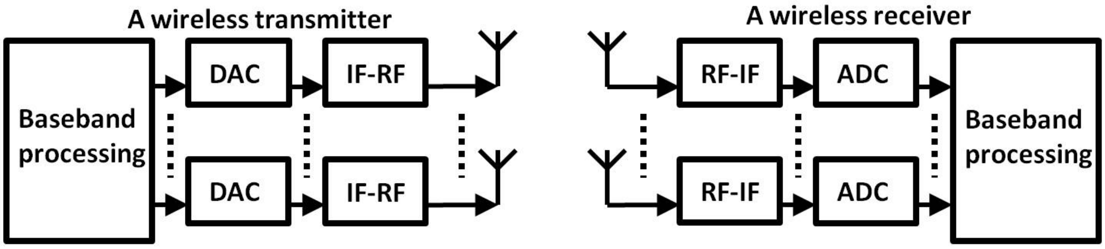

Typical power consumption breakdown in mW

Wireless transmitter

Trend	BB	DAC	RF
State of the art	300	300	500
In 5 years	30	100	400

Wireless receiver

Trend	RF	ADC	BB
State of the art	300	300	300
In 5 years	100	100	30

Figure 2.9: Current MIMO wireless transceiver (transmitter left, and receiver right).

2.7 Summary and Conclusions

Available battery energy in smart phones has remained constant over time. Each battery power density improvement has resulted in a shrinking phone to appeal to consumers. In the meanwhile the screen size has steadily gone up and new standards and functionalities have been added to the phone, reducing the power budget of existing wireless transceivers. Emerging technologies such as OLED and E-paper are expected to vastly reduce screen power consumption, leaving the analog frond end as the main power consumer in the mobile. The new LTE advance standard will use similar MIMO techniques as IEEE 802.11n to increase the data rate of smart phones. Despite the ongoing miniaturization of existing functionality and its corresponding power reduction in handheld devices, the vast increase in number of applications in new generations of smart phones and its subsequent demands on hardware has offset and for now halted the overall trend of weight and size reduction of mobile phones. Moreover, additional DR requirements, due to increased interference resulting from a rise in the number of mobile users, will lead to vastly increased power consumption of the front end. Current state-of-the-art MIMO receivers use about 1 Watt of power in receiving mode. A typical state-of-the-art 4x4 MIMO system can drain a typical smart phone battery in approximately 4 hours. A moderate 10 dB increase of DR requirements to handle increased interference levels, will reduce this to 20 minutes. Reducing MIMO power consumption in handheld devices is therefore of prime importance to increase battery lifetime.

Chapter 3

System Design Considerations for MIMO OFDM Systems

3.1 Introduction

In the previous chapter we have discussed the power trends that dominate mobile devices and MIMO systems. In this chapter we will focus more on the technical background of MIMO systems and try to identify the technical bottlenecks and challenges of designing a MIMO OFDM system.

To create a framework for evaluating the MIMO system, we will start by first addressing the commonly encountered received signal. This signal depends on the transmitted signal and the MIMO communication channel. For now we will use the commonly used Rayleigh fading channel model. In Chapter 6 we will introduce a ray tracer channel model, but for basic understanding of MIMO channels and MIMO capacity, the ray tracer model is not necessary in this chapter. From the received signal we will introduce the MIMO channel capacity model as it was derived by Telatar [2], and Foschini and Gans [3]. After we introduced the received signal, we introduce the state-of-the-art zero-IF receiver which is commonly used in MIMO OFDM systems. From the zero-IF architecture we will introduce common

RF specifications and how they influence one another over a receiver chain. Finally, we will use the capacity equation to help to identify areas of unresolved challenges and opportunities in MIMO OFDM systems.

3.2 Received Signal Model

3.2.1 Legal Transmit Power

From the IEEE 802.11n standard it is known that the legal transmit power limit varies per area and carrier frequency. For example at a 40 MHz bandwidth at 2.4 GHz, the legal transmit power is 23 dBm in Japan, 30 dBm in the USA, and 20 dBm in Europe.

3.2.2 Data Format

In the IEEE 802.11n protocol, the data symbols are preceded by a preamble. During the preamble the receiver is trained and the channel is estimated. In this chapter we assume the channel is time invariant, during the transmission of the data symbols. Such a system is called “packet based”. Figure 3.1 shows the OFDM training structure as is used in the IEEE 802.11 standard. In this figure, t_1 to t_{10} denote short training symbols and T_1 and T_2 denote long training symbols. The preamble is followed by the SIGNAL field and DATA. The SIGNAL field contains information about the modulation and the packet length. The DATA contains the data symbols that the transmitter sends to the receiver. The guard intervals GI and $GI2$ are chosen such that all relevant reflections arrive within a symbol time and there is no inter-symbol interference. In most systems the short training symbols are used to set the analog variable gain amplifiers (VGAs) in the RF of the receiver and the long training symbols are used to do a channel estimate in the digital domain of the receiver.

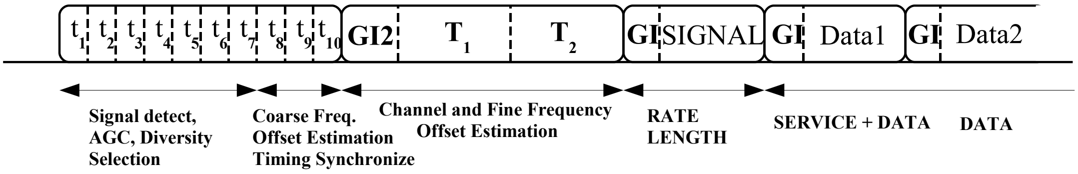

Figure 3.1: OFDM training structure.

3.2.3 OFDM

OFDM is a popular modulation method in wireless communication due to its ability to cope with severe channel conditions. In an OFDM signal, the bandwidth is divided into several subcarriers each having its own data symbol. The baseband equivalent of an OFDM signal over one signal period T_s is expressed as

$$x(t) = \sum_{k=-\frac{K}{2}}^{\frac{K}{2}-1} L_k e^{(i2\pi \frac{kB}{K} t)}, \tag{3.1}$$

where t is time, B is the bandwidth of the signal, K is the number of OFDM frequencies, the symbol time $T_s = \frac{K}{B}$, and L_k is the data symbol of the k^{th} OFDM frequency.

Two functions $x_n(t)$ and $x_m(t)$ are said to be orthogonal over the interval $a < t < b$ if they satisfy the condition

$$\int_{\alpha}^{\beta} x_n(t) x_m^*(t) dt = 0, \tag{3.2}$$

where $m \neq n$. In an OFDM signal the subcarriers are spaced $1/T_{Symbol}$ Hz apart and the time of a data symbol is T_{Symbol}. Because the data symbol time is $T_{Symbol} = \frac{K}{B}$, it is assured the carriers satisfy the orthogonality criterion. This is easily shown with the following equations

$$\int_{\alpha}^{\alpha+T_{Symbol}} x_n(t)x_m^*(t)dt = \int_{\alpha}^{\alpha+T_{Symbol}} e^{(i2\pi f_c)}L_n e^{(i2\pi \frac{nB}{K}t)} e^{(-i2\pi f_c)} L_m^* e^{(-i2\pi \frac{mB}{K}t)}dt$$

$$= L_n L_m^* \int_{\alpha}^{\alpha+T_{Symbol}} e^{(i2\pi(n-m)\frac{B}{K}t)}dt = L_n L_m^* \frac{e^{(i2\pi(n-m)\frac{B}{K}\alpha)}\left(e^{(i2\pi(n-m)\frac{B}{K}T_{Symbol})} - 1\right)}{i2\pi(n-m)\frac{B}{K}} = 0, \tag{3.3}$$

because $m \neq n$ and $e^{(i2\pi(n-m)\frac{B}{K}T_{Symbol})} = 1$. The benefit, of ensuring that the subcarriers are orthogonal, is that these will not interfere with each other. This quality is independent and unaffected by the channel which may exist between the transmitter and receiver; as long as the channel is constant during the symbol time and the guard interval is chosen sufficiently large to prevent inter-symbol interference.

A downside of using an OFDM modulation scheme is that during one symbol time, many, or even all, the sub carriers can ad up constructively, leading to a large peak to average power ratio (PAPR). The large PAPR of OFDM requires a large power back-off in the receiver chain [47]. The power back-off reduces the RF front end efficiency, as the signal is seldom amplified at its full range, thus the amplifier operates at a much lower efficiency. Another downside of the large PAPR is that many ADC levels are seldom used, and as such quantizing the input signal via an ADC often involves more quantization levels and thus more ADC power consumption than strictly necessary.

3.2.4 Noise

The system is affected by white noise. The noise power at a receive antenna is equal to

$$N = 10\log(kTB), \tag{3.4}$$

where k is Boltzmann's constant ($k = 1.38 \cdot 10^{-23}$J/K), T is the equivalent noise temperature of the receiver ($T = 290$ K), B is the noise bandwidth. Assuming a noise bandwidth of 40MHz, the receiver noise power amounts to $N = -128$ dBm.

3.2.5 Channel Model

Since the user uses an OFDM scheme the receiver channelizes the spectrum through the use of an FFT. As a result, the wideband spectrum can be considered as a set of narrowband signals. The channel for a single OFDM subcarrier can be modeled as narrowband Rayleigh fading. Consider a transmission system that consists of N_t transmit antennas and N_r receive antennas. If a narrowband complex transmitted signal vector $\mathbf{s}$ is transmitted, the received signal vector $\mathbf{r}$ can be expressed per subcarrier as

$$\mathbf{r} = \mathbf{H}\mathbf{s} + \mathbf{n}, \tag{3.5}$$

where $\mathbf{H}$ is a $N_r \times N_t$ complex channel-gain matrix and $\mathbf{n}$ is a complex N_r-dimensional additive white Gaussian noise (AWGN) vector. For uncorrelated Rayleigh fading, the entries in $\mathbf{H}$ are independent and identically distributed (i.i.d.), complex, zero-mean Gaussian.

3.3 MIMO Channel Capacity

The conventional way to calculate MIMO channel capacity is expressed by Foschini, Gans [3] and Telatar [2] as:

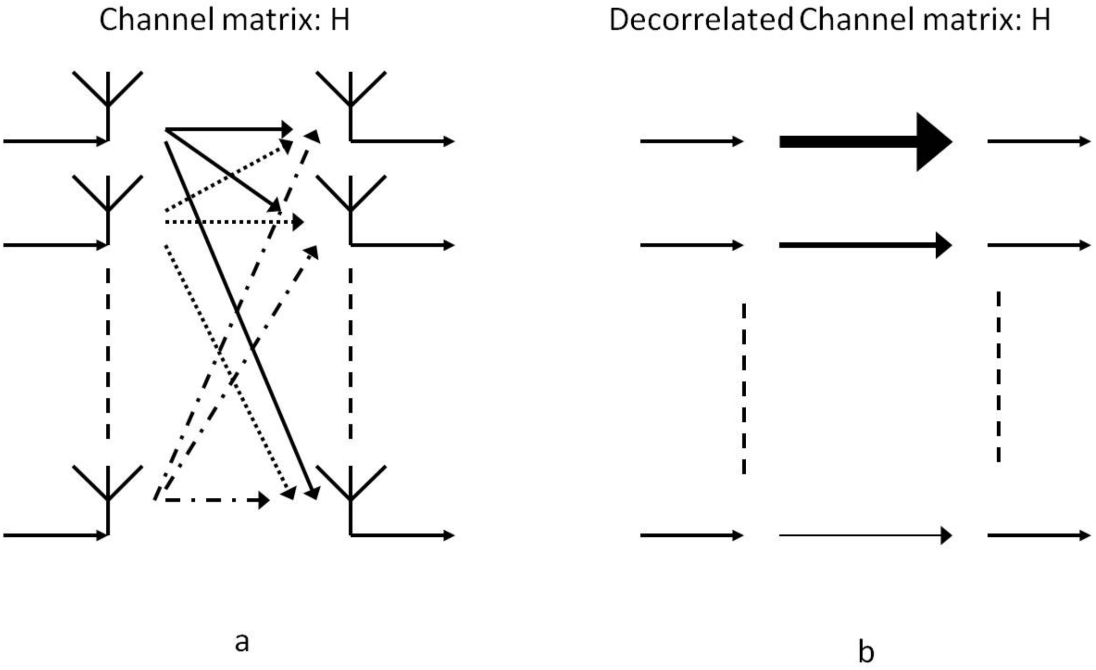

Figure 3.2: The MIMO channel matrix (a) is decorrelated (b) in the digital domain of the MIMO transceiver for every OFDM subcarrier to independent parallel communication channels.

$$C = \max_{\mathbf{K}_s:\mathrm{Tr}[\mathbf{K}_s]\leq P} \mathbb{E}\left[\log_2 \det\left(\mathbf{I}_{N_r} + \mathbf{H}\mathbf{K}_s\mathbf{H}^* \left[N_{th}\mathbf{I}_{N_r}\right]^{-1}\right)\right] \text{ b/s/Hz}, \tag{3.6}$$

where $\mathbf{K_s} = \mathbb{E}[\mathbf{ss}^*]$ is the expected transmit power matrix of size $N_t \times N_t$, and $N_{th}\mathbf{I}_{N_r} = \mathbb{E}[\mathbf{n_{th}n_{th}^*}]$, is the expected thermal noise at the receiver of size $N_r \times N_r$. Commonly the transmit power is distributed equally over the transmit antennas such that $\mathbf{K_s} = P/N_t\mathbf{I}_{N_t}$. The capacity can now be expressed as

$$C = \mathbb{E}\left[\log_2 \det\left(\mathbf{I} + \left(\frac{\rho}{N_t}\right)\mathbf{H}\mathbf{H}^*\right)\right] \text{ b/s/Hz}, \tag{3.7}$$

where $\rho = P/N_{th}$ is the average SNR per receive antenna caused by thermal noise at the antenna, $*$ denotes transpose conjugate and $\mathbf{I}$ denotes the identity matrix. Under the constraint that all transmit power P is divided equally over the transmit antennas, the total power of the complex transmitted signal $\mathbf{s}$ is now constrained to $\mathrm{Tr}[\mathbf{K}_s] = P$.

The capacity of (3.7) can also be expressed as the sum of the Eigen values of $\mathbf{H}$. Writing the capacity as a sum of Eigen values is insightful as it mathematically shows how the data is transmitted via parallel channels. The quality of each parallel channel depends on the value of the Eigenvalue. This also reveals the true power of MIMO when compared to SISO. As mentioned in (1.1) of Section 1.2 the capacity in a SISO system can only be increased by increasing the bandwidth or increasing the transmit power. The MIMO capacity as expressed by (3.6) can be vastly increased by increasing the number of transmit and receive antennas. Via a singular value decomposition (SVD) the Eigen values are derived. The SVD is given by $\mathbf{H} = \mathbf{U_H\Lambda_H V_H^*}$, here $\mathbf{U_H}$ and $\mathbf{V_H^*}$ are unitary matrices ($\mathbf{U_H U_H^*} = \mathbf{I}, \mathbf{V_H^* V_H} = \mathbf{I}$) , and $\mathbf{\Lambda_H} = \mathrm{diag}(\lambda_1, \lambda_2, \ldots, \lambda_K)$, were λ_k^2 is the k^{th} Eigen value of $\mathbf{HH}^*$. The capacity can now be expressed as a sum of Eigen values

$$C = \sum_{k=1}^{K} \mathbb{E}\left[\log_2\left(1 + \lambda_k^2 \frac{\rho}{N_t}\right)\right] \text{ b/s/Hz}. \tag{3.8}$$

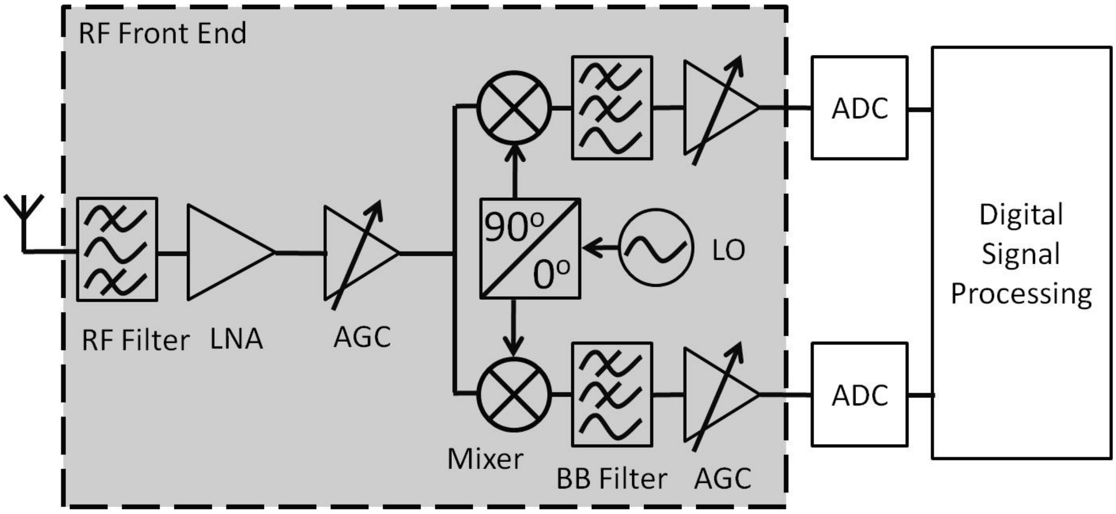

Figure 3.3: Typical zero-IF receiver.

Figure 3.2 graphically illustrates how decorrelation in the digital domain via an SVD creates parallel data transfer channels for each sub carrier. This is called decorrelation as we have transformed the channel matrix $\mathbf{HH}^*$ to a diagonal matrix. The off diagonal elements of $\mathbf{HH}^*$ are a measure of the similarity between the signals along the diagonal. In essence, the larger the off-diagonal elements are compared to the diagonal entries of $\mathbf{HH}^*$, the smaller the Eigenvalues will be. In the extreme case were $\mathbf{HH}^*$ contains only ones, there is only one Eigenvalue of size $\sqrt{N_t N_r}$ and all other Eigenvalues are equal to zero. Such an extreme case only exists if the signal received on each receive antenna is exactly equal. This is only the case if the channel contains no reflectors, and if the distance between the transmitter and the receiver is much larger than the distance between the individual receiver and transmitter antenna elements. The more reflective surfaces the channel contains the lower the correlation will be and thus the higher the MIMO capacity.

3.4 Zero-IF

In most receivers a broad band signal is processed at radio frequency (RF) by the analog front end, where the desired signal only occupies a small portion of the front end bandwidth. To present the desired signal to the baseband (BB) ADC, the analog front end amplifies, down-converts, and filters the received RF broadband signal. Therefore, the first stages of a receiver usually contain strong adjacent channel interferers.

Current state-of-the art MIMO receivers use a zero-IF receiver, also known as a direct conversion receiver, or homodyne receiver. Figure 3.3 depicts a typical zero IF receiver. The RF front end of a zero-IF receiver consists of a low-noise amplifier (LNA), a mixer, and a BB output buffer. The automatic gain control (AGC) behind the LNA prevents saturation of the mixer and BB filter, and the second AGC prevents clipping of the ADC. In a zero-IF receiver the RF signal is down converted directly to BB via a mixer [7]. The simplicity of the zero-IF receiver makes it attractive for compact implementation. One of the benefits of the zero-IF receiver is that the number of RF components is reduced when compared to a heterodyne receiver which uses an IF before final down conversion. Another important benefit is that the BB filter can be a low pass filter with a low Q-factor which allows for easy integration, without the need for external components. A benefit over heterodyne receivers is that there is no need for an image rejection filter. An important downside of direct conversion receivers are the high IP2 requirements, as the IP2 products appear in the IF band. Another downside of direct conversion receivers is that they are susceptible to I and Q imbalance. However, the I and Q imbalance can be corrected in the digital domain [48]. An additional downside of zero-IF receivers is that they are sensitive to DC offset, and require DC offset compensation. To simplify the receiver design the IEEE 802.11 standard has a zero in the BB equivalent spectrum at DC. Despite the difficulties of zero-IF receivers, their simplicity and economic benefits have made them popular and contributed to their widespread use in state-of-the-art receivers.

3.5 Receiver Cascade

As depicted in Figure 3.3 a typical receiver consists of several building blocks. For a zero-IF receiver the main building blocks are an LNA, a mixer, and an

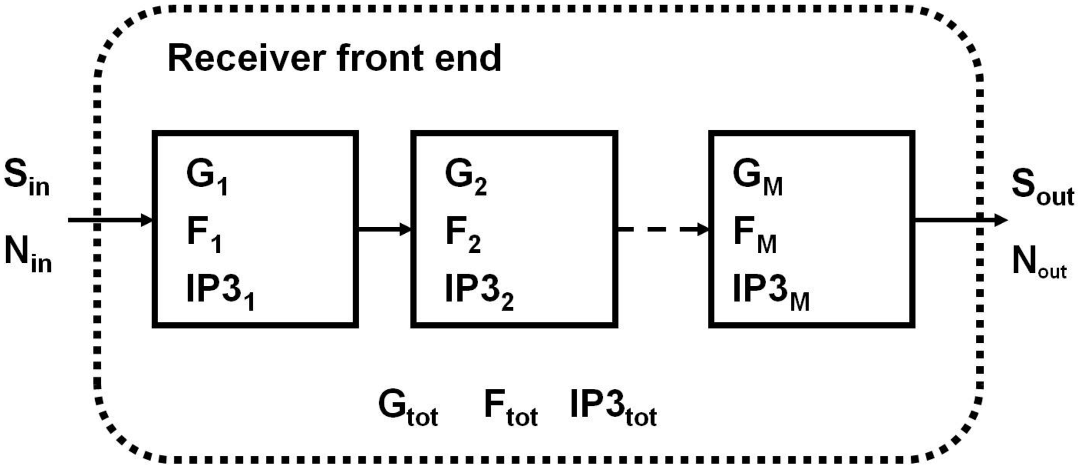

Figure 3.4: Typical receiver cascade.

output buffer. In RF design, these blocks are commonly characterized by their gain G, linearity expressed in the third intercept point $IP3$, and noise contribution expressed in the noise factor F, as is depicted in Figure 3.4. From the specifications of the individual building blocks we can calculate the total specifications of the front end. In this section we will explain G, $IP3$, and F, and provide formulas with which the total receiver specifications can be calculated. In Figure 3.4 S_{in} is the input signal power, S_{out} is the output signal power, N_{in} is the input noise power, and N_{out} is the output noise power.

3.5.1 Gain

In RF design there are several definitions of gain, such as for example power gain, transducer gain, available power gain, maximum power gain, insertion gain, and voltage gain. Due to the plurality of gains it is difficult to compare RF specifications. For example a listed voltage gain of a stage can be made large by deliberately mismatching the in and outputs, while the actual available power gain of the stage is small. Below we will list different definitions of gain. However, in this thesis we will restrict ourselves to the available power gain. We restrict ourselves to the available power gain, because this gain is inherent to the stage and independent of the applied source and load.

Available Power Gain

Available power gain, is defined as the maximum power that can be delivered to the load when the load is matched to the stage, divided by the maximum power that can be delivered to the stage when the source and stage are matched.

$$\text{Available Power Gain } (G): \qquad G = \frac{P_{load,max}}{P_{input,max}} \tag{3.9}$$

Maximum Power Gain

Maximum power gain is defined as the maximum power that can be delivered to the load when the load is matched to the stage, divided by the actual power that is delivered to the stage. By changing the impedance of the source, the maximum power gain can be changed.

$$\text{Maximum Power Gain } (G_M): \qquad G = \frac{P_{load,max}}{P_{input}} \tag{3.10}$$

Transducer Gain

Transducer gain is defined as the actual power that is delivered to the load, divided by the maximum power that can be delivered to the stage when the source and stage are matched. By changing the impedance of the load, the transducer gain can be changed.

$$\text{Transducer Gain } (G_T): \qquad G_T = \frac{P_{load}}{P_{input,max}} \tag{3.11}$$

Power Gain

Power gain is defined as the actual power that is delivered to the load, divided by the actual power that is delivered to the stage. By changing the impedance of the in and output of the stage the power gain can be changed.

$$\text{Power Gain } (G_P): \qquad G_P = \frac{P_{load}}{P_{input}} \tag{3.12}$$

It is interesting to note that when the input and output of the stage are matched to the source and load, the available power gain, the maximum power gain, the transducer gain, and the power gain are equal in value $G = G_M = G_T = G_P$.

Voltage Gain

Voltage gain is defined as the amplitude of the signal expressed in Volt on the load, divided by the amplitude of the input signal expressed in Volt. By changing the in and output impedance the voltage gain is changed as well.

$$\text{Voltage Gain } (G_V): \qquad G_V = \frac{V_{load}^2}{V_{input}^2} \tag{3.13}$$

When the in and output are matched, voltage gain is not necessarily equal to the available power gain. Voltage gain is only equal to the available power gain when the in and output are matched, and the in and output impedance is equal.

Insertion Gain

Insertion gain is defined as the actual power that is delivered to the load by the stage, divided by the actual power that is delivered to the load when the load is directly connected to the source without the stage in between the load and source. The insertion gain can be changed by changing the matching of the load compared to the stage and source.

$$\text{Insertion Gain } (G_I): \qquad G_I = \frac{P_{load,stage}}{P_{load,source}} \tag{3.14}$$

Total Gain

The available power gain, only dependents on the stage itself. Because the available power gain is inherent to the stage itself, it is a suitable measure for stage comparison. The total available power gain of the analog receiver G_{tot} (provided all stages are in and output matched) is given by

$$G_{\text{tot}} = \prod_{m=1}^{M} G_m, \tag{3.15}$$

where G_m is the available power gain of the m^{th} stage in the cascade (Figure 3.4).

3.5.2 Linearity

Third-Order Intercept Point

Analog devices are inherently nonlinear. The nonlinearity of a stage is commonly modeled via the third intercept point $IP3$ [7]. The third-order intercept point is based on the theory that a nonlinear system can be modeled as a Taylor series. The third-order intercept point relates nonlinear products caused by the third order nonlinear term of the Taylor series to the linearly amplified signal. The third-order intercept point is defined as the extrapolated point at which the output power of the third order nonlinearity is equal to the output power of the linearly amplified signal (Figure 3.5). Normally, an amplifier never reaches the intercept point, as it commonly lies beyond the output power an amplifier can deliver. Mathematically

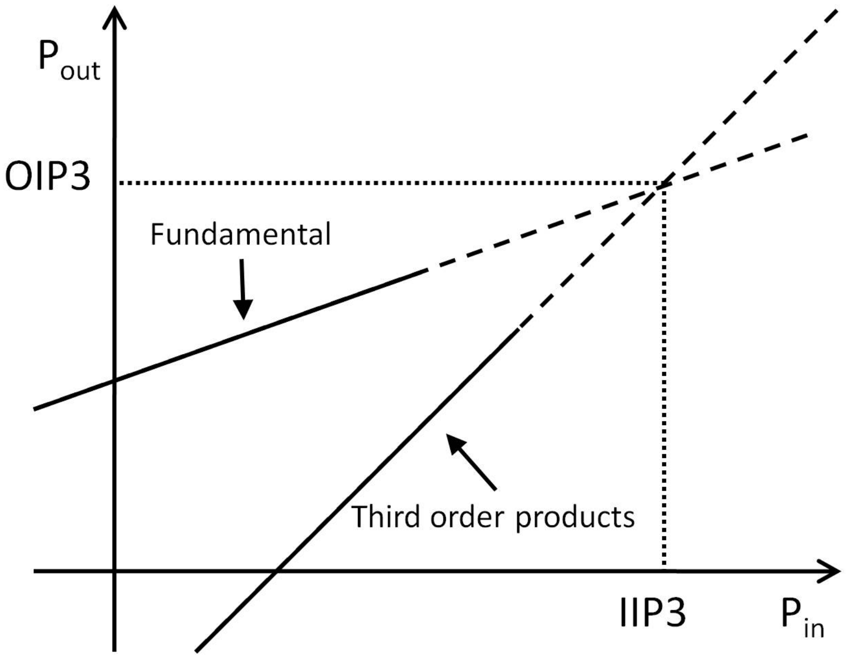

Figure 3.5: Definition of third-order intercept point [7].

the input referred third-order intercept point $IP3$ is defined as

$$IP3 = P_{in}\sqrt{\frac{P_{out}}{P_{Dist}}}, \tag{3.16}$$

where

$$P_{out} = GP_{in}. \tag{3.17}$$

Here G is the gain of the stage, P_{in} is the input power of the the signal, P_{out} is the output power of the linearly amplified signal, and P_{Dist} is the output power of the third order products.

Interference and IP3

A zero-IF receiver receives a wide frequency range at RF. Therefore, the first stages of the receiver usually contain strong adjacent channel interferers, with a priori not fully known statistical properties [6]. These signals need to be handled with adequate linearity to avoid excessive distortion spill-over into the band of the

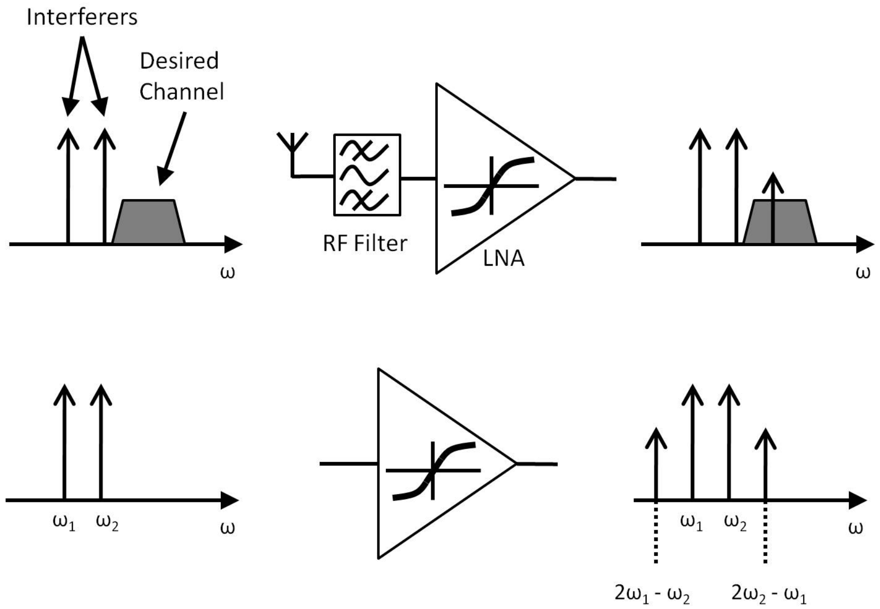

Figure 3.6: Effect of third-order nonlinearity in an LNA [7].

desired signal [7]. As shown in Figure 3.6, when modeling a nonlinear system as a Taylor series, the IP3 of the receiver is a measure of the amount of spill over into the desired band. According to the Taylor series, the third-order frequency components of two single frequency tone interferers of equal power each located in a separate adjacent channel at frequencies ω_1 and ω_2 will appear at equal strength at $2\omega_1 - \omega_2$ and $2\omega_2 - \omega_1$. One of the third-order frequency components, located either at $2\omega_1 - \omega_2$ or $2\omega_2 - \omega_1$, will fall into the desired channel. The power of the distortion P_{Dist} that falls into the desired channel caused by the two single frequency tone interferers can be expressed by

$$P_{Dist} = \frac{GP_{int}^3}{IP3^2}. \tag{3.18}$$

Here the two interferers have equal power and P_{int} is the power of one of the interferers, and G is the available power gain of the considered stage. The application of two single frequency tones is a commonly used method to measure the IP3 of amplifiers.

Total IP3

The total worst case $IP3$ of M stages can be calculated via [17]

$$IP3_{\text{tot}} = \left(\sum_{m=1}^{M} \frac{\prod_{j=1}^{m-1} G_j}{IP3_m} \right)^{-1}, \tag{3.19}$$

under the worst case assumption that all distortion components are in-phase.

To reconstruct the information content of the desired channel, the receiver does not necessarily need to be linear. As long as all the nonlinearities can be accounted for in the BB DSP, the information of the desired channel can be recovered. Because receivers generally need to be low power, the interferers are generally not sampled, but are filtered by non ideal analog components. Therefore, the statistical properties of interferers are generally not known in the BB-DSP and cannot be compensated. To prevent excessive spill-over of the interferers into the desired band, the receiver needs to be linear. However, it is generally known that linearity comes at a power penalty. Therefore, handling an interferer via additional linearity has a cost in terms of additional receiver circuit power. In Chapter 4 we will quantify the relation between interference power levels with which the receiver can cope and receiver circuit power consumption.

3.5.3 Noise Contribution

Next to the distortion signals, the analog front end adds noise to the desired signal. The noise added by the front end originates from the electronics, and is generally much larger than the noise of the channel introduced in Section 3.2.4. The addition of noise by the front end is modeled via the noise figure (NF), and is defined as NF= $10\log_{10}(F_m)$. Here, the noise factor F_m is defined for thermal input noise as:

$$F_m = \frac{\text{SNR}_m}{\text{SNR}_{m+1}}, \tag{3.20}$$

where SNR_m is the SNR at the input, and SNR_{m+1} is the SNR at the output of the m^{th} stage in a cascade. The total noise-factor of M stages in a cascade, F_{tot}, can be calculated via Friis formula

$$F_{\mathrm{tot}} = 1 + \sum_{m=1}^{M} \frac{F_m - 1}{\prod_{j=1}^{m-1} G_j}, \tag{3.21}$$

where F_m the noise-factor of the m^{th} stage and G_j the available power gain of the j^{th} stage. The total noise figure also complies to

$$F_{tot} = \frac{\left(\frac{S_{in}}{N_{in}}\right)}{\left(\frac{S_{out}}{N_{out}}\right)}, \tag{3.22}$$

where S_{in} is the input signal power of the receiver, S_{out} is the output signal power of the receiver, N_{in} is the input noise power of the receiver, and N_{out} is the output noise power of the receiver.

3.6 Analog-to-Digital Converter

The analog signal is finally presented to the ADC for digitization. To prevent aliasing, the ADC is required to sample the analog input signal at least at the Nyquist rate. Because the selectivity of the BB filter of the output buffer is non-ideal there are unwanted left over frequency components of adjacent channels which are also sampled by the ADC. To prevent corruption of the desired channel via aliasing of these unwanted adjacent channel products into the desired channel, the ADC needs to sample at a higher frequency than the Nyquist rate. Moreover, the adjacent channel components generally contain more power than the desired signal. To maintain adequate resolution for the desired channel, additional bits are required in the ADC. These additional bits are called headroom bits. It should be noted that in OFDM systems the term headroom is also commonly used to refer to power back-off due to PAPR. The exact sampling frequency and resolution of the ADC is therefore a function of the required resolution for the desired channel, the BB filter selectivity, and the interference power with which the receiver needs to cope [11]. Unfortunately, the power consumption of an ADC is linear in the sampling rate and exponential in the number of bits. A commonly accepted ADC power model is,

$$P_{\mathrm{ADC}} \sim \kappa_t F_s 2^{b_{\mathrm{ADC}}}, \tag{3.23}$$

where F_s is the sample frequency of the ADC, κ_t a technology constant and b_{ADC} the number of ADC bits [37] [49]. This ADC power model is related to the ADC FOM presented in Section 2.2.2. As mentioned in Section 2.2.2, for ADCs which are limited by thermal noise, the power consumption even scales with twice the number of effective number of bits. Additional headroom bits and a higher sampling frequency, to deal with high interference power levels, are therefore a costly solution in terms of ADC power consumption.

3.7 Design Considerations

Both the receiver front end and the ADC require additional dynamic range (DR) to adequately cope with adjacent channel interference. In most standards the receiver needs to recover the desired signal at high adjacent channel interferer levels. The interference-to-carrier ratio (ICR) as specified by IEEE802.11 is around ICR = 40 dB. However, in reality the ICR values are often even higher [50]. The required additional linearity of the front end comes at increased receiver circuit power. In Chapter 4 we will quantify the relation between ICR and receiver circuit power, and show that the ICR requirement dominates the receiver circuit power consumption. In regard to the ADC, let us assume that at an ICR of 40 dB, the adjacent channel products that are present at the ADC are 40 dB larger than the desired channel. To guarantee sufficient resolution for the desired user in the presence of such large adjacent channel users, additional bits for the ADC are required. In case adjacent channel users of 40 dB larger than the desired user need to be sampled together with the desired user, an additional DR in the ADC of 40 dB is required. This translates to an additional number of bits per ADC of $1/2 \log_2(10^4) = 6.64$ bits, resulting via (3.23) to an overal P_{ADC} increase of 9900%.

From this simple analysis it is clear that handling interferers is a dominant factor in receiver circuit and ADC power consumption. As established in Chapter 2 the receiver circuit and ADC power consumption are expected to be the bottleneck of future wireless transceiver when extending battery lifetime. As such it makes sense to focus on interference reduction to reduce receiver circuit and ADC power consumption.

In Chapter 4 the relation between ICR and receiver circuit power will be presented. In Chapter 5 we will introduce a practical solution that reduces interference power in the RF front end to alleviate the ADC and RF requirements in order to reduce power consumption. Further, in Chapter 5 an IC implementation in 65nm CMOS is given along with proof of concept measurements. In Chapter 6 algorithms are given that control the circuit implementation presented in Chapter 5, and the power savings achieved by the algorithms in terms of ADC bits are quantified.

3.8 Conclusions

OFDM is a popular modulation scheme due to its ability to cope with extreme channel conditions. However, the PAPR of OFDM requires a power back-off in the receiver chain, reducing overall system efficiency. Next to the PAPR of OFDM, interferers pose strong dynamic range requirements on the RF front end and ADC, making them power hungry. In Chapter 2 we have shown that in the absence of disruptive new technologies, the RF front end and ADC power consumption are the future bottlenecks in terms of extending battery lifetime. Mitigating the interferers and thus the dynamic range requirements of the RF front end and ADC has the potential to vastly reduce the power consumption of the ADC and RF front end.

Chapter 4

Optimum Data Transfer Energy Efficiency

4.1 Introduction

The motivation to optimize data transfer energy efficiency (bits/Joule) for a receiver with a limited availability of battery energy is two-fold. As mentioned in Chapters 2 and 3, in many applications the mobile user spends significantly more time receiving data than transmitting. Often, the energy consumed in receiving mode is several orders of magnitudes larger than the energy consumed in transmit mode [12] [13], even if the transmitter circuit power consumption is larger than the receiver circuit power consumption when switched on. Secondly, in a short range link, the transmit power can be relatively small. So the transmit power amplifier is no longer the main power consumer. Yet, the receiver front end often needs to recover a weak signal in the presence of strong adjacent channel interference, which requires highly linear, thus power hungry RF designs. In the absence of disruptive new approaches, we expect that this trend will continue for the foreseeable future.

This chapter is based on work published in [14–16], and aims to quantify the relation between carrier-to-interference ratio (CIR) and the receiver circuit power dissipation. In order to quantify this relation we strive to find an appropriate operation point for each of the analog stages of a power-constrained receiver, such that its user data transfer energy efficiency is maximized per Joule of receiver circuit energy spent. To find the optimum user data transfer energy efficiency we perform the following steps:

1. We find the lowest receiver circuit power consumption for a given set of receiver specifications and for a given IC process according to [17].
2. For a given receiver circuit power budget and for a given IC process we find the maximum throughput expressed in spectral efficiency (bits/s/Hz) by reformulating the results of step 1.
3. For a given bandwidth we calculate the data transfer energy efficiency (bits/Joule) of the maximum possible throughput found in step 2 for various receiver circuit power budgets and CIRs.
4. We use the results of step 3 to find the optimum data transfer energy efficiency and use that result to calculate the relation between receiver circuit power consumption and CIR.
5. We calculate that at large SNR the most power-efficient receiver (in terms of Joule/bit) resulting from step 4 operates at a spectral efficiency near 2.3 bits/s/Hz.

The optimum of step 4 appears to depend mainly on the strength of adjacent channel interference. Therefore, the optimum serves to quantify the relation between CIR and receiver circuit power dissipation. Too low receiver circuit power would lead to a highly non-linear receiver, hence strong distortion and low throughput. Too high values of receiver circuit power would create an unnecessarily linear receiver, which cannot be exploited because of the finite signal-to-channel-noise ratio of the received signal. Yet even with very large signal-to-noise ratios, it appears to be more energy efficient to use a receiver with modest linearity. There appears to be an optimum choice of the distribution of gain, noise figure and linearity along the cascade, which yields the highest user data transfer energy efficiency. For very low available receiver circuit power, our results imply that a duty cycle strategy is more efficient than continuous operation. In these cases the receiver is proposed to operate in bursts.

A commonly used direct-conversion receiver architecture as presented in Section 3.4 is used in our analysis. As mentioned in Section 3.4, in most receivers a broad band signal is processed at radio frequency (RF) by the analog front end, where the desired signal only occupies a small portion of the front end bandwidth. The analog front end amplifies, down-converts, and filters the received RF broadband signal in order to present the desired signal to the baseband (BB) ADC. Because final channel selection usually occurs at a later stage, the first stages of our receiver usually contains strong adjacent channel interferers, with a priori not fully known statistical properties [6]. To avoid excessive distortion spill-over into the band of the desired signal these signals need to be handled with adequate linearity [7]. Generally, a higher linearity requirement leads to a higher power consumption of the analog circuit. Conventionally, the linearity is fixed in RF designs and specified for the highest power of the interference at which the receiver should still operate. This results in an overly linear design at all lower values of the interference power, reducing battery lifetime unnecessarily. Most RF designs are based on a set of system specifications, determined by standardization [7], such specifications may include packet error rates, sensitivity and modulation. An RF designer than strives to design a receiver at the lowest power possible, for this target [8, 9].

Conversely, we want to determine the maximum data transfer energy efficiency (bits/Joule) possible in terms of bits/s per unit of available receiver circuit power budget (Joule/s). To formulate this optimum we do not a priori fix the system specifications, such as the modulation constellation. Rather, we assume that the key RF receiver specifications, IP3, gain, and noise figure, are adaptive. The maximum data transfer energy efficiency might seem to depend on a large number of independent variables, but for a given IC process, several design performance indicators have known achievable values [17]. This reduces the number of independent variables which determine the optimum of the throughput in terms of spectral efficiency [14]. We conclude that at large SNR, the most power-efficient receiver (in terms of Joule/bit) will operate near 2.3 bits/s/Hz. We give an expression for its power consumption in (4.35).

4.2 Modeling System Data Transfer Energy Efficiency

To operate a wireless network at the highest data transfer energy efficiency possible, in terms of bits per second per unit of receiver circuit power, we strive to find the receiver circuit power $\widehat{P_r}$ at which the throughput T (bits/s/Hz) is maximized for a given bandwidth B using

$$\widehat{P_r} = \arg\max_{P_r}\left(\max_{P_1 \ldots P_M : \sum P_m = P_r}\left(\frac{BT}{P_r}\right)\right) \qquad [Joule/s]. \tag{4.1}$$

That is, we search the most efficient receiver circuit power budget. The inner optimization for a given receiver circuit budget with $\sum P_m = P_r$ is given by

$$\widehat{T} = \max T \mid_{\sum P_m = P_r} \qquad [bits/s/Hz], \tag{4.2}$$

here P_m is the power allocated to the m^{th} stage of a receiver circuit. The maximum is taken over all possible settings of the RF stages, provided that the total consumed power does not exceed P_r. We use the capacity expression

$$T = \log_2\left(1 + \frac{S}{N_{tot}}\right) \qquad [bits/s/Hz], \tag{4.3}$$

as a measure of achievable throughput T. Here S is the input signal power. Yet, T should not be interpreted as the Shannon capacity of the system in information theoretic sense: if the sampling and ADC circuits are allowed to capture the entire band, including the interference signal, the distortion can be predicted by the BB DSP and its effect can be eliminated, at least from an information theoretical perspective. Hence one could design a receiver that has higher throughput than the value found in (4.3). An example of such an architecture is a receiver were the ADC samples the antenna RF signals directly. However, such a receiver architecture would be at odds with our ambition to minimize the receiver circuit power consumption. Conventional receiver architectures reduce power consumption by using analog frequency selectivity to relax the dynamic range requirements of the front end and the ADC. Lacking a better model, we define the throughput T as in (4.3). The total noise plus distortion, relative to power levels at the input, is

$$N_{\text{tot}} = N_{th} + \frac{N_r}{G_{\text{tot}}} + \frac{N_d}{G_{\text{tot}}}, \tag{4.4}$$

where N_{th} is the noise in the channel, N_r the electronics noise added by the analog circuits of the receiver, and N_d is the distortion caused by an interferer. Other RF impairments such as LO leakage, DC leakage and images are not considered, since they are related to the architecture, topology and layout, which are beyond the scope of this chapter. The AWGN noise in the channel is defined as in Section 3.2.4 and is given by $N_{th} = kTB$. where $k = 1.38 \times 10^{-23}$ is Boltzmann's constant, T is the temperature and B is the bandwidth of the desired signal. Further, G_{tot} is the total available power gain of the analog receiver as defined in Section 3.5 and is given by

$$G_{\text{tot}} = \prod_{m=1}^{M} G_m, \tag{4.5}$$

where G_m is the gain of the m^{th} stage in the cascade (Figure 4.1). We now need a more detailed model of N_d and N_r.

4.2.1 Distortion and Noise

Here we recapitulate part of Section 3.5, but contrary to Section 3.5 the interference is not modeled as two single frequency tones. As mentioned in the introduction of this chapter, the first stages of our receiver usually contain strong adjacent channel interferers, with a priori not fully known statistical properties [6]. These signals need to be handled with adequate linearity to avoid excessive distortion spill-over into the band of the desired signal [7]. Because the statistical properties of the interferers are a priori not fully known, the distortion spill-over in the band of interest is experienced by the receiver as noise. Here, we obtain the distortion power N_d in (4.4) via the third order input referred intercept point $IP3$. The $IP3$ is a measure of the linearity of the analog circuits in the receiver [7]. Total $IP3$, $IP3_{tot}$, is defined as in Section 3.5 and is given by

$$IP3_{tot} = P_{int}\sqrt{\frac{P_{out}}{N_d}}, \tag{4.6}$$

where P_{out} is the output power in the channel of the interferer due to the received channel interference power P_{int}. $IP3_{tot}$ corresponds to the extrapolated input power at which P_{out} and N_d are equal. For an analog receiver the output power is $P_{out} = G_{\text{tot}}P_{in}$, with P_{in} the input power. Therefore we can substitute P_{out} in (4.6) by $G_{\text{tot}}P_{int}$. The distortion products of the interferer which appear in the desired channel can now be expressed as

$$N_d = \frac{G_{\text{tot}}P_{int}^3}{IP3_{\text{tot}}^2}. \tag{4.7}$$

We simplify our model by assuming that, after further channel selectivity filtering, Nyquist sampling and A/D conversion, the baseband processing engine of the receiver has no further knowledge of this distortion signal, and experiences it as AWGN [51]. The total worst case $IP3$ of M stages can be calculated via [17]

$$IP3_{\text{tot}} = \left(\sum_{m=1}^{M} \frac{\prod_{j=1}^{m-1} G_j}{IP3_m}\right)^{-1}, \tag{4.8}$$

under the worst case assumption that all distortion components are in-phase. Here $IP3_m$ is the third order intercept point of the m^{th} stage.

Next to the distortion signals, the analog front end adds noise N_r to the desired signal. This addition of noise is modeled via the noise figure (NF), and is defined as NF= $10\log_{10}(F_m)$. Here, the noise factor F_m is defined for thermal input noise as:

$$F_m = \frac{\text{SNR}_m}{\text{SNR}_{m+1}}, \tag{4.9}$$

where SNR_m is the SNR at the input, and SNR_{m+1} is the SNR at the output of the m^{th} stage in a cascade. Note that the noise figures do not model the contribution by distortion. The total noise-factor of M stages in a cascade, F_{tot}, can be calculated via Friis formula

$$F_{\text{tot}} = 1 + \sum_{m=1}^{M} \frac{F_m - 1}{\prod_{j=1}^{m-1} G_j}, \tag{4.10}$$

where F_m the noise-factor of the m^{th} stage and G_j the gain of the j^{th} stage.

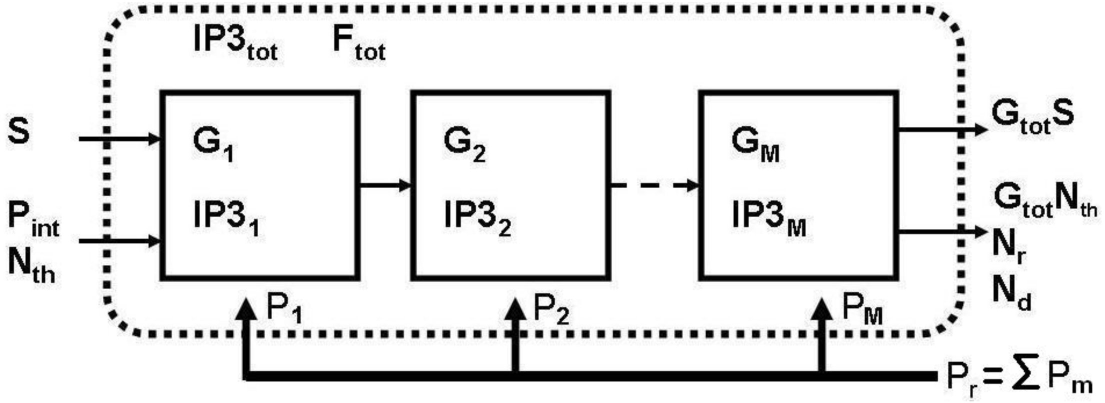

Figure 4.1: *Power consumption P_r in a receiver, to be optimized by adapting the $IP3$ and Gain G of each of the M stages.*

Moreover, the total noise factor must satisfy

$$F_{\mathrm{tot}} = 1 + \frac{N_r}{G_{\mathrm{tot}} N_{th}} \tag{4.11}$$

where G_{tot} is the total gain of the analog circuit and N_r is the variance of the electronics noise added by all analog circuits weighed with the partial gains. The electronics noise can now be expressed as

$$N_r = \left(F_{tot} - 1\right) N_{th} G_{tot} \tag{4.12}$$

By combining (4.4) (4.7) and (4.12), the total noise plus distortion, normalized to power levels present at the input, is now given by

$$N_{\mathrm{tot}} = F_{\mathrm{tot}} N_{th} + \frac{P_{int}^3}{IP3_{\mathrm{tot}}^2}, \tag{4.13}$$

where $IP3_{tot}$ follows from (4.8) and F_{tot} from (4.10). Figure 4.1 now depicts the receiver model, where every individual stage has variable gain ($G_1, \cdots, G_M$) and IP3 ($IP3_1, \cdots, IP3_M$), thus allowing for variable $IP3_{tot}$ and variable F_{tot} of the receiver cascade.

4.2.2 Optimum Throughput

To find the optimum data transfer energy efficiency, we first optimize the throughput for a given receiver circuit power budget. In [14] our aim is to optimize the power budget P_r over the various stages such that throughput T is optimum under the constraint of a given technology, a given received power S, total gain G_{tot} needed to drive the ADC and channel parameters N_{th} and P_{int}. In [14] we first addressed how for a chosen F_{tot} and $IP3_{\text{tot}}$ one can optimize the power budget P_r by optimally distributing the gains $(G_1, \cdots, G_M)$ and $IP3$'s $(IP3_1, \cdots, IP3_M)$ over the cascade. In fact, this is a mathematical formalization of a commonly encountered design problem in RF design, of optimizing each circuit block to meet a given spec for the receiver. In [17] a double Lagrangian tool is proposed for this exercise, to solve the distribution of the gains and $IP3$ for the cascade. Paper [9] summarizes [17] for $M = 2$. This Minimum-Power Cascade Optimization (MPCO) solves:

$$P_{\text{min}} = \min \left(\sum_{m=1}^{M} P_m \right), \tag{4.14}$$

where P_m is the power dissipation of circuit block m, as will be covered by (4.17). In [14] we extend the MPCO by further optimizing F_{tot} and $IP3_{\text{tot}}$ to satisfy our end goal of maximizing the throughput, thus searching for

$$\widehat{T} = \max_{F_{\text{tot}},\, IP3_{\text{tot}}} (T), \tag{4.15}$$

where the available receiver circuit power P_r, satisfies $P_r = P_{min}$ as in (4.14). This is achieved by expressing the power optimal $IP3_{\text{tot}}$, called $\widehat{IP3}_{\text{tot}}$, as a closed form function (4.22) of the figure of merits related to the used IC design process, the available receiver circuit power P_r, the power optimal total noise factor $\widehat{F}_{\text{tot}}$ and total gain G_{tot}. Therefore, we can write N_{tot} as a function of $\widehat{F}_{\text{tot}}$ and the available receiver circuit power P_r. Our claim is that in the end the maximization in (4.15), for a given power budget P_r, is equal to minimizing the total noise according to

$$\widehat{N}_{\text{tot}} = \min_{F_{\text{tot}}} \left(N_{tot} \left(\widehat{IP3}_{\text{tot}}(F_{\text{tot}}) \right) \right). \tag{4.16}$$

We call this a Maximum-Throughput Cascade Optimization Method (MTCO).

4.2.3 Minimum-Power Cascade Optimization Method

Linearity Factor Model

A commonly used equivalent figure of merit (EFOM) [17] is

$$P_m = \frac{f_m G_m \, IP3_m}{\kappa_m}, \tag{4.17}$$

where f_m is the power limiting bandwidth and κ_m is the power linearity factor of the m^{th} stage. The most appropriate parameter to choose for f_m highly depends on the circuit functionality. For LNAs with a dominant pole, the bandwidth is an appropriate choice. By using an EFOM, P_m theoretically does not depend on the noise figure F_m. By using structure independent transforms (SIT), it is possible to trade IP3, gain and power dissipation, to transform a chosen topology for each circuit block to a circuit with the optimal specification [52]. Creating a topology that can also change $IP3$ adaptively and stil meet (4.17) is a topic of current IC design research.

Dual Lagrange Optimization Method

So,

$$P_{\min} = \min_{\substack{G_1, \, \cdots, \, G_M \\ IP3_1, \, \cdots, \, IP3_M}} \left(\sum_{m=1}^{M} \frac{f_m}{\kappa_m} G_m \, IP3_m \right), \tag{4.18}$$

while achieving the G_{tot} using (4.5), $IP3_{\text{tot}}$ using (4.8), and F_{tot} using (4.10). In this optimization process, the f_m, κ_m and F_m of a cascade are taken as constant. The individual F_m is kept constant because the F_m is limited by the topology and used IC process technology. A closed form expression [17] for the minimal analog signal conditioning (ASC) power dissipation as a function of the overall noise factor F_{tot} is,

$$P_{\min} = IP3_{\text{tot}} \left(\sqrt{F_e} + \sqrt{\frac{F_w}{(F_{\text{tot}} - F_1)}} \right)^2 , \tag{4.19}$$

where the "weighed excess noise factor" F_w is defined as

$$F_w = \left(\sum_{m=1}^{M-1} \sqrt[3]{\frac{f_m}{\kappa_m}(F_{m+1} - 1)} \right)^3 . \tag{4.20}$$

Here the excess noise factor of the final stage is

$$F_e = \frac{f_M}{\kappa_M} G_{\text{tot}}, \tag{4.21}$$

which is a fixed value.

4.2.4 Maximum-Throughput Cascade Optimization Method

While (4.19) gives the minimum power P_{min} needed to satisfy a required $IP3_{tot}$, we can conversely claim that the best $\widehat{IP3}_{\text{tot}}$ that one can achieve for a given available P_r equals

$$\widehat{IP3}_{\text{tot}} = P_r \left(\sqrt{F_e} + \sqrt{\frac{F_w}{(F_{\text{tot}} - F_1)}} \right)^{-2} . \tag{4.22}$$

Now, we can rewrite the total noise (4.4) as a function depending on F_{tot}, P_{int} and P_r

$$N_{\text{tot}} \quad = F_{\text{tot}} N_{th} + \tfrac{P_{int}^3}{P_r^2} \left(\sqrt{F_e} + \sqrt{\tfrac{F_w}{(F_{\text{tot}} - F_1)}} \right)^4 , \tag{4.23}$$

By combining (4.2), (4.3), (4.4), and (4.23), we can maximize T by minimizing N_{tot}. We require that

$$\left. \frac{dN_{\text{tot}}(F_{\text{tot}})}{dF_{\text{tot}}} \right|_{F_{\text{tot}} = \widehat{F}_{\text{tot}}} = 0, \tag{4.24}$$

and obtain $\widehat{F}_{\text{tot}}$ as $\widehat{F}_{\text{tot}} =$

$$F_1 + \frac{4F_w}{\left(-\sqrt{F_e} + \sqrt{F_e + 2^{5/3}\left(F_w N_{th}\frac{P_r^2}{P_{int}^3}\right)^{1/3}}\right)^2}. \tag{4.25}$$

Applying this value of $\widehat{F}_{\text{tot}}$ means that (4.12) turns into $N_r/G_{\text{tot}} =$

$$(\mathrm{F}_1 - 1)\,N_{th} + \frac{4F_w N_{th}}{\left(-\sqrt{F_e}+\sqrt{F_e+2^{5/3}\left(F_w N_{th}\frac{P_r^2}{P_{int}^3}\right)^{1/3}}\right)^2}, \tag{4.26}$$

and (4.7) turns into $N_d/G_{\text{tot}} =$

$$\frac{P_{int}^3}{P_r^2}\frac{1}{16}\left(\sqrt{F_e} + \sqrt{F_e + 2^{5/3}\left(F_w N_{th}\frac{P_r^2}{P_{int}^3}\right)^{1/3}}\right)^4, \tag{4.27}$$

which we insert in (4.3) and (4.4). We now have found an analytically closed-form solution which maximizes the throughput for a given circuit power budget P_r. We also found closed-form solutions for $\widehat{F}_{\text{tot}}$ and $\widehat{IP3}_{\text{tot}}$ that achieve the optimum throughput, respectively (4.25) and (4.22) with (4.25) inserted. The individual gain ($G_1, \cdots, G_M$) and $IP3$ ($IP3_1, \cdots, IP3_M$) per stage follow from [17]. In Section 4.3 we give an example of MPCO to motivate our search for the MTCO, calculating the efficiency in terms of bits/Joule for a target $NF_{tot} = 2$ dB, with firstly $IP3_{tot} = -40$ dBm, and secondly $IP3_{tot} = -20$ dBm. Surprisingly, in our scenario, the data transfer energy efficiency at $IP3_{tot} = -40$ dBm is more than an order of magnitude larger than at $IP3_{tot} = -20$ dBm, namely 4.4 Gbit/Joule and 0.3 Gbit/Joule, respectively. The difference in P_r is 8 dBm (5.9 mW) versus 28 dBm (590 mW), respectively.

4.2.5 Variable Third Order Intercept Point

With increasing interference power P_{int} both the second and third noise term in (4.4) will increase. The second term increases, because to mitigate a more powerful interferer, more linearity is required so noise figure often is sacrificed.

The third noise contribution increases as a function of P_{int}, as a more powerful interferer means more distortion. The only option to meet target specifications is to make more receiver circuit power available. Conversely, a weaker interferer can be handled with less power in the analog circuits.

In conventional RF design, the total $IP3$ is determined by a worst case channel to interference ratio (CIR) as defined by the standard, where

$$\mathrm{CIR} = \frac{S}{P_{int}}. \tag{4.28}$$

An example of a common value for the CIR in the IEEE 802.11b standard at which the receiver should still operate is -40 dB. However, as mentioned in Section 3.7, in reality the CIR requirements are often even more stringent [50]. This implies that a conventional design wastes power to achieve a certain linearity, when the actual value of the CIR is lower than the worst case.

A variable $IP3$ setting in the receiver adds an additional degree of freedom and allows the power consumption of the receiver to lower. The receiver can now adapt itself to the instantaneous value of the CIR, instead of to the worst case required by the standard. In the MTCO the optimal throughput of the system as a function of the available receiver and interference power is calculated. Figure 4.2 shows the simulation results for the system specifications of Table 4.4, $S/N_{th} = 30$ dB, $k = 1.38 \times 10^{-23}$, $T = 295$ K, $G_{tot} = 65$ dB, and $B = 22$ MHz. The circuits of Table 4.4 originate from a circuit library which is given in Tables 4.1, 4.2, and 4.3. In Figure 4.2 it can be seen that a reduction of the CIR of 20 dB allows for a reduction of the power consumption of 30 dB for a given target rate. The factor $\frac{3}{2}$ relation between CIR and P_r follows from (4.7).

This implies that a receiver with adaptive $IP3$ could opportunistically scale back the $IP3$, in the absence of large interferers, to operate in a substantially lower power mode, potentially orders of magnitudes. We recognize that this can be a challenge in IC design as changing the $IP3$ typically also changes in and output impedances of receiver stages which in turn can lead to a power mismatch, which can reduce the aforementioned benefits. An implicit relation between interference and receiver circuit power consumption was reported earlier [6–9, 17], but now we have quantified this relation. We have reported this result in literature in [14–16].

4.2.6 Maximum Data Transfer Energy Efficiency

The data transfer energy efficiency observes an optimum, as depicted in Figure 4.3. The location of the optimum is technology-dependent and directly relates to the linearity factors κ. The optima as in Figure 4.3 are depicted in Figure 4.4 for different values of CIR. These form a straight line on a logarithmic scale, with an angle of the line being $\alpha = -\frac{3\text{dBm}}{2\text{dB}}$, due to (4.7). Therefore, we only need to find one optimum to calculate all other optima for different CIR. This relation can be expressed as

$$\mathrm{P}_{opt} = \mathrm{P}_{opt,\,0\mathrm{dB}} - \alpha \mathrm{CIR}, \tag{4.29}$$

where $\mathrm{P}_{opt,\,0\mathrm{dB}}$ is the optimum at $CIR = 0$dB and P_{opt} is expressed in dBm and CIR in dBs.

We now derive the throughput related to the maximum data transfer energy efficiency in Figure 4.3, the throughput T corresponding to

$$\widehat{T}_{MT} = \max_{P_r} \frac{\widehat{BT}}{P_r} \tag{4.30}$$

The corresponding value of T is now called the maximum data transfer energy efficiency throughput $\widehat{T}_{MT}$. Results are plotted in Figure 4.5. As can be observed in Figure 4.5, $\widehat{T}_{MT}$ converges to an upper limit for high values of the SNR. For large values of SNR we can simplify Equation (4.3) with (4.26) and (4.27) inserted via (4.4) to

$$\lim_{SNR \to \infty} T = \log_2 \left(1 + \frac{S P_r^2}{P_{int}^3 (\frac{f_n}{\kappa_n} G_{tot})^2} \right). \tag{4.31}$$

We are interested in finding $\widehat{T}_{MT}$. Thus solving

$$\frac{\delta}{\delta P_r} \left(\frac{\log_2(1 + \alpha P_r^2)}{P_r} \right) = 0, \tag{4.32}$$

where

$$\alpha = \frac{S}{P_{int}^3(\frac{f_n}{\kappa_n}G_{tot})^2}, \tag{4.33}$$

yields,

$$2\sigma - (1+\sigma)\ln(1+\sigma) = 0, \tag{4.34}$$

where $\sigma = \alpha P_r^2$. A numerical approximation for σ yields $\sigma = 3.9$, and the limit of $\widehat{T}_{P_r}$ at large SNR is $\widehat{T}_{P_r} = 2.3$ bits/s/Hz. The P_r corresponding to $\widehat{T}_{P_r}$ at large SNR, $\widehat{P_r}$, is given by

$$\widehat{P_r} = \sqrt{\sigma}\sqrt{\frac{P_{int}^3}{S}}\left(\frac{f_n}{\kappa_n}G_{tot}\right) \tag{4.35}$$

A conclusion is that we showed the most power efficient receiver in terms of Joule/bit at large SNR will operate near 2.3 bits/s/Hz and its power consumption has been calculated in (4.35). Interestingly this limit is independent of the used IC technology. However, the optimum power efficiency for lower SNR values does depend on IC technology. At high SNR the receiver is limited by the distortion noise caused by the interferer. When the power budget of the receiver circuit is increased the data transfer energy efficiency is initially increased via the MTCO, as the noise figure is improved which is required to lift the signal above the noise floor. Increasing the power budget further decreases the data transfer energy efficiency obtained via MTCO. This is because the data rate can now only be increased by increasing the linearity. Unfortunately, there is a non-linear relation between linearity and power consumption which causes the data transfer energy efficiency to decrease.

We believe this result is significant. A system designer can fix the modulation and coding method to 2.3 bits/s/Hz irrespective of the channel and interference conditions. Moreover the transmitter does not need to know the IC technology used for the receiver, because the optimum is independent of IC technology. The receiver then adapts G, $IP3$, but there is no need to adapt transmitter settings. By fixing the throughput to 2.3 bits/s/Hz we are generally well below the available channel capacity for high SNR ($\log_2(1+S/N_{th})$). Therefore, we effectively exchange excess transmit power of for example a mains powered base station for maximal receiver circuit data transfer energy efficiency in a handheld device. An additional argument is that for most wireless network applications, mobile users spend only a short amount of time transmitting. Thus the energy consumed for receiving is orders of magnitudes larger than for transmitting [12] [13]. From this perspective it makes sense to focus on reducing the receiver circuit energy consumption.

4.2.7 Duty Cycling

A strategy to operate at the optimal data transfer energy efficiency and to achieve lower average power consumption is duty cycling. The receiver operates at the optimal data transfer energy efficiency and switches on and off according to the available circuit power. Via (4.3), (4.4), (4.26), and (4.27) the throughput which corresponds to the maxima of the data transfer energy efficiency curves in Figure 4.3 is calculated, results are shown in Figure 4.5. Interestingly, the throughput corresponding to the optimum data transfer energy efficiency is independent of the CIR. However, the receiver circuit power required to achieve this throughput is not (Figure 4.4). At large SNR this relation is given by (4.35).

However, in systems with very short duty cycles, the overhead for short packages can be prohibitive. In such cases there exists a tradeoff between the delay for merging packets versus the optimal power consumption. Furthermore, at the right hand side of the optimum, the throughput T expressed in bit/s/Hz can increase by making more circuit power available. However, the data transfer energy efficiency BT/P_r expressed in bits/Joule cannot increase if a more power consuming circuit is used. Designing for better linearity than, the linearity needed to accommodate a crude modulation of 2.3 bit/s/Hz, does not pay off.

4.3 Numerical Results

We first start with an example of the traditional Minimum Power Cascade Optimization (MPCO), and show how this can lead to a non-optimum system in terms of data transfer energy efficiency. As an example the target specifications for the MPCO are $NF_{tot} = 2$ dB, with first $IP3_{tot} = -40$ dBm, and secondly

Table 4.1: κ_m *for various LNA circuit designs in 90 nm CMOS.*

LNA	[53]	[54]	[55]	[56]	[56]
NF [dB]	3.4	4.4	1.7	2.0	3.0
BW [GHz]	$4.1^{\dagger}$	19.9	1.5	$6.0^{\dagger}$	$4.0^{\dagger}$
Gain [dB]	12.4	12.7	16	15	14
IIP3 [dBm]	-1	-2.5	4.0	-2.3	5.6
Pdc [mW]	9.0	12.6	19.6	19.2	19.2
κ_m $[10^9]$	6.50	18.0	7.65	6.01	19.0

LNA	[57]	[58]	[59]	[60]	[61]
NF [dB]	4.4	2.1	2.9	3.6	6.5
BW [GHz]	$5^{\dagger}$	$0.6^{\dagger}$	1.35	1.14	8
Gain [dB]	13.5	13.4	12.3	8.1	14.1
IIP3 [dBm]	$-8^{\ddagger}$	-10	-2.7	-7.25	$-1.7^{\ddagger}$
Pdc [mW]	4.0	1.2	9.72	1.0	86
κ_m $[10^9]$	4.91	1.18	1.33	1.48	1.62

† Estimated from the calculated maximum Power Gain.

‡ Estimated from the 1 dB compression point.

Table 4.2: κ_m *for various Mixer circuit designs in 90 nm CMOS.*

Mixer	[62]	$[63]^{\dagger}$	[64]
NF [dB]	17.4	11.5	9.1
f_m **[GHz]**	20	3.85	2.1
Gain [dB]	3.2	12.1	10.2
IIP3 [dBm]	-2.1	$-2.8^{\ddagger}$	10.7
Pdc [mW]	1.8	9.78	14.5
κ_m	$14.3 \cdot 10^9$	$3.35 \cdot 10^9$	$17.8 \cdot 10^9$

† Merged Mixer and LNA.

‡ Estimated from the 1 dB compression point.

Table 4.3: κ_m *for various Output buffer circuit designs in 90 nm CMOS.*

Buffer	[65]	[66]	[67]
NF [dB]	16	26.5‡	25
f_m **[MHz]**	500	10	2
Gain [dB]	0	67.5†‡	14†
IIP3 [dBm]	19	-52.5	-4
Pdc [mW]	32.5	13.3	1
κ_m	$1.22{\cdot}10^9$	$2.37{\cdot}10^7$	$2.00{\cdot}10^7$

Buffer	[68]	[69]	[69]
NF [dB]	12.3‡	17	30
f_m **[MHz]**	0.24	2200	2200
Gain [dB]	33†	-10†	50†
IIP3 [dBm]	-18	-3	-45
Pdc [mW]	23.8	2.5	2.5
κ_m	$3.19{\cdot}10^5$	$4.40{\cdot}10^7$	$2.78{\cdot}10^9$

† Voltage gain.

‡ Estimated from data.

Table 4.4: *Typical design choices for cascades in an ASC (LNA [55], Mixer [64], and Output buffer [65]). Where, numbers denoted in italics are considered as variable in this chapter.*

	LNA	**Mixer**	**Buffer**
NF [dB]	1.7	9.1	16
Gain [dB]	*16*	*10.2*	*0*
IIP3 [dBm]	*4*	*10.7*	*19*
κ_m	$7.65{\cdot}10^9$	$17.8{\cdot}10^9$	$1.22{\cdot}10^9$
f_m **[MHz]**	100	2500	22

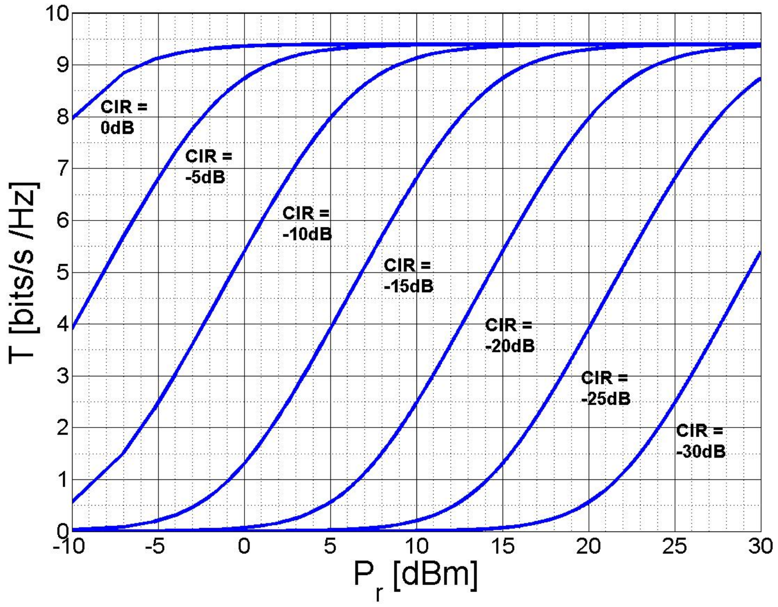

Figure 4.2: *Achievable Throughput (bit/s/Hz) for different values of CIR due to adjacent channel interference, versus available receiver circuit power* P_r *for a WLAN-like system in 90 nm CMOS.*

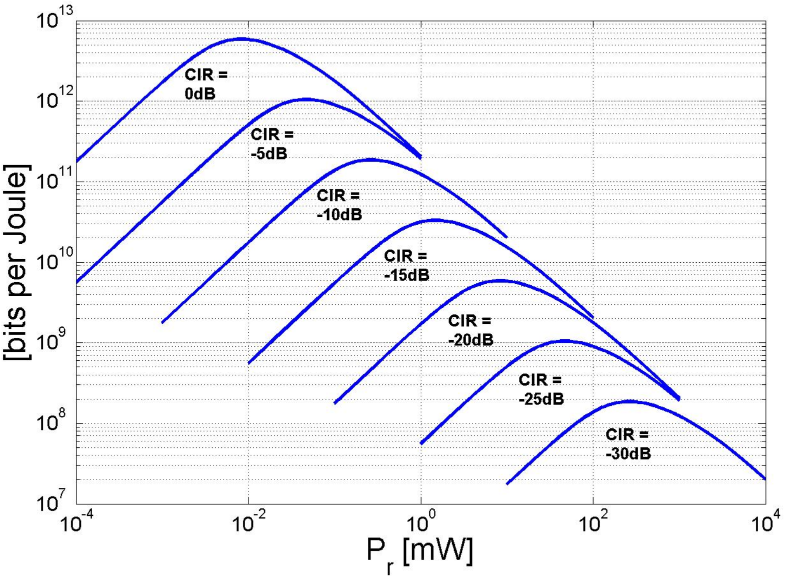

Figure 4.3: *Data transfer energy efficiency (bits/Joule) for different values of CIR due to adjacent channel interference, versus receiver circuit power* P_r *for a WLAN-like system in 90 nm CMOS.*

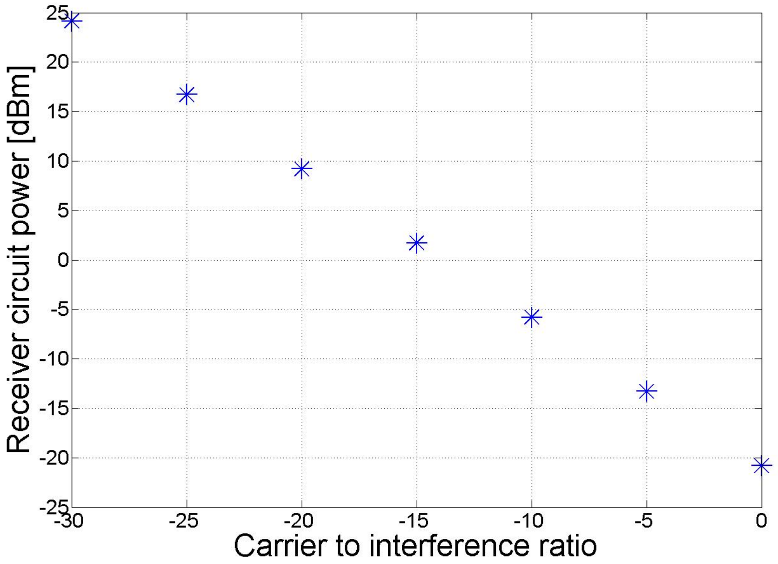

Figure 4.4: *Optimal receiver circuit power to be allocated to the receiver for maximum data transfer energy efficiency (bits/Joule) for different values of adjacent channel interference, for a WLAN-like system in 90 nm CMOS with SNR = 30dB, G = 65 dB.*

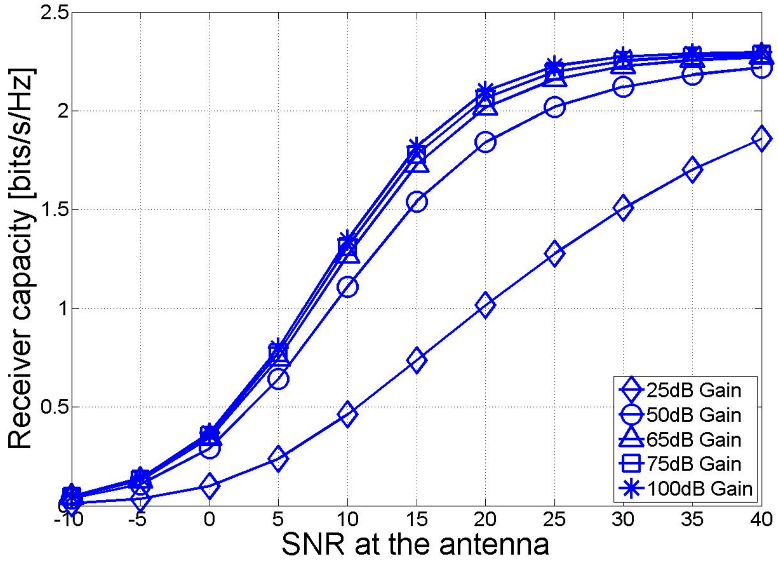

Figure 4.5: *Throughput (bit/s/Hz) at the maximum data transfer energy efficiency (bits/Joule) as a function of SNR at various values of the power gain, for a WLAN-like system in 90 nm CMOS.*

$IP3_{tot} = -20$ dBm. We consider a transmitter that can provide ample S/N_{th}, namely of 30 dB. Adjacent channel interference is at + 20 dB, i.e., CIR = −20 dB. We use the EFOM of Table 4.4 for 90 nm CMOS. Further, $T = 295$ K, $G_{tot} = 65$ dB. The characteristic frequencies f_m are chosen to satisfy the frequency requirements of an IEEE802.11b system in the 2.4 GHz band, with $B = 22$ MHz, f_m is for the LNA $f_1 = 100$ MHz, the mixer $f_2 = 2500$ MHz, and the output buffer $f_3 = 22$ MHz. The MPCO gives the power needed to operate this receiver. The result is very illustrative: The data transfer energy efficiency for a system operating at $IP3_{tot} = -40$ dBm is 4.4 Gbit/Joule ($T = 1.1$ bits/s/Hz, $P_r = 8$ dBm), and at $IP3_{tot} = -20$ dBm it is 0.3 Gbit/Joule ($T = 9.2$ bits/s/Hz, $P_r = 28$ dBm). This motivated our search for a MTCO which results in the optimal setting for NF_{tot} and $IP3_{tot}$ in terms of maximizing the data transfer energy efficiency.

The closed-form solution for optimum spectral efficiency of the throughput as a function of available receiver circuit power and for various values of CIR is depicted in figure 4.2, using (4.3), (4.4), (4.26) and (4.27). For large available receiver power the throughput approaches the throughput for a signal 30 dB above thermal noise, and for an LNA with noise figure $F_1 = 1.7$ dB. At small available receiver power, N_r and N_d become dominant. The figure shows that when the CIR is decreased, more power is needed to achieve a certain throughput. The closed-form solution for maximizing throughput can be extended to express the data transfer energy efficiency in bits per Joule as a function of available receiver power BT/P_r, using (4.2), (4.3), (4.4), (4.26) and (4.27). The result is depicted in Figure 4.3. When the CIR is decreased, the efficiency in bits per Joule for a given available receiver power is decreased as well. The receiver circuit power and throughput corresponding to the optimum of the data transfer energy efficiency curves in Figure 4.3 are plotted in Figure 4.4 and 4.5 respectively.

4.4 Conclusions

A closed form analytical solution has been presented which maximizes the data transfer energy efficiency. From the maximized data transfer energy efficiency all other receiver system specifications such as $IP3$ and F can be derived via the MTCO. Making the $IP3$ adaptive can substantially improve the power efficiency, since a 20 dB reduction in CIR requirements results in a 30 dB reduction in receiver circuit power consumption. Furthermore, the closed form solution allows us to formalize the relation between interference power and achievable throughput for a given available receiver circuit power budget. The relation between interference and receiver circuit power has been known, but we have formalized this relation. For large SNR the throughput corresponding to the optimal data transfer energy efficiency is 2.3 bits/s/Hz, irrespective of interference power level. Interestingly this limit is independent of the used IC technology. However, the optimum power efficiency for lower SNR values does depend on IC technology. This result has interesting consequences for new standards and can aid in the design of new standards and wireless networks to extend battery lifetime, since in typical applications most energy in mobile devices is consumed by the receiver chain. Therefore, a duty cycling strategy at low power consumption levels results in a higher system data transfer energy efficiency. Interestingly, our analysis can be used as a method to determine whether duty cycling is a good design strategy for low power fixed receivers in a given technology.

Chapter 5

ACMM MIMO IC for Analog Spatial Filtering

5.1 Introduction

The main contribution of this chapter is to report our successful design and implementation of a novel 65nm CMOS 4x4 RF Analog Complex Matrix Multiplier (ACMM) IC working at 2.4 GHz. This includes the design method, design choices, the IC implementation challenges, and the attainable circuit performance and its limitations. The IC is designed for MIMO systems operating in the IEEE 802.11n standard. However, the principles are applicable to other frequencies and channel bands. In Chapter 6 we apply the principles to cognitive radio. The theory supporting this chapter has been published in the signal processing and communication theory community in [16] [18] and will be introduced and extended in Chapter 6. This chapter focuses on the novel receiver architecture and its CMOS implementation. As this dissertation may be read by researchers with a different background we give an intuitive explanation of the underlying signal processing principles, to make this chapter self contained, and to explain design choices. The architecture is described in Section 5.3. Our measurements reported in Section 5.5 are used in Section 5.7 to quantify that the average receiver circuit power can

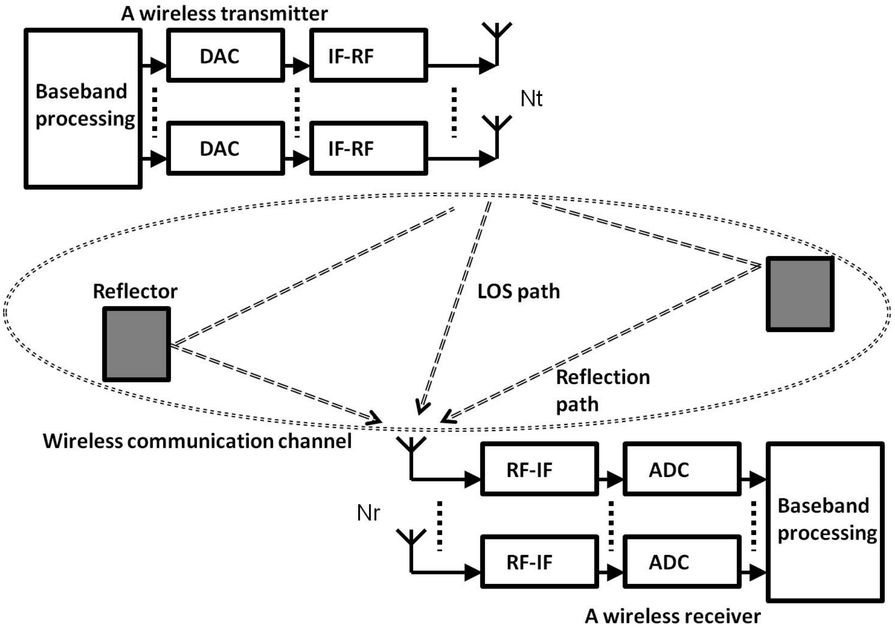

Typical power consumption breakdown in mW

Wireless transmitter

Trend	BB	DAC	RF
State of the art	300	300	500
In 5 years	30	100	400

Wireless receiver

	Trend	RF	ADC	BB
	State of the art	300	300	300
	In 5 years	100	100	30
MIMO system including an ACMM block	In 5 years	10	10	30

Figure 5.1: MIMO system, abstract channel model, and very global indication of MIMO Power consumption breakdown. The power consumption breakdown includes an estimated power consumption in 5 years time of a MIMO system including an ACMM block in the receiver chain.

be reduced by 90%. Our realization confirms theoretical expectations reported in [16] [18] [70]. Section 5.8 concludes this chapter.

As mentioned in Chapters 1, 2, and 3, due to an increasing use of wireless communication systems, the cellular and license free spectrum becomes increasingly congested. Therefore, interference suppression has become of key importance. It is clear that interference can effectively be filtered in time domain, in code domain, in frequency domain, in spatial domain, or by combinations thereof. Unfortunately, the effectiveness of filter selectivity in the analog domain is limited, and increases power consumption. Many receivers such as in laptops and in mobile phones are portable and limited in battery power. Thus average energy consumption reduction to increase battery lifetime is of key importance. Currently, in most systems the radio frequency (RF) front end and analog-to-digital converter (ADC) need to handle the interfering users via extra dynamic range (DR) and bandwidth, before final digital filtering can be performed. The additional DR and bandwidth requirements of the front end, and the additional DR as well as the additional sample rate requirements of the ADC, cause increased power consumption. The DR and sample rate of the ADC depend on the interference power level, both in and out of band. Determining this DR and sample rate requires a trade off with the analog filter selectivity [10] [11].

As mentioned in Section 3.3, multiple-input and multiple-output (MIMO) systems can best exploit their transmit and receive antennas, when they operate in propagation conditions with multiple reflective paths and/or at short distances (Figure 1.1, 1.2 and 5.1). This makes the channel selective both in the frequency and in the angular domain. Modern MIMO systems exploit the angular selectivity by spatially multiplexing multiple streams from a single user. An intuitive interpretation is that of transmitting independent data streams, each via a separate mutually overlapping set of reflective surfaces. Mostly, MIMO systems emit a different data stream on each available transmit antenna, which creates partly overlapping radiation patterns. The scattering properties of the channel typically create random, partly overlapping, but nonetheless separable directionality patterns for the different streams. As Figure 3.2 depicts, a form of spatial multiplexing occurs, which significantly increases the channel capacity. The more orthogonal the various streams are upon arrival at the receiver, the more effective decorrelation can be performed, so the higher the MIMO throughput. Figure 3.2b illustrates that after separation, the capacity per stream may differ, and depends on the actual propagation channel, more precisely on the Eigenvalues of the MIMO channel matrix.

The overall trend of the power consumed by MIMO transceivers using the IEEE 802.11n standard is introduced in Chapter 2. The ballpark figures of Section 2.6 are depicted in this chapter in Figure 5.1. As mentioned in Section 2.6, the instantaneous power consumption of the transmit RF, in particular the PA appears to dominate the power consumption. It is not expected that for the IEEE 802.11n standard, the PA can be designed in the future with significantly lower power consumption. However, typical data traffic patterns requires the transceiver to spent significantly more time listening to the channel and receiving data [12] [13] than transmitting. The cumulative energy consumed by the receiver is typically three orders of magnitude larger than the energy consumed for transmitting data, even though the power consumed by an active PA in the transmitter is larger. To increase battery lifetime via a reduction in energy consumption, our focus is on reducing the time-average power consumption of the receiver. As depicted by the ballpark trend in Figure 5.1 the power consumption reduction over time of the ADCs and the RF front end designs is slower than that of the digital circuitry, which follows Moore's law [37] [49]. Without disruptive new technologies we expect this trend to continue for the foreseeable future. As interference levels grow, the specifications of the RF front end and ADC become more stringent for new generations of radios. The increase in specifications causes an increase in the power demands of the RF front end and ADC.

Current MIMO systems execute spatial signal separation in the digital domain. As a downside, digital decorrelation requires a power hungry front end and an ADC per antenna, in the order of the values in Figure 5.1, particularly if interference can be present [10] [11]. To alleviate the DR requirements posed by interferers, we propose a novel architecture that contains a building block to spatially filter out interfering signals, while simultaneously facilitating the separation of the MIMO streams in the digital part of the system. This is in contrast to previous spatial filter architectures that were designed for only a single data stream. Another novel property of our architecture is that the ACMM building block allows the

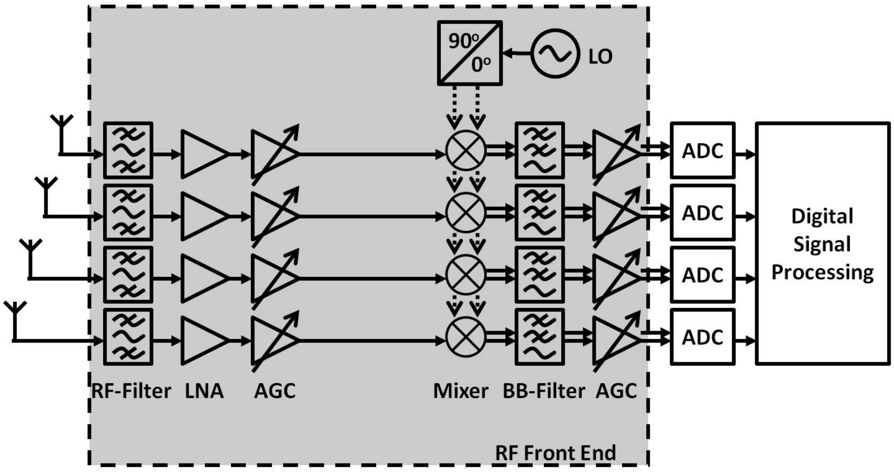

Figure 5.2: Regular MIMO systems consist of separated receivers allowing for multiple spatial streams to transmit data, significantly increasing channel capacity. Every receiver antenna has its own RF front end, making MIMO comparatively power hungry, since capacity scales less than linear in the number of antennas. All spatial multiplexing occurs in the digital domain.

decorrelation of data streams not only in the digital domain, but also preconditions the signals in the analog RF domain, i.e., in front of the ADCs, thereby increasing the effective number of bits in the ADCs and avoiding an increase in noise. In fact, system analyses in [71] showed that a joint analog spatial filter to exploit the angular selectivity of the channel can be very effective across a wide input spectrum even when the coherence bandwidth is small and the number of multi-paths is large. The analog spatial filter is highly effective in most wireless environments, while the channel states for which the spatial filter inadequately separates the desired user from interferers are rare. To our knowledge we present the first IC realization of a 4x4 MIMO architecture which mitigates interference in the analog RF frontend and simultaneously preserves all data streams.

5.2 Proposed MIMO Receiver Architecture

To reduce the number of receiver components and the power consumed by regular multiple antenna systems (a regular MIMO receiver is depicted in Figure 5.2), rank deficient methods such as beamforming have been proposed. Conventional

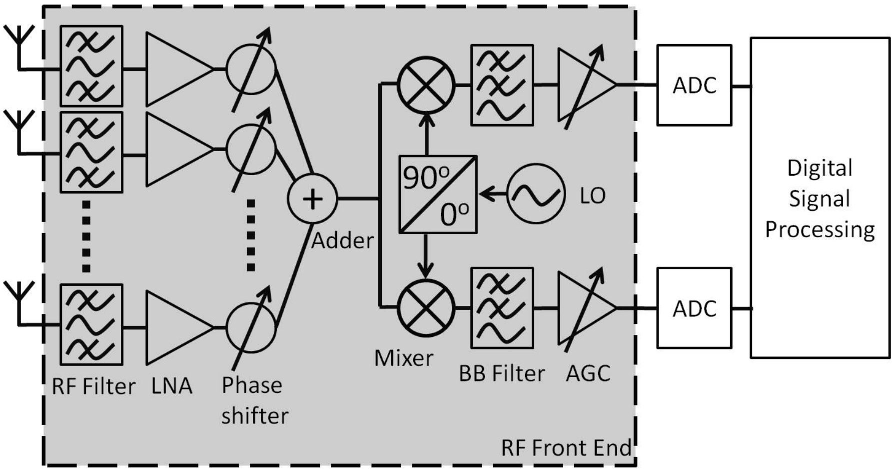

Figure 5.3: A beamformer reduces the number of mixers and ADCs required and allows for spatial filtering to alleviate the dynamic range requirements in an ADC. Since a beamformer is essentially a rank reduction only a single data stream is possible resulting in significant channel capacity loss.

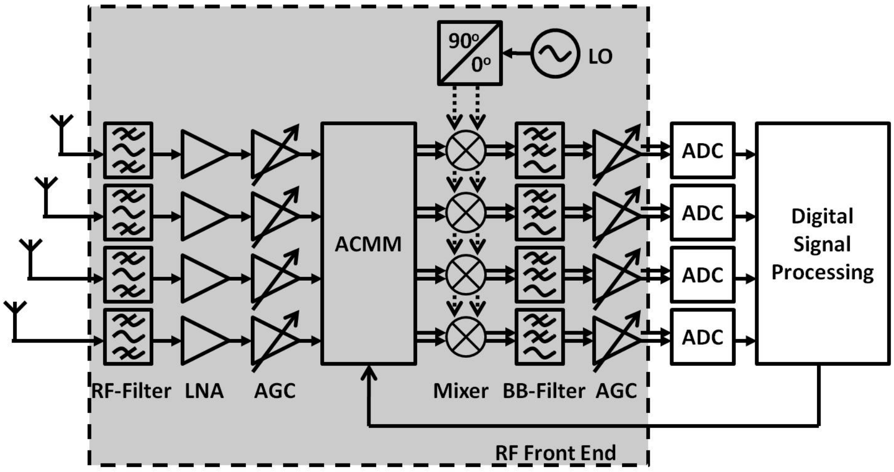

Figure 5.4: Block diagram of ACMM in a MIMO receiver. The ACMM is a full rank matrix operation which allows for multiple independent beamforms simultaneously. Multiple data streams and spatial filtering of interferers are supported simultaneously.

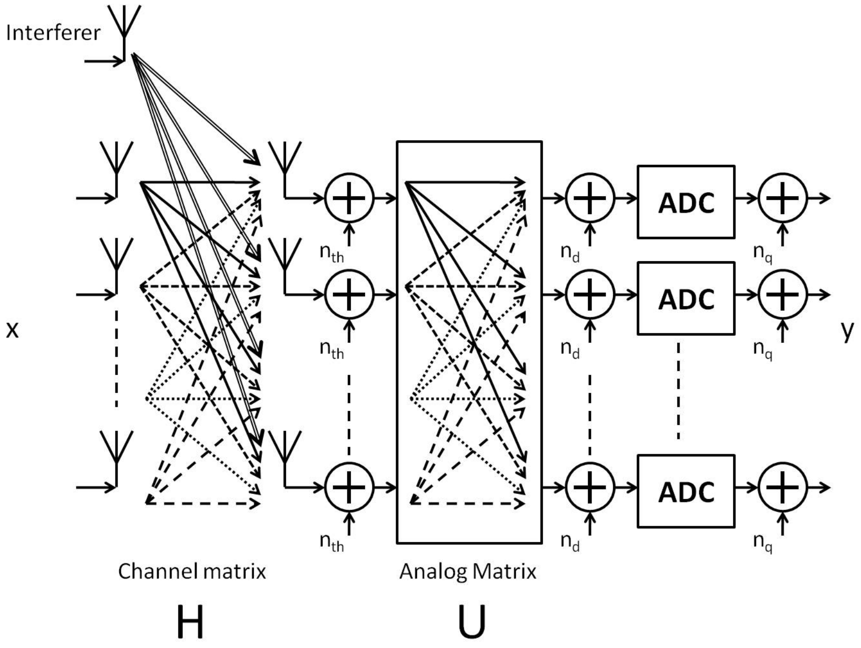

Figure 5.5: Abstract representation of the ACMM architecture.

beamforming methods as in Figure 5.3 are rank deficient, since all antennas share a common ADC. The signals from the various antennas can be combined to optimize the received signal power. If the signals do not arrive from a common angle of incidence, e.g. in a scattering environment, maximum ratio combining gives favorable signal reception. In such a case, the resulting optimized antenna pattern does not necessarily resemble a well defined directional beam. Alternatively, the antenna signals can be combined such that a co-channel interferer is suppressed, which received renewed attention in the context of cognitive radio [70]. Moreover, it was recognized recently [18, 70] that also in the event of interference on neighboring channels an adaptive antenna combiner can reduce the dynamic range requirements of the common ADC significantly. Perfect nulling of a dominant co-channel interferer requires highly accurate phase control in every branch. Yet, reduction of the power of a neighboring channel interferer by a few tens of dBs is feasible with relatively coarse control and nonetheless reduces the power consumption in the front end.

In [72] we propose an RF analog complex-valued matrix multiplier (ACMM) with an equal number of inputs and outputs. The block diagram is in Figure 5.4 and its signal processing model is in Figure 5.5. Instead of reducing the vector signal to a single component, as in regular beamforming, our ACMM has multiple outputs, each of which is offered to the baseband MIMO processor. The RF stages adapt to the current state of the propagation and interference, under adaptive control via a baseband (BB) feedback loop. Since the ACMM reduces the interference power, the analog stages and the ADCs behind the ACMM can be operated at a low power consumption setting, while maintaining a throughput that is comparable to a regular digital MIMO system, i.e., as in Figure 5.2. In this way, our proposed architecture not only alleviates the power-hungry dynamic range requirements of the ADC, but also preconditions the analog wanted signal components to optimally excite the ADCs. This results in significant receiver power reduction, as predicted in [18] [70]. Hence, our architecture performs a non-critical part of the signal separation processing in the analog domain, so that it reduces the total power consumption.

When exploiting the angular selectivity of the channel, every ACMM output can be interpreted as a differently beamformed combination of the inputs. Typically, the digital BB estimation algorithm performs a blind estimation. Similarly, the algorithm used in our measurements is an adaptation of the one used in [18] and performs its channel estimation based on the matrix outputs seen at the ADCs. Since the ACMM restricts itself to phase shifting and amplification, which may have occurred naturally in some scattering propagation environment, the separation algorithms in the digital domain itself only require minor modifications, compared to traditional MIMO without ACMM. However, an additional control loop is needed to adapt the ACMM parameters, and their estimation. The conversion of the digital control into settings of the analog circuits has been part of our design. Due to the oversampling rate of the ADCs and the non ideal selectivity of the analog filter, frequency products containing angular information of the interference are available in the digital domain, and can be used in the digital BB estimation.

For an intuitive understanding of a MIMO receiver in combination with the novel ACMM building block, we can interpret each of the four resulting beam patterns as an appropriate compromise between focusing on a unique Eigenvalue (or unique data stream) in the MIMO channel and suppressing interferers. Effectively, the

ACCM matrix preconditions the antenna inputs such that their range best fits the analog components and ADCs and avoid noise enhancements in later digital stages. Therefore, an optimal matrix setting typically reduces the correlation between the ADC input stream, thereby reducing the commonality of signal components in the various branches. This increases the effective resolution of the ADCs, so it allows further power reduction. The weights of the ACMM are chosen such that the noise contributions of the intermodulation products n_d originating from the adjacent channel interferers, and the quantization noise n_q of the ADCs are reduced. Since the setting of the analog matrix operation occurs in finite steps, and is applied over the entire frequency band, further digital processing is still required to adequately recover the transmitted data. The spatial filtering implemented in our IC is largely frequency independent, except for phase deviations due to parasitic effects in the CMOS implementation. Nonetheless, our experience is that the ACMM can effectively be used to filter adjacent channel interference, particularly when it is caused by a (strong, thus) nearby transmitter: in fact a short range channel typically exhibits a low delay spread thus a high coherence bandwidth. As Figure 5.5 illustrates, the channel matrix including interference paths is no longer square, but rather behaves as a rank-reduced channel matrix. It introduces a blind spot for the combination of phase settings that represent the interference. In the case of co-channel interference, correlation techniques can be applied to estimate the channel, in particular if the desired user and the interferer use CDMA.

Because the matrix can be used to partially decorrelate the antenna inputs, it can also be used to mitigate and alleviate other correlating effects, such as interaction between closely spaced antenna elements.

5.3 ACMM Circuit Description

This section describes the 65nm CMOS ACMM IC, which has been designed to be integrated into in an existing MIMO test bed [73] containing the block functions in Figure 5.4 except the ACMMM. For ease of implementation, the 65nm CMOS

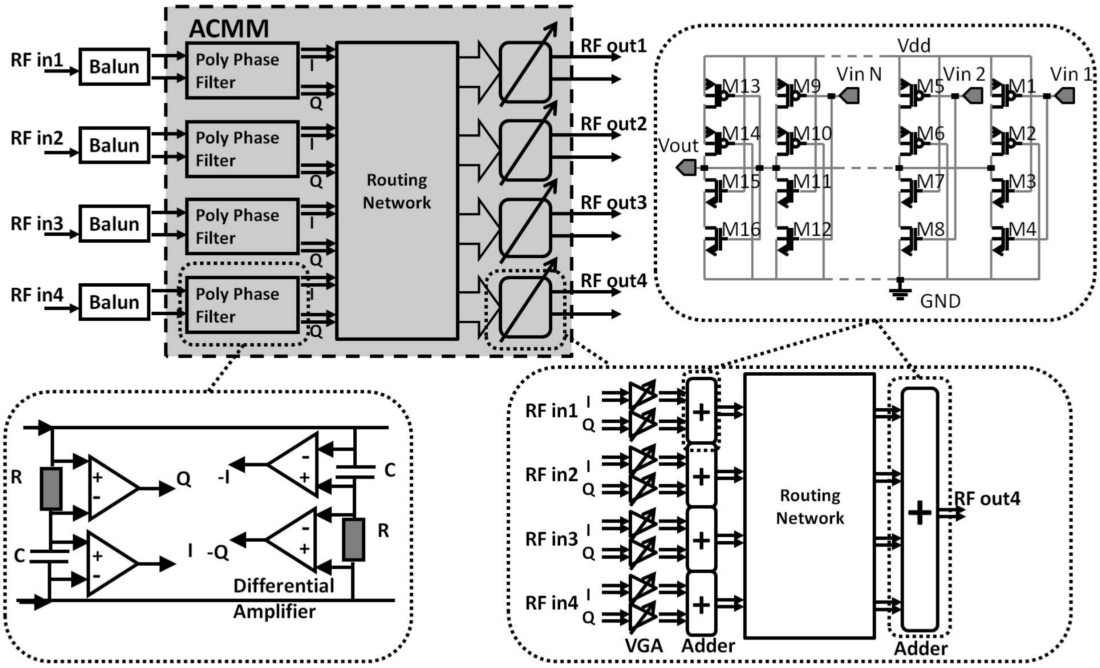

Figure 5.6: Block diagram of ACMM IC board containing ACMM IC and baluns. ACMM IC consists of polyphase filters, routing network, VGAs, and adders.

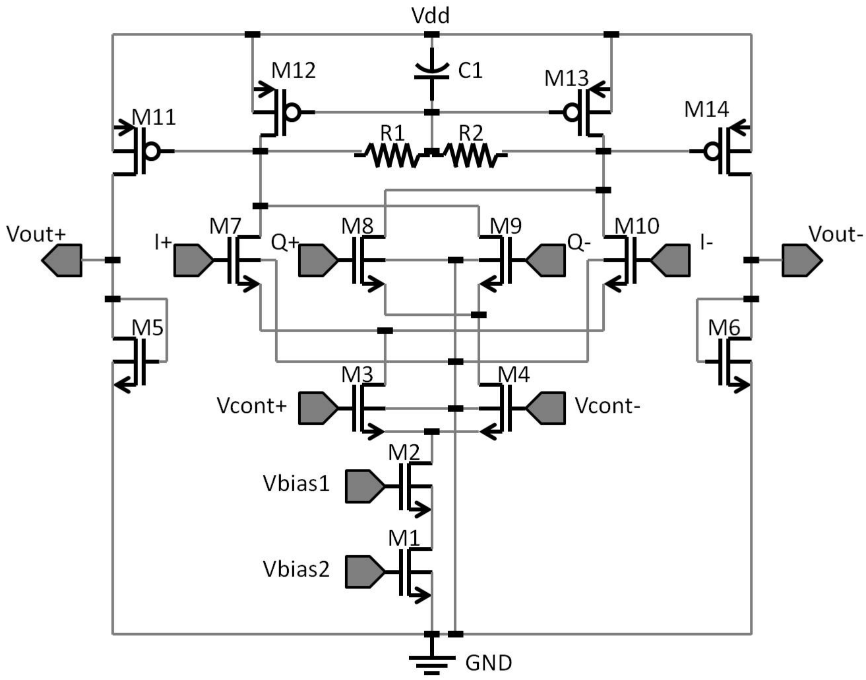

Figure 5.7: VGA is implemented as a Gillbert Cell. RC filter is part of Vdd filter. Cascoded current source for common mode rejection.

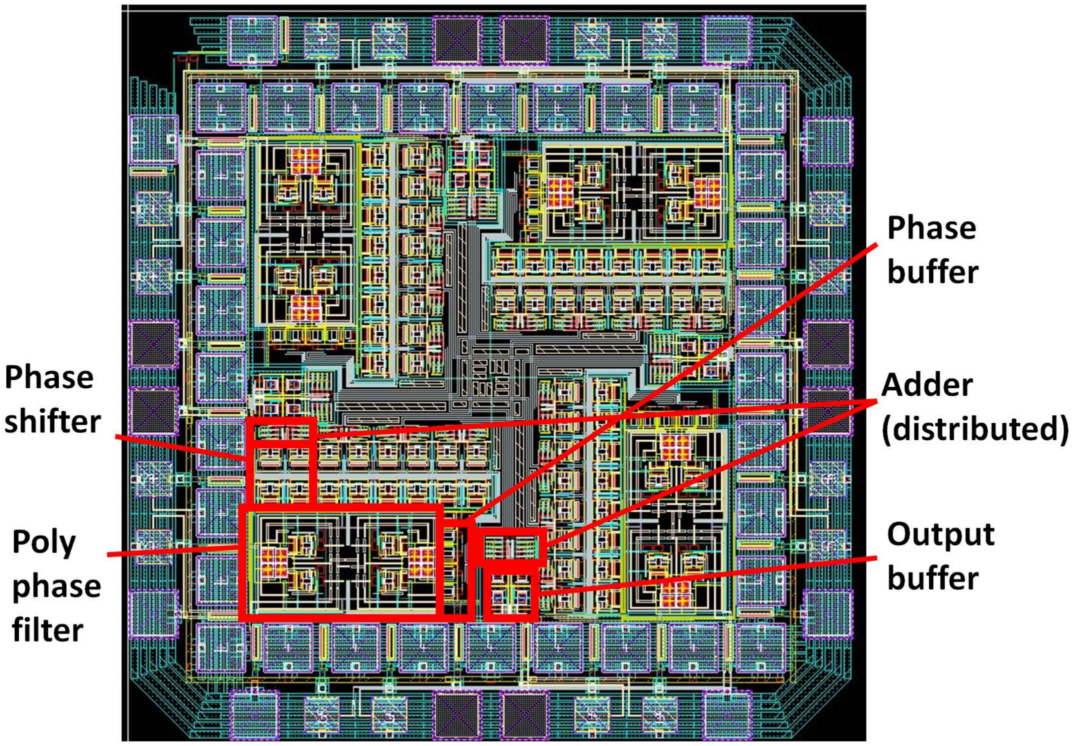

Figure 5.8: Layout of the ACMM IC.

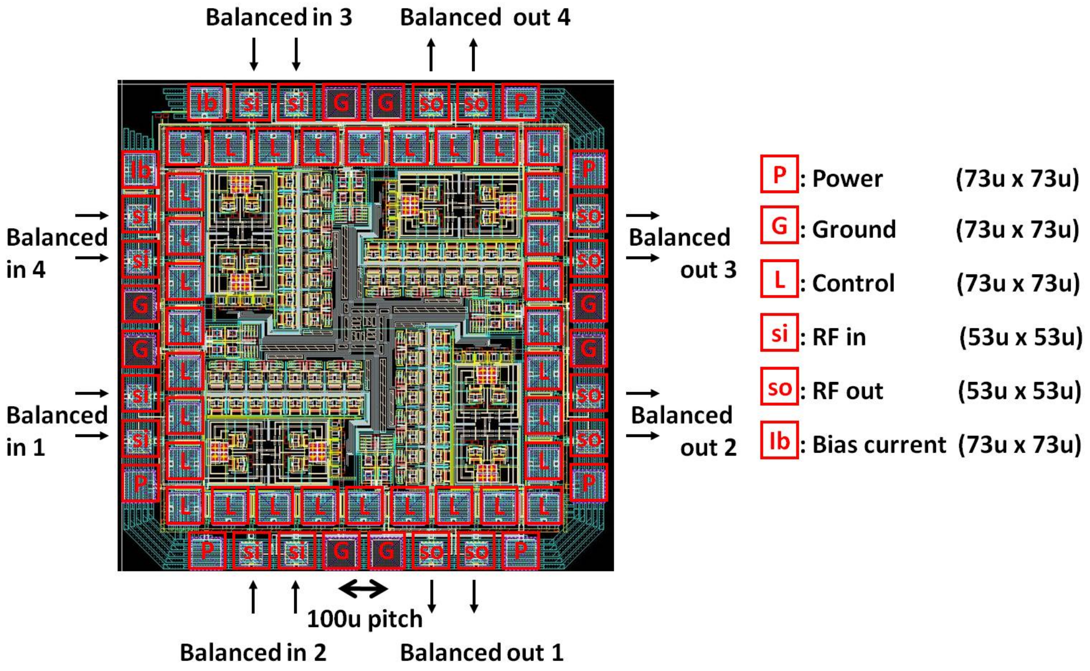

Figure 5.9: Layout of the ACMM IC with bond pad ring layout. The effective area inside the bond pad ring is 720 x 720 um.

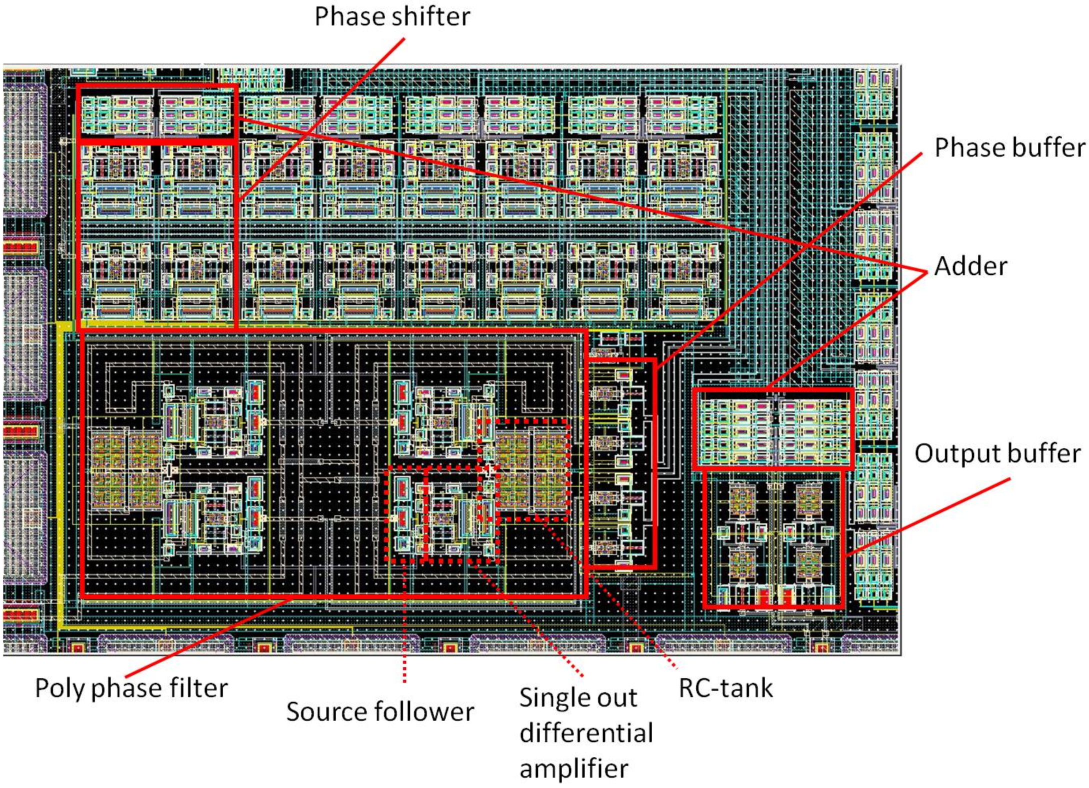

Figure 5.10: Close up of a corner of the layout of the ACMM IC.

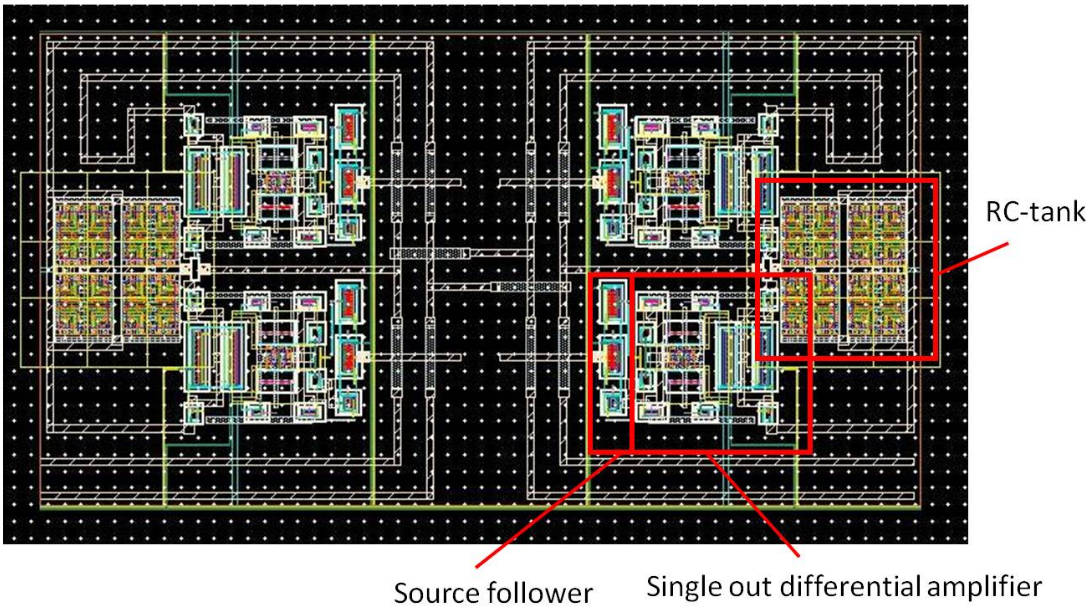

Figure 5.11: Layout of a single PPF stage.

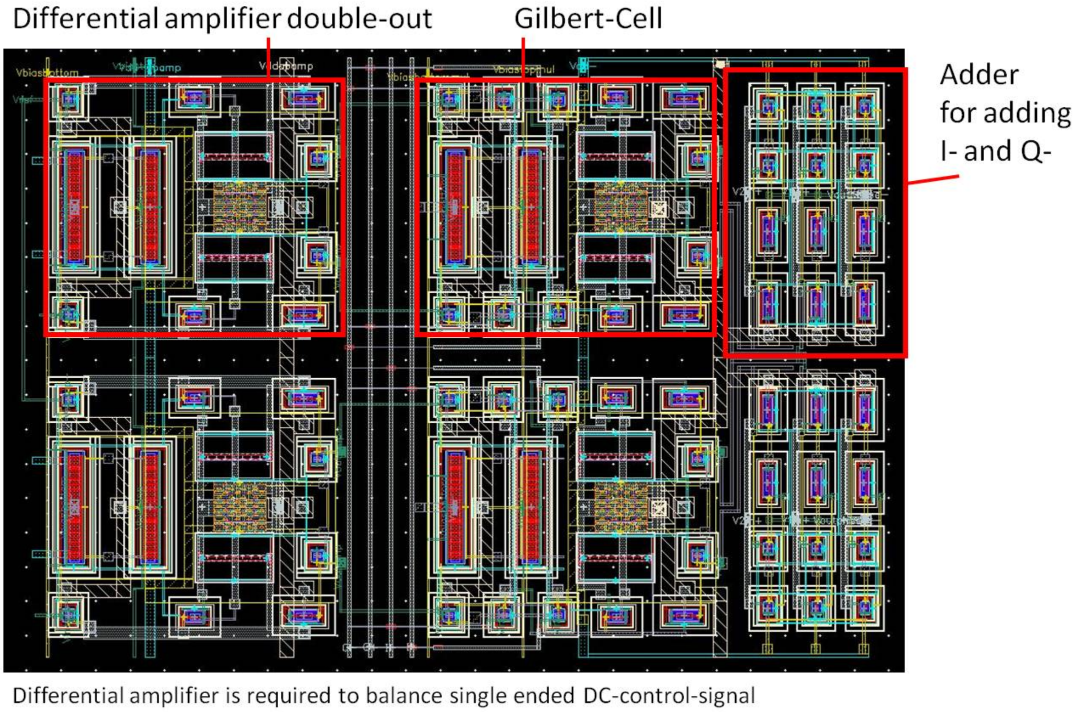

Figure 5.12: Layout of a single phase shifter stage.

ACMM IC has been mounted on a custom-designed PCB board including baluns and decoupling capacitors. The current MIMO test bed comprises off-the-shelf components such as typical RF-filters, LNAs, RF-AGCs, mixers, BB filters, ADCs and DSP, as has been discussed in [73]. The matrix elements of the 65nm CMOS ACMM IC building block consist of I and Q weights each of which is individually controlled through an analog signal. The analog control signals will eventually be generated in the test bed via DACs with finite step size. It is important to point out that, since the circuit was intended to operate in a test bed to be used for proof-of-concept measurements, the design is optimized for spatial resolution. We purposely over designed the spatial resolution for testing. One of the goals is to lower the DAC resolution for the analog control signals and measure the effect on overal system performance. Since the circuit is stand alone in and output buffers were added which are not necessary in a fully integrated design. These buffers are required to generate enough gain to drive the ADC buffers in the test bed, but not for the spatial filtering itself.

Figure 5.6 depicts the block diagram of the ACMM IC and PCB board. The 4 single-ended RF inputs are balanced off chip by baluns. For better isolation, the ACMM IC has been implemented differentially. Each RF input of the ACMM is divided into a differential I and differential Q pair by a polyphase filter (PPF). Every RF I and every RF Q output pair of the PPF is split in 4 balanced signals and routed to the 4 separate beam formers (BFs). Each BF consists of a differential VGA for every I and for every Q RF input pair, and an adder. The values of the elements in the matrix are created by an adaptive complex amplification (I and Q) using VGAs. There are a total of 32 VGAs, which corresponds to the total number of real and complex weights in the 4x4 matrix. The outputs of the VGAs are combined by adding currents (Figure 5.6). The VGAs are implemented as Gilbert cells (Figure 5.7). The current sources are cascoded for better common mode rejection. The adders are distributed over the IC to minimize the amount of wires that require routing (Figure 5.8, 5.10, and 5.12). The single ended analog DC control input signals are balanced on chip via differential amplifiers to reduce the number of required analog control signals and thereby the number of bond pads (Figure 5.9). The balancing of control signals would not be required when the ACMM is integrated with the rest of the transceiver.

The PPFs create the differential RF I and differential RF Q pairs via two RC filters. Each antenna receives a wide band RF signal. Therefore, a mismatch in the group delay between individual PPFs can have a huge impact on the overall control accuracy across this wide frequency band. To minimize the mismatch between individual PPFs we opted for a very accurate matching of the group delay between I-, I+, Q-, and Q+, inside a single PPF over the entire frequency band of interest, 2.4 GHz to 2.5 GHz. A mismatch in the absolute value of the phase for a single frequency or for the entire frequency range can be compensated by applying a different amplification on the I and Q paths. This is analogous to classical I and Q mismatch compensation, but this does not compensate the group delay mismatch between I- and I+ and between Q- and Q+. Furthermore, due to the group delay mismatch between Q and I, I and Q compensation via different I VGA and Q VGA weights is only valid for a limited frequency range. Thus, a relative mismatch between the I and Q phase across the wide frequency range cannot be completely compensated as such. To achieve a good matching of the group delay between the four outputs of an individual PPF, we minimized the parasitic capacitors affecting the two RC filters. Ideally all current that flows through the R also flows trough the C at a 90 degrees phase rotation. In reality, parasitics cause current to leak and thereby alter the ideal 90 degrees phase rotation. This effect is frequency dependent and dominated by the parasitic capacitors at the inputs of the differential amplifiers of the PPF. The size of the parasitics in the IC can vary across the inputs, due to process spread. To minimize the phase rotation and the effect of process spread caused by the parasitic capacitors, we gave the gate of the input transistor of the differential amplifiers the smallest available gate length in C65, and we minimized the connection wire lengths in between the R, C, and comparators. Any effect of proces spread on the amplification of the differential amplifiers is calibrated by applying different VGA voltage settings in the matrix. To best ensure an equal amount of parasitics on the various differential amplifier inputs and also to minimize wire length differences which cause phase imbalance between the positive and negative RF inputs of the differential amplifiers inside a single PPF, a star structure was chosen for the differential input wires. Due to these symmetry and parasitic requirements, the PPF occupies a relatively large area in the layout (Figure 5.8, 5.10, 5.11, 5.12, and 5.18). The penalty for such a high matching between the group delays is an increased overall noise figure of the ACMM. This increased noise figure is caused by the mismatch between the RC filter (matched to the 50 Ohm impedance of the input connections) and the input impedance of the differential amplifiers (input impedance in the order of 10k Ohm). To minimize other mismatches due to differences in parasitics and wire lengths inside the ACMM, the internal layout of the IC is symmetric for every individual PPF output to every individual phase shifter input. Further, the ACMM is rotational symmetric between the outputs of separate phase shifters to the input of the adders and in between the distributed adders in order to maintain symmetry between the internal routing. In summary, there are two mechanisms important for the accuracy of the matrix. Firstly, there are frequency independent differences between RF signals across the band of interest due to parasitic, mismatch, and wire length differences. Secondly, there are frequency dependent differences between RF signals across the band of interest due to parasitic, mismatch, and wire length differences. Due to the structure of the matrix, the blind BB algorithm compensates for the frequency independent differences, leaving the frequency dependent differences as the dominant source of inaccuracy in the system.

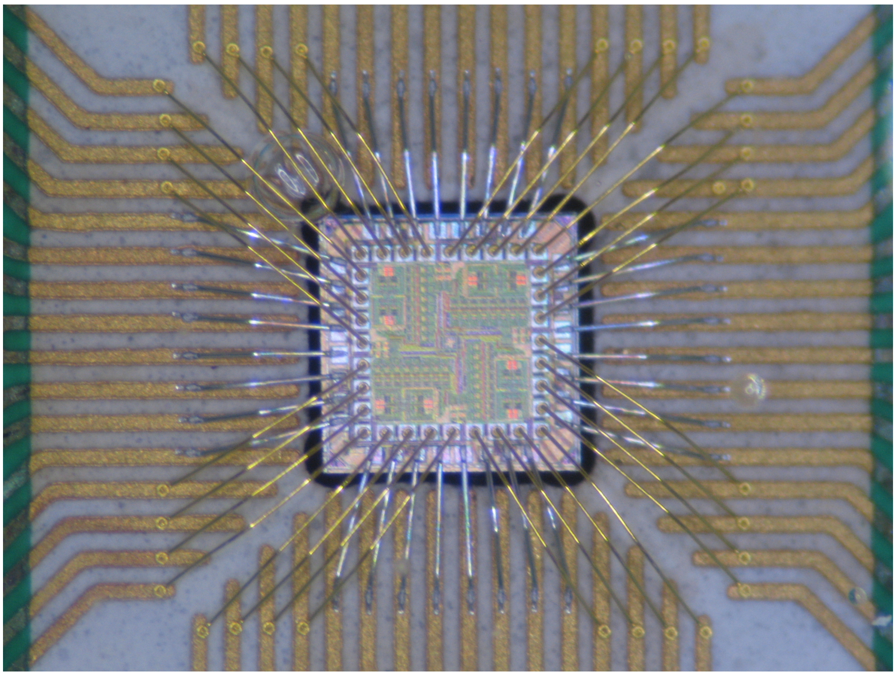

Figure 5.13: *Top view of the bond wires of the IC. The short aluminum wires are connected to the outer pad ring containing the RF signals. The longer gold wires are connected to the inner pad ring containing the control signal pads.*

5.4 Aluminum and Gold Bond Wires

The ACMM IC has a total of 64 bond pads. To reduce the die area of the IC the bond pads are divided over two staggered bond pad rings. The outer ring contains the RF signal pads and the power supply pads and the inner ring contains the control signal pads (Figure 5.9). To minimize the bond wire parasitics the bond wires should be as short as possible. To shorten the length of the bond wires the IC is lowered in a cavity in the PCB (Figures 5.14 and 5.15). The IC is lowered into an adhesive in the cavity until the top of the IC is nearly level to the top of the PCB. To prevent the bond wires of the inner and outer ring from touching, we opted for a different bond wire technology for the inner and outer bond pad ring, namely gold wires and aluminum wires respectively. The benefit of aluminum bond wires for the outer ring is that they leave the IC and enter the PCB with a nearly parallel orientation, while the gold wires of the inner ring leave the pads and enter the PCB with a nearly perpendicular orientation (Figure 5.15). This difference in orientation limits the chance that one of the inner and outer bond

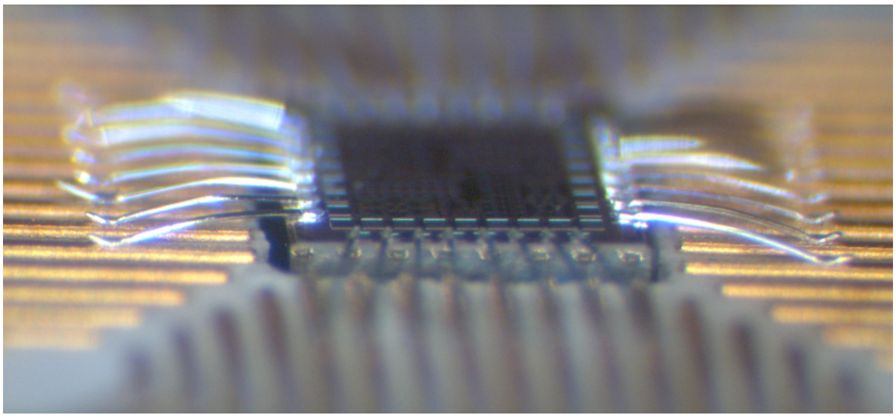

Figure 5.14: *Side view of only the aluminum bond wires of the IC. The IC is lowered in a cavity to shorten bond wire length. The short aluminum wires are connected to the outer pad ring containing the RF signals.*

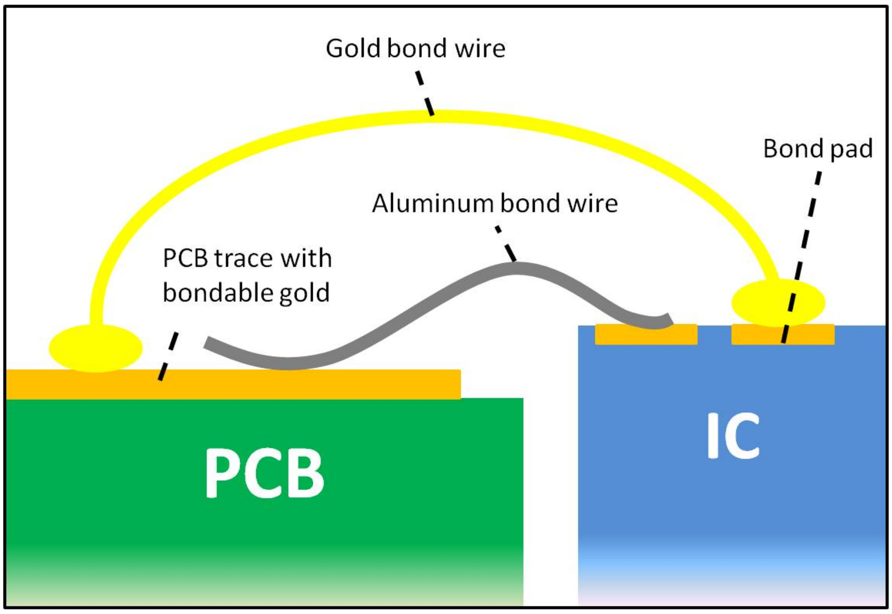

Figure 5.15: *Schematic side view of the bond wires. The IC is lowered in a cavity to shorten bond wire length. The short aluminum wires are connected to the outer pad ring containing the RF signals. The longer gold wires are connected to the inner pad ring containing the control signal pads.*

wires touch each other. Due to the small pitch of the bond pads and the limits of the aluminum bond wire machine, the aluminum bond wires are attached inversely to the standard procedure. The benefit of wiring the aluminum bonds inversely is that the excess tab of the aluminum wires is at the side of the PCB (Figure 5.14). Since the bond wires are fanning out, having the tab of the aluminum wires at the IC side could have caused the tabs of separate wires to touch each other. By lowering the IC into the cavity and by using aluminum bonds which leave and enter parallel to the IC and PCB, the RF bond wire lengths are reduced from 3 mm to 0.8 mm.

5.5 Measurement Results

The spatial resolution and nulling precision is limited by the accuracy with which the phase shifts and amplitudes of the matrix elements can be controlled. In our system, the accuracy of the phase and amplitude setting is further determined by deviations from a true-time delay for different matrix elements, so these are susceptible to slope deviations in the group delay. The parasitics, mismatch, and wire length differences inside the PPF cause a slight imbalance in the group delay of I- and I+, and Q- and Q+. This causes an error in the differences of the phase shift over the band of different matrix elements which are added at every output. The left hand side of Figure 5.16 depicts a screenshot of a typical S-parameter measurement of a single setting for a single matrix element. As can be seen the input matching, indicated by S11, of the IC and PCB board is -23 dB in the band of interest. In the measurement the scale of the y-axes is 20 dB per unit. The S11 measurement shows that, as was expected, the input matching of the RC filter is poor at low frequencies, where the C acts as an open, while at higher frequencies we can see the effect of the R. Further, the measured S22 output matching is -16 dB in the band of interest, the S12 is -80 dB, and the S21 is used to measure the phase over the band of interest.

The measured maximum difference in the expected value of the phase, originating from deviations in the group delays, in a PPF determines the resolution with which

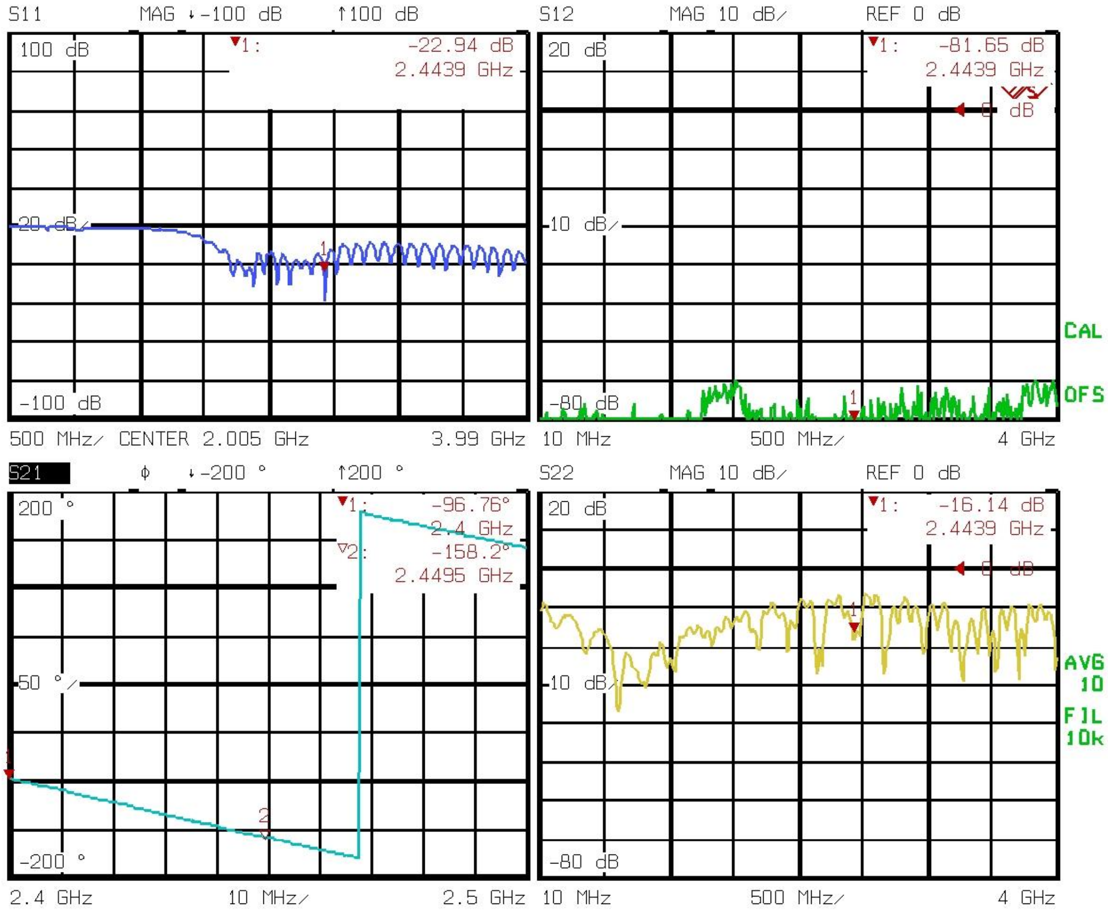

Figure 5.16: Screenshot of the measured accuracy via S parameters of a single setting for a single complex weight in the 4x4 ACMM as a function of frequency. Different matrix element settings have different group delays limiting the matrix element accuracy.

Table 5.1: *Typical measurements of the maximum relative differences in phase caused by the group delay differences referred to the group delay setting "21 I+", from 2.4 GHz to 2.5 GHz, for different settings of matrix element "21" which is used to control the amplification and phase shift between RF input 1 and RF output 2.*

Matrix element setting	**Group delay phase change $\Delta(\Delta\phi)[^{\circ}]$ 2.4 GHz - 2.5 GHz (Referred to setting 21 I+)**
21 I+	0
21 I-	2
21 Q+	1
21 Q-	2
21 I+ Q+	0
21 I- Q-	0
21 I+ Q-	2
21 I- Q+	2

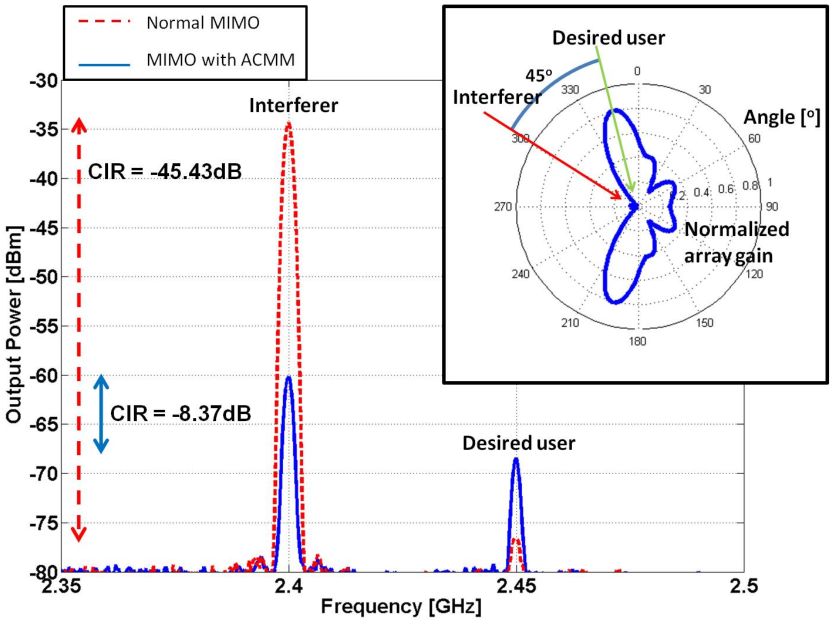

Figure 5.17: Measured CIR improvement, desired user on 2.45 GHz and a much larger interferer at 2.4 GHz. Inset: Visualization of normalized linear array gain for single output of receiver using ACMM.

Table 5.2: *Measurements and potential power reduction with current ACMM design.*

Parameter PCBs and IC	**Value**	**Remarks**
Vdd	1.4V	Designed 1.2V
Total Idd	97mA	Including output buffers
P ACMM core	12mW	Without output buffers: simulated
Gain$_{max}$	12dB @1.4V	Including LNA and PCB losses. Designed 20dB @ 1.2V
NF$_{total}$	14dB @1.4V	Including LNA and PCB losses. Designed 14dB @ 1.2V
Sensitivity	-60dBm	Designed -60dBm
Accuracy @ 20MHz	8 bits	
RF input range	+26dBm -60dBm	
RF output range	-19dBm -48dBm	Compressed range

Reference	**Current Average Rx Power Consumption (4x4 MIMO)**	**Estimated Average Rx Power Consumption with 4x4 ACMM**	**Power saving**
[32]	1488mW Including ADCs	57mW (Including ADCs)	96%
[33]	256mW Only RF	25mW Only RF	90%

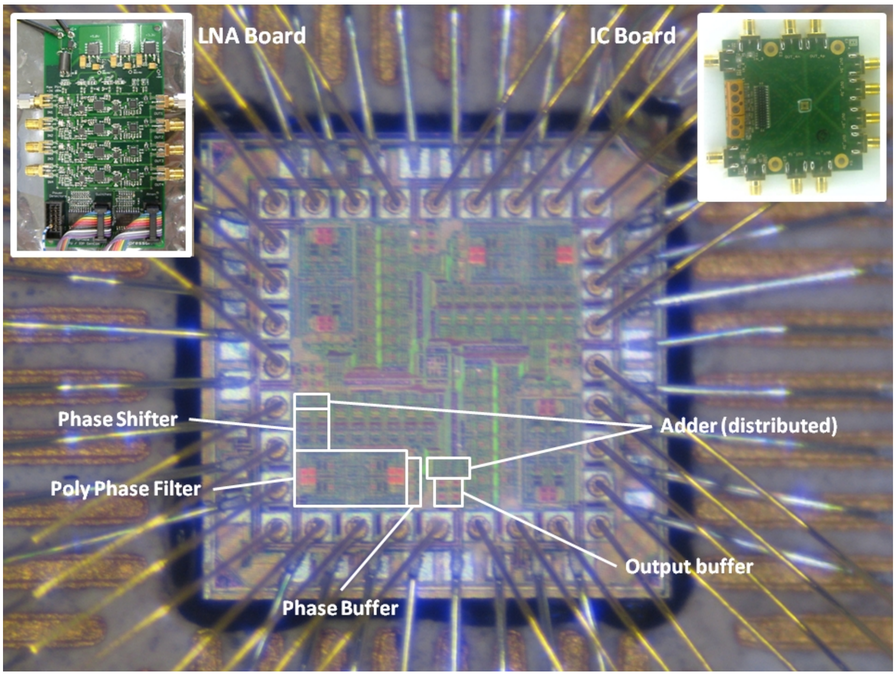

Figure 5.18: IC Die close up and PCB boards.

the matrix can eliminate or reduce interference. An absolute error in the phase can be calibrated by varying the amplification of the I VGA relative to the Q VGA of a matrix element. To find the maximum relative phase error, we have measured every matrix element separately for different I VGA and different Q VGA settings. Table 5.1 depicts a typical result, and correspond to the matrix element 21 which is used to control the amplification and phase shift between RF input 1 and RF output 2. Results are shown for 8 uniformly distributed element settings by controlling both the I VGA and Q VGA to either an off state equal to half the Vdd, or to a positive or negative on state setting defined by half the Vdd plus or minus 200 mV, respectively. We measured from 2.4 GHz to 2.5 GHz and over 360^o and measured a maximum relative inaccuracy of 2^o caused by the differences in group delay compared to the baseline group delay of 21I+ (the I VGA of matrix element 21 is set to Vdd plus 200 mV and the Q VGA is switched off). The measurement was repeated for all matrix elements and yielded a comparable result. At the outputs of the 4 adders, this corresponds to an equivalent overall effective beam forming accuracy of each of the 4 beam formers of approximately 8 bits I and 8 bits Q for a 20 MHz band, and 5 bits I and 5 bits Q for a 100 MHz band. This reduces the accuracy requirements of the DACs used to control the

VGAs. In fact, controlling the VGAs at higher resolution would not significantly improve the accuracy of the resulting beam formed outputs.

Figure 5.17 depicts a system level IC measurement. The desired user is at 2.45 GHz, while a 45 dB stronger interferer is at 2.4 GHz. The dotted line represents the signal present in a normal MIMO receiver branch. The solid line depicts the signal in the same receiver branch after signal preconditioning via our spatial filter. In this measurement, the delays for the desired and interfering antenna signals are created via fixed delay lines from a single source for each of the signals. The element values of the ACMM are calculated according to [18]. The corresponding angle-of-arrival (AOA) difference between the two sources is 45°. For this AOA difference the channel-to-interference ratio (CIR) improvement is 37 dB. This 37 dB improvement is in agreement with the 5 bits accuracy over the 100 MHz band measured in Table 5.1. Due to the different cable lengths the corresponding phase differences of the measurements do not correspond to the phase shifts that would occur in a linear array with antennas at half a wavelength of the carrier frequency when receiving these signals in a multi-path-free environment. In the radiation pattern of the inset of Figure 5.17 we have corrected for this nonuniform phase distribution by assuming that the antennas are off grid as compared to a linear array, and calculated the corresponding beam pattern from the measured outputs. This calibration was performed to provide an intuitive and graphical interpretation of the measured ACMM output. The CIR improvement is achieved without using any frequency selective filtering. Spatial filtering can even be applied with an interferer at the same frequency as the desired user.

The measured performance of the LNA and ACMM are specified in Table 5.2. Vdd is 1.4 V and Idd is 97 mA including output buffers. Our realization of the IC fell short of the target gain, but this could be compensated through the LNA board such that we could reassure performance to determine the system power reduction. In principle the gain is required to drive the input buffer of the ADC in the test bed. The gain is not necessary to show the functionality of the spatial filter operation. In a fully integrated design the input buffers of the ADC and the output buffers of the ACMM are not necessary.

5.6 Measurements Analysis and Redesign

Due to errors in the post layout parasitic extraction deck in the TSMC library, proper post layout simulations could not be performed to verify the ACMM layout design. Therefore a manual parasitic extraction was conducted and the expected gain was 10 dB. After tapeout the measured gain of the ACMM was between -20 to -30 dB. By increasing the bias current and power supply voltage, the gain was increased to 2 dB. The origin of the loss of gain at the original biassing and voltage supply was found by Zhe Chen under my supervision via measurements and additional circuit and post layout simulations. After an initial RC parasitic extraction the gain was estimated between -10 to -22 dB, which was still 10 dB higher than the measured value. After inclusion of additional causes for gain loss, such as the double MIM-Capacitor extraction error of the TSMC library, the simulated gain loss after parasitic extraction approached the measured results up to an error of 1 to 4 dB. A main cause of the gain loss was ground lifting due to a connection error in the IC wide ground mesh. Therefore, increasing the Vdd and bias current could restore most of the gain loss.[1]

Isolate PCB and Connection Wires

The IC is measured with a vector network analyzer (VNA) (Rohde & Schwarz, ZVRE) with two single ended cables. The Vdd and several control signals are generated by five power supplies (Agilent E3631A), the other control signals and the bias currents are set with a precision measurement mainframe (Agilent E5270). In measurements the differential outputs of the IC are first DC decoupled with external decoupling capacitors and then connected via SMA cables to an external off-PCB balun. The single ended port 1 of the VNA is connected to one of the single ended inputs of the IC-PCB, and the single ended port 2 of the VNA is connected to the output of the external balun. The effects of the cables connected to the VNA are removed from the measurements via a calibration with a calibration set. To accurately measure the IC performance in combination with the bond

---

[1] In principle we do not need gain for the spatial filter, we needed gain to drive the input buffer of the ADC in the test bed

wires we should account for: the PCB losses, the external decoupling caps, the external balun, and the connection wires between the external decoupling caps and external balun. To measure the PCB losses an IC was removed from one of the six bonded PCBs (specimen 3) and the PCB without IC was measured under a probe station. The measured loss at 2.45 GHz from input SMA connector to output SMA connector is 4 dB. The decoupling capacitor on the output SMA connector has a loss of 0.3dB at 2.45 GHz. The wires used to connect the decoupling caps to the balun have a measured loss of 1.7dB at 2.45 GHz. The measured loss of the balun at 2.45 GHz is 1.5dB. Therefore, the total loss outside the IC that should be accounted for in the IC measurements is 7.5 dB.

Measurement of ESD Diodes

The ESD diodes are checked for damage via DC measurements. In the measurement all ports are connected to ground while one port is connected to a voltage source. Due to the on-PCB baluns it is not possible to measure the input ports. Furthermore, it is not possible to isolate the individual power supply pads. The result of the 5 remaining specimens is shown in Tabular 5.3. As can be seen specimen 1, 4, and 5 suffer from ESD damage. The removed IC of specimen 3 had a short from Vdd to ground.

Parasitic Extraction

In order to find the overall gain loss a proper parasitic extraction needed to be performed. To perform a proper parasitic extraction several issues needed to be resolved:

- Parasitic resistor effect and analysis
- Parasitic capacitor effect and analysis

Table 5.3: *DC Measurement and of ACMM ports.*

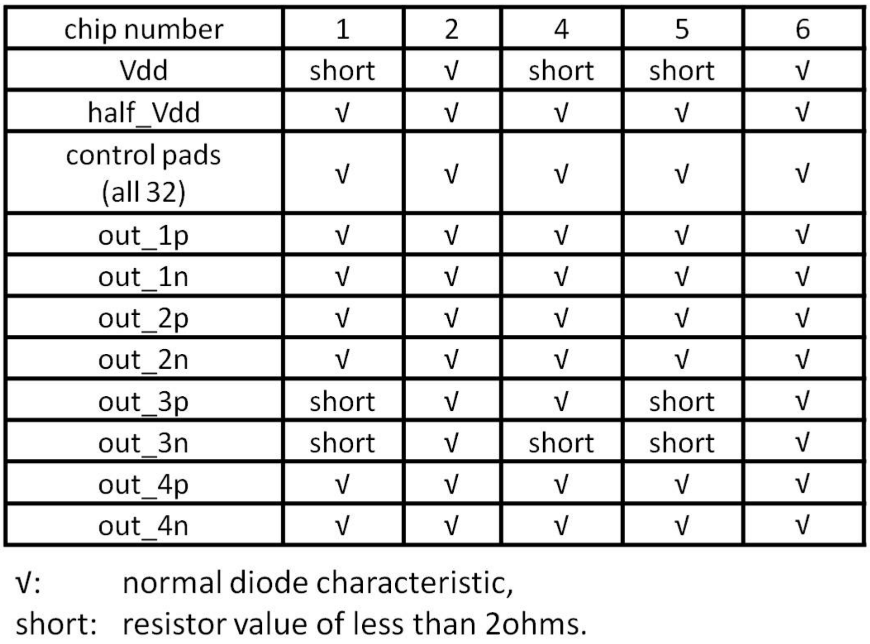

chip number	1	2	4	5	6
Vdd	short	√	short	short	√
half_Vdd	√	√	√	√	√
control pads (all 32)	√	√	√	√	√
out_1p	√	√	√	√	√
out_1n	√	√	√	√	√
out_2p	√	√	√	√	√
out_2n	√	√	√	√	√
out_3p	short	√	√	short	√
out_3n	short	√	short	short	√
out_4p	√	√	√	√	√
out_4n	√	√	√	√	√

√: normal diode characteristic,
short: resistor value of less than 2ohms.

- Twice MIMcap extraction problem

- Temperature effect

- Total gain loss distribution

The measurement of Idd, Vdd and S-parameters did not provide enough information to find out the reason for the gain loss. Therefore, post-layout simulation were used. However, the post-layout simulation results are quite different from measurement results. One of the problems was the Twice MIMcap Extraction. This resulted in an erroneous estimate of the capacitor values. To obtain more reliable results some settings were changed, Assura LVS was used instead of Calibre LVS. Further there was a label problem in parts of the layout. There was only one Vdd and Gnd label in the top level layout. This was changed to 6 Vdd and 8 Gnd corresponding to the pads where the bondwires connect the power supply to the IC. The simulation results after these changes are shown in Figure 5.19. Next to the

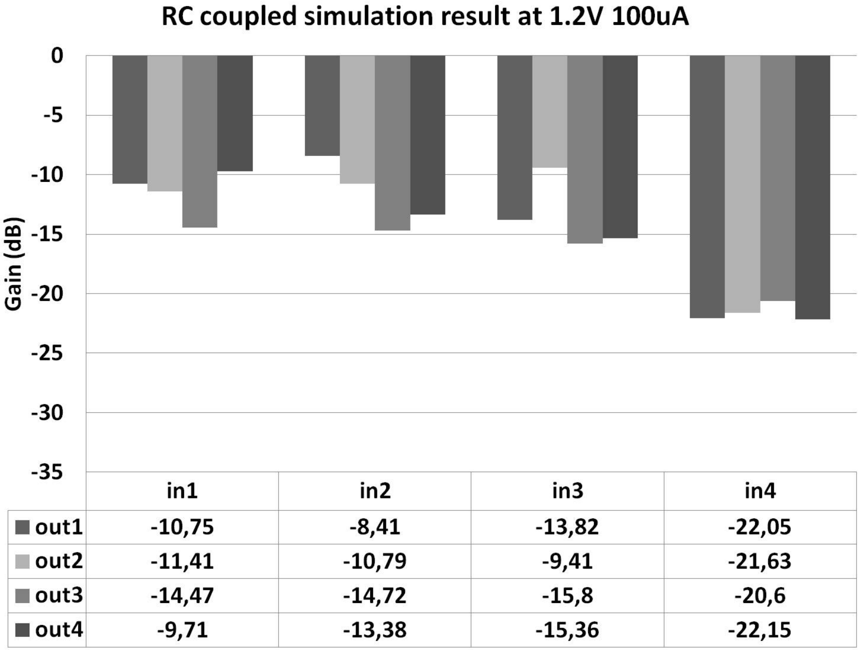

	in1	in2	in3	in4
■ out1	-10,75	-8,41	-13,82	-22,05
■ out2	-11,41	-10,79	-9,41	-21,63
■ out3	-14,47	-14,72	-15,8	-20,6
■ out4	-9,71	-13,38	-15,36	-22,15

Figure 5.19: *RC simulation results.*

simulations, measurements were conducted on the IC. The measurement results are depicted in Figure 5.20. The measurement results and initial RC simulation values are aligned for comparison in Figure 5.21. As can be seen in the figure, the measurement results and simulation results are still approximately 10 dB apart. The expected gain from the schematic alone without parasitics was 22 dB, which is 30 to 45 dB higher than the gain after parasitic extraction.

Ground Lifting

After the RC coupled simulations, simulations were done with only the R parasitics in order to find out if there were DC power supply issues. As can be seen in Figure 5.22, the input part of channel 4 has the worst DC biasing and the output part of channel 3 has the worst DC biasing. The reason is that despite a large IC wide ground mesh there are only 3 connections between the Gnd mesh of the pad ring and inter ground ring so that the Gnd of the VGAs, opamps and buffers are not 0 V but 30-50 mV. This reduces critical voltage headroom. Further, the width of the internal Vdd ring is only 8 um, resulting in a decrease of the Vdd of 40-60 mV

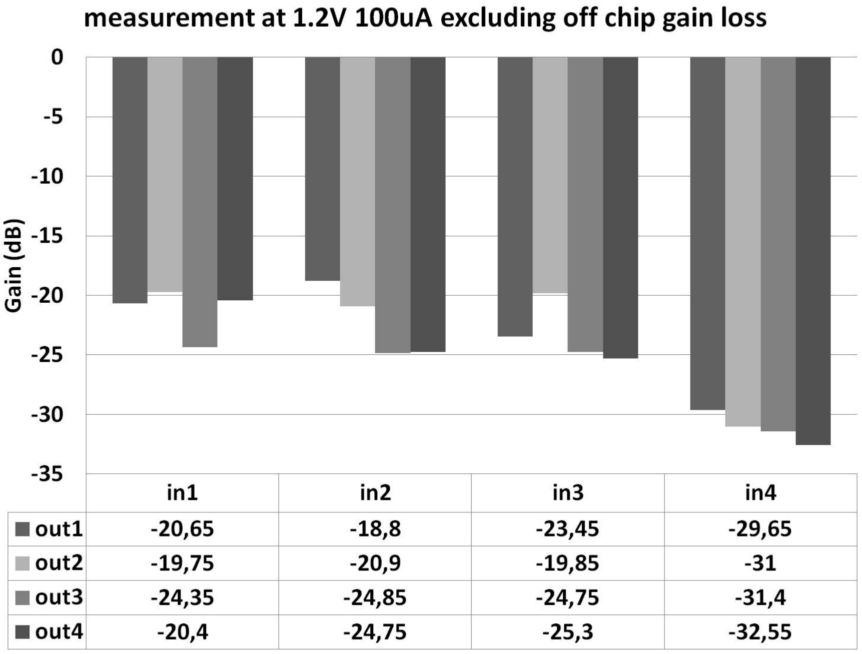

	in1	in2	in3	in4
out1	-20,65	-18,8	-23,45	-29,65
out2	-19,75	-20,9	-19,85	-31
out3	-24,35	-24,85	-24,75	-31,4
out4	-20,4	-24,75	-25,3	-32,55

Figure 5.20: *Measurement results.*

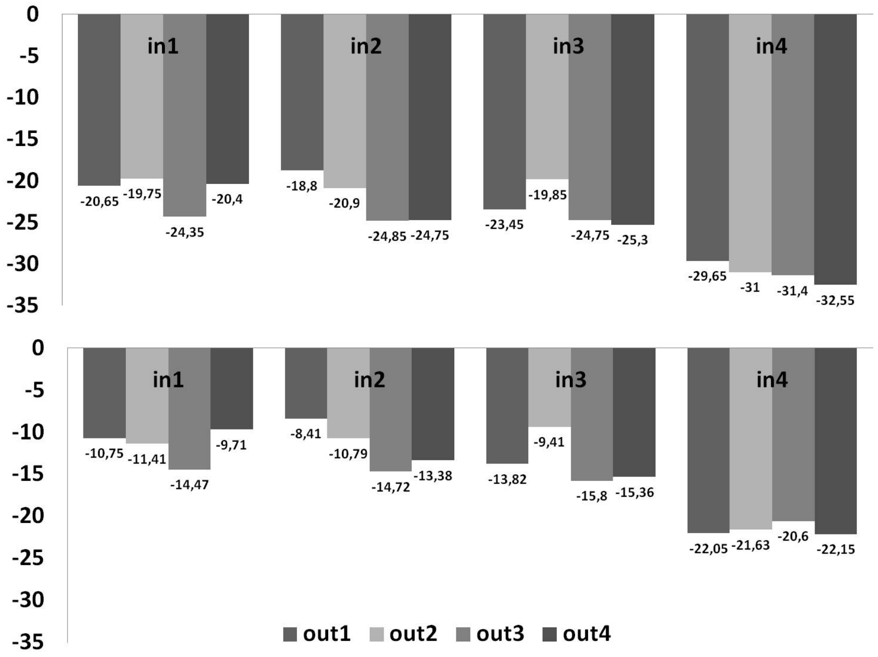

Figure 5.21: *Comparison between measurement results (top) and initial RC simulation results (bottom).*

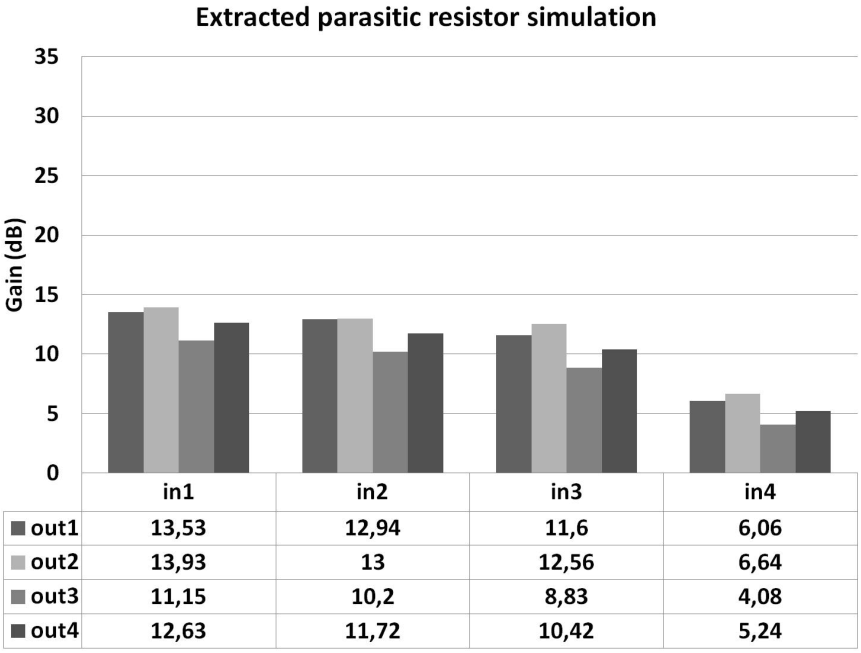

	in1	in2	in3	in4
■ out1	13,53	12,94	11,6	6,06
■ out2	13,93	13	12,56	6,64
■ out3	11,15	10,2	8,83	4,08
■ out4	12,63	11,72	10,42	5,24

Figure 5.22: *R simulation results to find DC power supply errors.*

as well, thus resulting in more voltage headroom loss. Figure 5.23 illustrates the voltage headroom loss by listing several power supply voltages across the chip. In the figure, the values below 100 mV should have been 0 V and the values above 1.1 V should have been 1.2 V. As can be seen in the figure, the Gnd connection is just 6 mV at the 3 connection entries to the inner ground mesh. The loss of the voltage headroom for the differential amplifiers is listed in Table 5.4. As can be seen in the last column, the loss of a little voltage headroom has a big influence on the bias current of the amplifiers. Any change in the biasing alters the gain of the amplifiers.

Parasitic Capacitors

To isolate the impact of the internal routing networks from the DC voltage headroom reduction, simulations were done with only the parasitic capacitors. The result of these simulation are shown in Figure 5.24. In the figure it can be seen that the distribution of the gain of the four outputs as a function of the four inputs has a similar distribution. After careful deduction the origin of this distribution

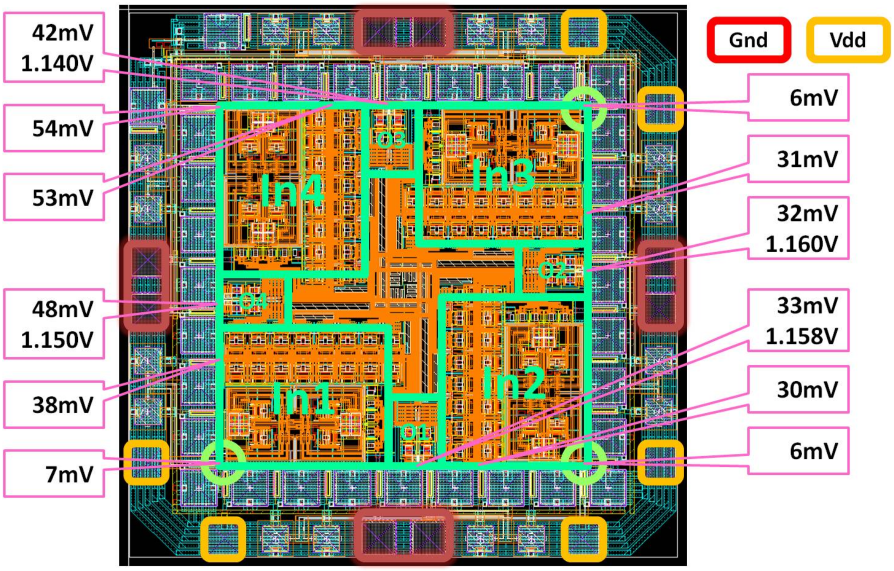

Figure 5.23: *Voltage headroom changes due to ground and power supply connection.*

Table 5.4: *Voltage of each opamp in the RC filter of the polyphase filter.*

Input block	Differential amplifier No.	Vdd (mV)	Gnd (mV)	Tail current (uA)
1	1	1175	37	81
	2	1173	28	91
	3	1173	16	107
	4	1174	33	86
2	1	1181	33	86
	2	1180	26	95
	3	1180	14	110
	4	1181	27	93
3	1	1182	38	81
	2	1180	32	87
	3	1180	16	107
	4	1182	30	90
4	1	1157	56.3	60.2
	2	1157	54.2	62.3
	3	1157	54.5	62.1
	4	1157	54.7	61.8

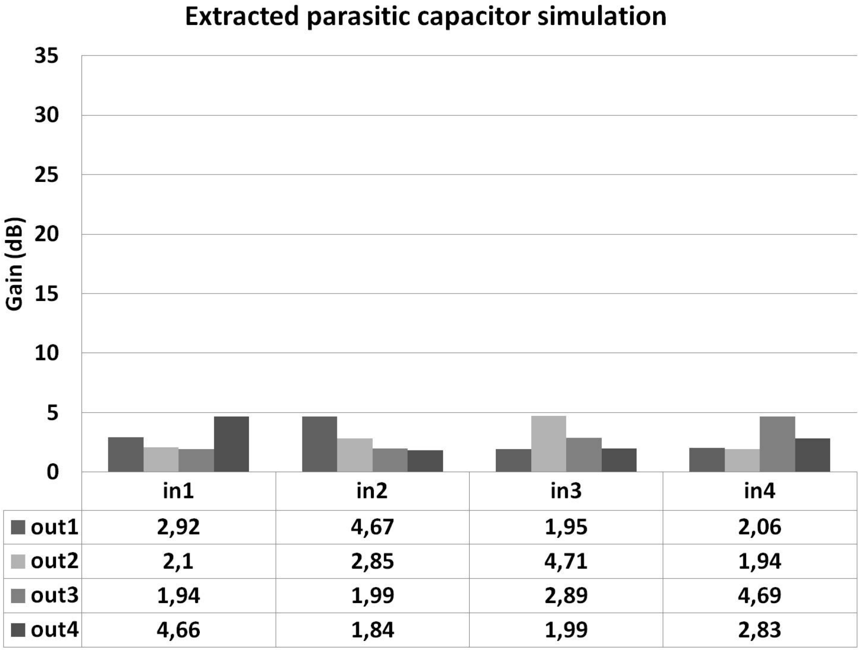

	in1	in2	in3	in4
■ out1	2,92	4,67	1,95	2,06
■ out2	2,1	2,85	4,71	1,94
■ out3	1,94	1,99	2,89	4,69
■ out4	4,66	1,84	1,99	2,83

Figure 5.24: *C simulation results to find the effect of routing.*

was traced to the second routing network. This routing network is between the phase shifters and the adders in front of the output buffers (Figure 5.6). The layout corresponding to one quarter of this routing network is depicted in Figure 5.25 along with the difference in parasitic capacitor values. Despite being in one of the highest metal layers and despite the relatively small parasitic capacitor value, the parasitic value is close to the input impedance of the adder. Due to the relatively high input impedance of the adder and the value of these parasitics, they have a relatively large impact on the output power distribution. One option to decrease the influence of these parasitic capacitors is to increase the input impedance of the adder. Another option is to put the routing in a higher metal layer and spread it over a wider area. In the current design we were restricted in area and therefore opted for a lower metal layer.

MIM Capacitors Extraction

As mentioned in the introduction of this chapter, the MIM capacitor values are extracted wrongly in the post layout simulation. To estimate that effect the ex-

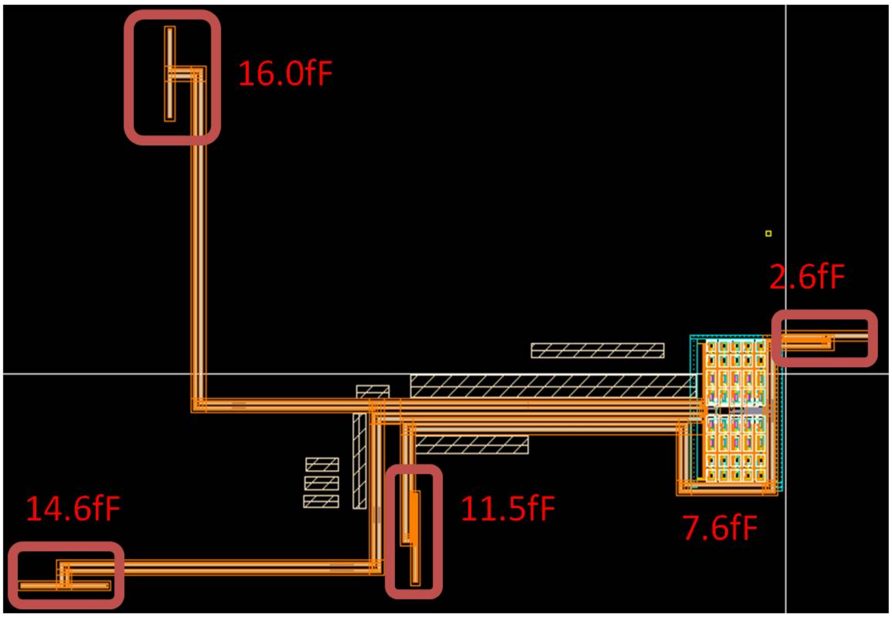

Figure 5.25: *Layout of one quarter of the second routing network.*

Table 5.5: *Estimating the effect of the erroneous MIM capacitor extraction.*

MIM cap position	Schematic simulation		extracted Value (fF)	Redo simulation	
	length(um)	value(fF)		length(um)	value(fF)
RC tank	14.3	222	435	20.5	449
phase buffer	4	20	37	6	42
output buffer	10	111	215	14.5	228
Gain(dB)	21.8			25.5	

tracted MIM cap values are used in the schematic and the results are compared to the original schematic. From simulations it became clear that the erroneous MIM cap extraction led to an overestimate of the gain (Table 5.5). This is because an increase in the capacitor values improves the in and output matching between several cascaded blocks. Table 5.6 lists the in and output impedance of individual components. It should be noted that for example the output impedance of the RC tank and the input impedance of the differential amplifier has been purposely mismatched to increase the phase rotation accuracy at the cost of gain. After correcting for the MIM capacitor extraction error the potential for gain loss improvement when only the parasitic capacitors are considered is listed in Table 5.7. Here we only consider the capacitors since the resistive parasitics mainly reduce the DC voltage headroom.

Table 5.6: *In and output impedance of individual blocks.*

Zm	RC tank	Differential amplifier	source follower	phase buffer	VGA	two adder	final adder	output buffer
input	34-j36	887-j29.23k	-2.74k-j8.46k	915-j3.38k	-176-j27.5k	472-j8.27k	650-j8.41k	2.89k-j3.35k
output	41.4-j23 31.4-j48.3	3.14k-j1.63k	616-j58	637-j141	1.27k-j173	655-j170	1.09k-j251	117-j20

Table 5.7: *Gain loss distribution due to parasitic capacitors.*

stage	RC tank	Differential amplifier	source follower	phase buffer	VGA	two adder	final adder	output buffer
gain loss (dB)	-2	5	1.5	-1	3.5	1	3/4/4/1.5	2.5
	4			8.5/9/8.5/8				

Temperature effect

Since all supply current is funneled trough just three points, we suspect that there might be a local temperature increase which alters the circuit properties. The estimated temperature at the three connection points is 80 ^{o}C. The effect of a temperature increase is depicted in Figure 5.26. The results of the figure are for a uniform temperature increase across the IC. We suspect that any temperature increase is very local and that 80 ^{o}C might be a conservative estimate. Therefore, the results in Figure 5.26 should be interpreted as an indication of the effect of a local temperature increase. The gain loss at 50 ^{o}C is 2.5 dB and at 80 ^{o}C 5.6 dB.

Total effect

The effect of the voltage headroom reduction due to the parasitic resistance, the effect of the parasitic capacitors in the routing, the effect of the erroneous MIM capacitor extraction, and the effect of an increased temperature are accounted for and results are compared to the measurement data in Figure 5.27. As can be seen in the figure there is a good match between the measured data and the simulation data. A typical example of the gain loss distribution is given in Figure 5.28.

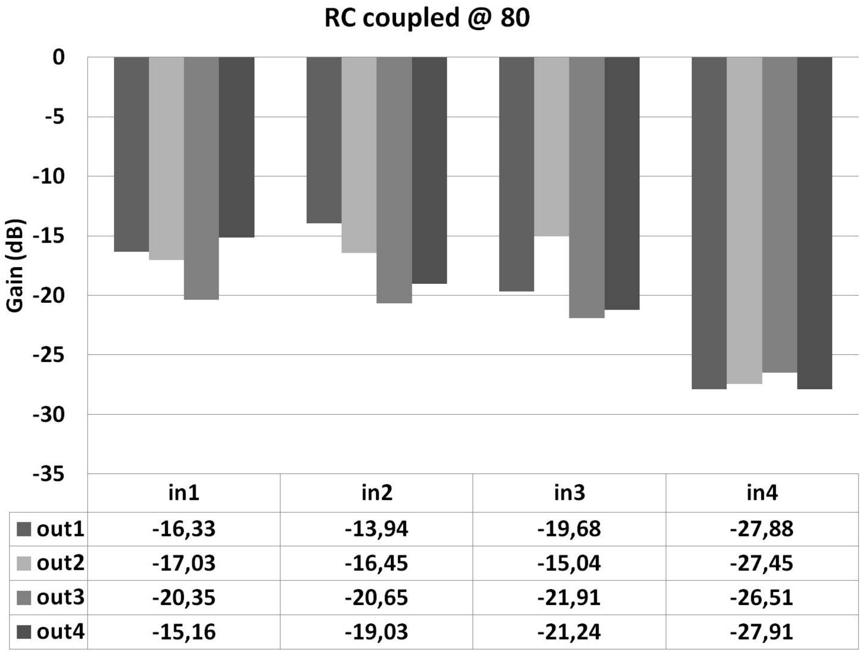

	in1	in2	in3	in4
■ out1	-16,33	-13,94	-19,68	-27,88
■ out2	-17,03	-16,45	-15,04	-27,45
■ out3	-20,35	-20,65	-21,91	-26,51
■ out4	-15,16	-19,03	-21,24	-27,91

Figure 5.26: *RC simulation results to estimate the effect of IC temperature increase.*

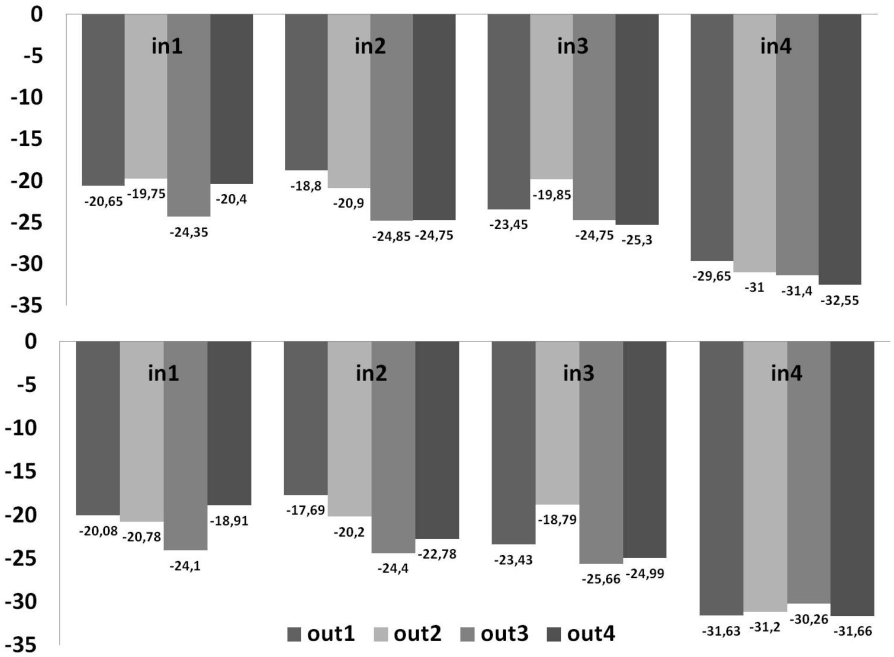

Figure 5.27: *The measured data (top) compared to the corrected RC simulation results (bottom).*

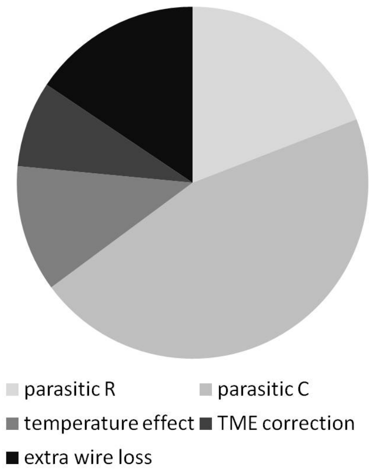

Option	Gain or Gain loss (dB)
Schematic result	21.75
Measurement result	-27.35
Total gain loss	49.1
Found gain loss	48.1
error	1

Figure 5.28: *Gain loss distribution (for input 3 to output 2).*

Next steps

There are several options to improve the gain performance of the IC such as:

- Redesign Vdd/Gnd wire and connection. This has been done in the simulator. Simulation results indicate a 10 dB gain improvement.
- Improve the parasitic capacitor effect (5-10dB). This can be done by putting the internal routing in the highest metal layer and spread it over a wider area. However, the penalty is a significant increase of the surface area of the IC. Due to our area restriction we used a lower metal layer.
- Improve the pad location to better align output and input routing. This can be done by changing the entire layout and locating the RF input pads and the RF output pads on opposite sides of the circuit. However the penalty is a significant increase of the surface area of the IC. Due to our area restriction we used two square pad rings around the circuit.
- Improve the temperature effect by e.g. spreading parallelling functionality and connection wires. Again here the penalty is an area increase.
- A new design of low power LNA at the beginning of the cascade. This helps for the current stand alone IC, but is not necessary in a fully integrated circuit.

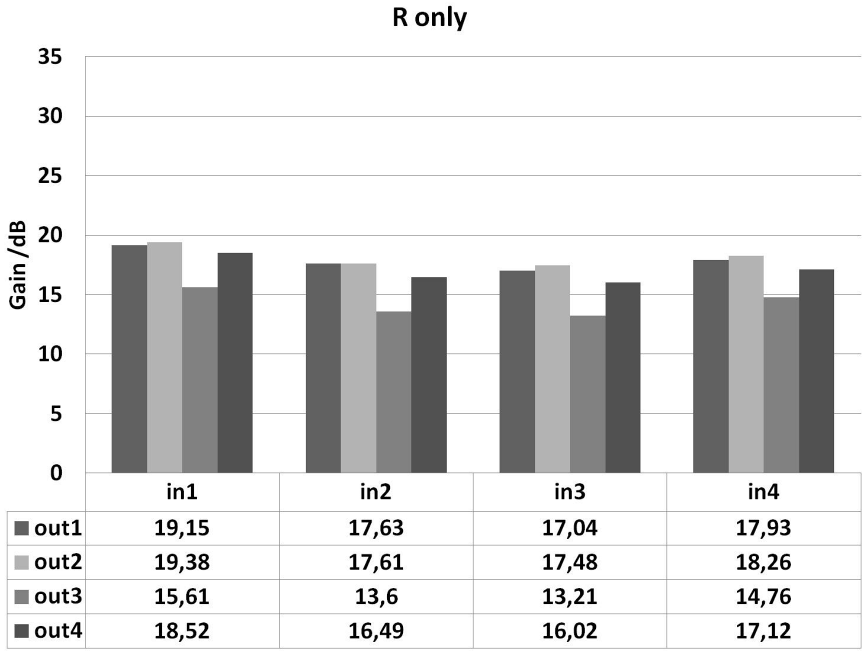

	in1	in2	in3	in4
■ out1	19,15	17,63	17,04	17,93
■ out2	19,38	17,61	17,48	18,26
■ out3	15,61	13,6	13,21	14,76
■ out4	18,52	16,49	16,02	17,12

Figure 5.29: *R simulation results to find DC power supply improvements by improved ground wiring.*

Related to the first bullet, we restored the ground mesh connections in the simulator to their originally intended state and thereby improved voltage headroom. The results of the improved ground mesh connection are shown in Figure 5.29 and Figure 5.30. When we compare the results in Figure 5.30 to Figure 5.19 we can see that the gain improvement caused by the improved ground mesh wiring is in the order of 10 dB per branch. For use of the ACMM in the test bench this gain is good enough. The gain is needed to drive the input buffer of the ADC in the test bed and is not needed for the spatial filter functionality of the circuit.

5.7 Benchmarks

If the ACMM is integrated in an existing 4x4 MIMO system, the system can operate in a lower power mode when an interferer is spatially filtered. The overall effectiveness of the ACMM depends on several parameters:

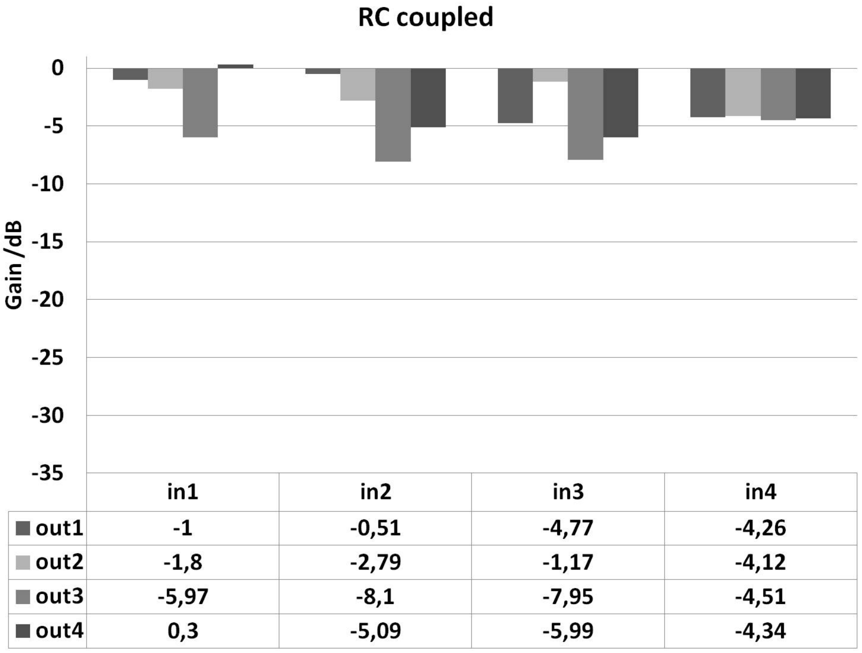

	in1	in2	in3	in4
■ out1	-1	-0,51	-4,77	-4,26
■ out2	-1,8	-2,79	-1,17	-4,12
■ out3	-5,97	-8,1	-7,95	-4,51
■ out4	0,3	-5,09	-5,99	-4,34

Figure 5.30: *RC simulation results to find DC power supply improvements by improved ground wiring.*

1. The RF bandwidth of the system, which contains desired users and interferers
2. The delay spread of each user and interferer channel, which determines the coherence bandwidth of each channel and thus the effectiveness of a common preconditioning matrix over the relevant part of the RF bandwidth.
3. The accuracy of the elements of the ACMM over the RF frequency band.
4. The number of receiver antenna elements.

Currently, it is common practice to design a receiver to operate at a predetermined (worst case) CIR level. We will benchmark our solution for this worst case, assuming a strong interferer at a CIR of -40 dB. At such high interference levels, the interferer is typically close to the receiver, so it is realistic to assume a short delay spread. To simplify our analysis, we also assume that the interferer arrives via a single angle of arrival, but this is not a fundamental constraint of our circuit architecture. Further, again only for simplification, it is assumed that the four desired Eigenvalues each consist of a single reflection. More complex and realistic channel model simulations are reported in Chapter 6. The reported results are in agreement with the simplified channel model of this section. Due to the finite accuracy of the ACMM, the interferer cannot be canceled fully if the difference in AOA of one of the four reflections of the desired user and the reflection of the interferer is smaller than the angular resolution with which the ACMM can set a minimum. The angular resolution of the ACMM depends on the achievable control accuracy of the elements of the ACMM over the considered bandwidth, and the number of antenna elements. For a uniform angle of arrival, under the constraint of our current channel assumption, the probability that the interferer and desired signals effectively overlap for four receive antennas and cannot be separated is less than 1% in our ACMM realization of 5 bit I and Q accuracy over a bandwidth of a 100 MHz. At all other angles of incidence, the power consumption of the RF front end and of the ADC, can be reduced substantially by exploiting the CIR improvement method demonstrated here [72] and predicted theoretically already in [18] [16]. Given the current channel assumptions, the probability that all four desired reflections overlap with the AOA of the interferer (and thus the MIMO receiver needs to operate at full power including the ACMM power consumption) is in the order of 10^{-8}. At all other instances the receiver can scale back power consumption of at least one receiver chain, if its linearity and ADC settings are adaptive. If the linearity setting of the receiver is not adaptive, the receiver could still operate in a lower power mode. The increased linearity of the front end will impact negatively on the average bit-error-rate, but on the other hand this is outweighed by the enabled CIR improvement which acts positively on the average bit-error-rate. The exact trade-off is beyond the scope of this chapter. The simulated power consumption of the ACMM core, excluding the output buffers, is 12 mW. The measured power consumption of the entire IC including output buffers and PCB board is 136 mW. Since our ACMM building block enables a CIR improvement, power consumption can be opportunistically reduced for a typical MIMO receiver for all blocks after the ACMM block depending on the current channel conditions. In our calculation, the power consumption of the LNAs is estimated at around 4% of the original total RF circuit power consumption. Under our channel assumptions, our solution showed an average improvement of 90 to 96% of the time-average power consumption, given the presence of a strong interferer (Table 5.2). If spatial filtering can be applied to unamplified antenna signals at a sufficiently low NF, the LNA power can be reduced as well. The average power reduction for 5 bits accuracy over a 100 MHz band can then be estimated to reach almost two orders of magnitude. However, the power spend in the matrix is still an overhead.

Figure 5.18 shows the IC, the IC board, and the LNA board. The chip is mounted in a cavity. The 65 nm CMOS chip occupies 1.2 mm2 including bond pads. This IC has been successfully used in a proof-of-concept measurement. This validates our claim that with our approach, MIMO receivers using over 90% less power than state of the art solutions can be realized, when MIMO receivers include the novel ACMM building block.

5.8 Conclusions

A novel MIMO receiver architecture has been introduced containing a novel ACMM building block which exploits the spatial selectivity of the MIMO channel in the analog domain. The ACMM IC has been implemented in 65 nm CMOS and operates in the 2.4 GHz band. To the best of our knowledge the ACMM is the first realization of an analog spatial filtering of interference at RF to alleviate the DR requirements of the receiver and ADC in a MIMO system. Earlier this concept has been simulated by us (Chapter 6), and the substantial performance gain has been confirmed by our test. In contrast to regular beamforming the ACMM allows for all MIMO data streams. The control accuracy of the ACMM is 5 bits I and 5 bits Q per matrix element over a 100 MHz band. Measured CIR improvement is 37 dB at an AOA difference of 45°. The measurements confirm that the expected average power consumption reduction over time of a MIMO system including an ACMM building block is over 90%.

Chapter 6

Analog Spatial Filtering in Wideband Cognitive Radio

6.1 Introduction

In the previous chapter we showed spatial filtering in an IEEE 802.11n context. To support the practical feasibility of our approach in Chapter 5, an IC implementation of an analog 4×4 ACMM full MIMO spatial filter at an RF of 2.45 GHz has been realized in 65nm CMOS, and it is confirmed via measurements that analog interference suppression is effective. The implementation and measurement results are documented in Chapter 5 and submitted in the RF community in [72]. However, the principles of spatial filtering are also applicable to other frequencies and channel bands. Therefore, in this chapter we apply the same spatial filtering principles as shown in Chapter 5, but now applied to cognitive radio. More specifically, we determine the potential benefits of spatial filtering in terms of increased throughput (bit/s/Hz), and we quantify the potential power savings in terms of ADC quantization bits. Our approach in this chapter is as follows:
i) extending [18], from a vector beamformer to the novel receiver architecture including a full rank analog complex matrix multiplier (ACMM) (which was introduced in Chapter 5), which allows for full MIMO spatial filtering. In contrast

to the wideband vector beamformer from [18], and the narrowband rank reduced matrix from [74], our full rank wideband MIMO spatial filter separates all spatial streams simultaneously, hereby significantly increasing system capacity.
ii) The channel model is expanded to the full MIMO case and novel DSP algorithms for computation of MIMO spatial filter coefficients are proposed.
iii) Analysis of DR reduction in different wireless propagation environments modeled via ray tracers.
iv) Analysis of the effect of quantization in the filter implementation.
The Chapter is structured as follows: Section 6.2 introduces the model for respectively the radio front-end, the ADC, the signal, and the wideband multiple antenna channel models. Section 6.3 includes the throughput calculation, the beamforming algorithms, and the MIMO spatial filtering algorithm. Section 6.4 gives the numerical results of the beamforming and spatial filtering algorithms for various channel conditions. Finally Section 6.5 concludes this chapter.

With the continued increase in the number of users in the crowded pre-allocated parts of the radio spectrum, a more efficient use of the available spectrum is required. To increase spectrum utilization, a cognitive radio (CR) continuously senses and uses unoccupied channels in a wideband spectrum, alleviating congestion and improving the overall throughput.

In a typical CR scenario there are multiple primary and secondary user transmissions over a wide bandwidth and the desired user only occupies a small portion of the band [6, 75, 76]. Contrary to the front end of Chapter 5, now the entire RF band is filtered, down converted, and finally sampled by an ADC. Final channel selection occurs in the digital domain. As mentioned in Section 3.7, before final digital filtering can be performed, in most systems the radio frequency (RF) front end and analog-to-digital converter (ADC) need to handle the interfering users via extra dynamic range (DR). Unfortunately, additional DR requirements make the RF and ADC power hungry [10, 77, 78]. The DR and sample rate requirements of the ADC depend on the combination of the interference power level with which the receiver needs to cope, both inside and outside the band, and these are a trade off with the analog filter selectivity [11]. As mentioned in Section 2.2.2, the power consumption of ADCs currently reduces approximately with an order of magnitude every decade [37, 49]. In the absence of disruptive new technologies, we expect this power trend to continue for the foreseeable future. In a CR several users with various received power levels are sampled simultaneously. At a typical power level difference of 40 dB for an undesired user, the ADC requires 6.64 more effective bits to maintain similar effective resolution for the desired user compared to an interference free case. This additional ADC bit requirement leads to an approximate 100 times increase in the required ADC power consumption, compared to what is necessary for the interference-free case. The power requirements of, for example, high sampling speeds (e.g. 1 GHz), and high resolution (10/12 bits) ADCs required for the IEEE 802.22 standard have thus far been prohibitive for the wide spread use of CR.

Since the received signals come from distinct spatial angles, multiple antennas can be used at the receiver to resolve them (Section 3.3). Systems that include multiple receive antennas can be realized as vector beamformers (multiple antennas with combining in the analog domain and a single ADC) and full MIMO (multiple antennas with an ADC per antenna). The concept of spatial filtering via vector beamforming to reduce interfering users was first introduced in [70]. In [74], a narrowband channel in combination with a rank reduced analog matrix is studied. In [18], the benefit of a vector beamformer as a spatial filter to reduce interference power levels is analyzed for a wideband channel, and it is shown that spatial filtering has the potential to reduce ADC power consumption with over 90%.

6.2 System Model

In this section firstly two receiver architectures from Chapter 5 for spatial filtering are reintroduced, namely a vector beamformer spatial filter and a MIMO spatial filter. Specifically, the impact of the difference between the IEEE 802.11n scenario and the CR scenario on the architectures is explained. Secondly, the ADC power consumption model is introduced, to allow quantitative analysis of power savings obtained by our proposed architectures. Thirdly, our signal model is based on OFDM signaling. Finally, wideband channel models for realistic propagation environments are introduced, namely i.i.d. Rayleigh fading per subcarrier, and a wideband MIMO ray tracing model.

6.2.1 Front End Architectures

Contrary to the RF front end of Chapter 5, the sampled broadband BB signal contains the interfering users as well as the desired signal. The CR RF front end chain and the ADC have to deal with a broadband RF signal. To prevent clipping of the ADC, an automatic gain control (AGC) amplifies the entire wideband spectrum to an appropriate level. To prevent excessive spill over of interfering signals into the desired signal band, the analog front end needs to have adequate linearity. After analog channel selection within the wide bandwidth via mixing and non ideal analog filtering, the signal presented to the analog-to-digital converter (ADC) consist of the desired user, interfering users, and leftover adjacent channel interference products. To prevent aliasing of the adjacent channel interferer into the desired channel it is necessary to over-sample, and headroom bits are required to guarantee adequate resolution for the desired signal. The filtered signal is further processed in the baseband (BB) domain by the digital signal processing (DSP) for the purpose of spectrum sensing and/or narrowband reception. A co-channel interferer can be filtered digitally using a combination of coding, timing, and frequency hopping schemes. In full MIMO antenna systems, the BB DSP can also use matrix beamforming techniques to spatially filter co-channel interferers, but this digital filtering requires a powerhungry ADC per receive antenna with large DR.

Vector Beamforming

In contrast to Section 5.2, the I and Q baseband signals contain all users. The I and Q signals are low pass filtered, set to an adequate gain for the ADC by an AGC, and then quantized by an ADC. Figure 5.3 depicts a CR receiver with a vector beamforming architecture acting as an analog vector spatial filter. The considered beamforming system architecture consists of a commonly used zero IF architecture combined with several receive antennas, each with their own RF-filter, LNA, and phase shifter. The outputs of the phase shifters are combined and presented to an in-phase I and quadrature Q mixer which downconverts the combined RF frequency band to baseband with the signal provided by the local oscillator (LO).

Full MIMO Spatial Filter

Contrary to the architecture of Section 5.2, the ADCs now sample a broadband BB signal containing all users. The architecture depicted in Figure 5.4 and processes parallel RF signal streams in the form of a MIMO receiver with an independent ADC per antenna. The architecture includes a similar RF analog complex matrix multiplier (ACMM) as in Section 5.2, which is implemented as a matrix of complex multipliers and adders (Figure 5.6). In contrast to the vector beamformer, the considered full MIMO spatial filter addresses all spatial streams simultaneously, hereby significantly increasing system capacity. The considered MIMO architecture consists of a commonly used zero IF architecture combined with several receiver antennas, each with their own RF-filter and LNA. The outputs of the LNAs are inputs to a matrix operation at RF. The outputs of the matrix are each presented to an in-phase I and a quadrature Q mixer which down converts the RF signal to baseband with the signal provided by the shared local oscillator (LO). The composite I and Q baseband signals containing all users are low pass filtered, set to an adequate gain for their ADC by an AGC, and then quantized by the ADCs.

Mismatch

There are two kinds of mismatches that impact overall system performance. The first form is impedance mismatch between two stages of a receiver chain. The second form is a difference in physical attributes between paths in the receiver, caused for instance by process spread, and parasitic differences attributable to e.g. routing in the layout. Many of the latter form of mismatches, particularly differences in signal branches, can not be distinguished from random channel realizations, so these can be partly or entirely corrected by our proposed solution. In particular the feedback loop (see Figure 5.4) compensates mismatch artifacts that appear in the base band, by setting the ACMM appropriately. However, these mismatches have not been part of the simulation in this chapter. On the other hand, impedance mismatches lead to a penalty in the noise performance. In our IC realization (Chapter 5), we achieved a proper gain and phase control by buffering the signals, feeding it into an RC hybrid, and applying a high-impedance, voltage controlled I and Q amplification. This avoids mutual coupling of the settings of the various matrix elements, but potentially does not achieve the highest noise performance. This noise penalty can be acceptable because it is applied to input signals that are already preamplified. Yet, this of course puts more stringent requirements on the noise performance, gain and dynamic range of the first LNA amplifiers. On the other hand, dynamic range reduction achieved by spatial filtering impacts power consumption of stages behind the ACMM favorably, where power spent in the spatial filter is an overhead. A full analysis of the power consumption trade-off of the entire chain, including LNA, AGC, mixer and ADC is beyond the scope of this chapter, but in [14–16] and Chapter 4, we published a framework that potentially can model this. In our model we purposely omit mismatch in the analog front end, since mismatch heavily depends on the technology and the specific design in that technology [79], which are beyond the scope of this chapter.

6.2.2 Analog-to-Digital Converter

To guarantee adequate resolution, dynamic range for the desired user, and receiver sensitivity for spectrum sensing, additional headroom bits are required in the presence of strong interference levels. Unfortunately, the power consumption of an ADC grows exponentially with the number of bits. As mentioned in Section 3.6, a commonly accepted ADC power model is,

$$P_{\mathrm{ADC}} \sim \kappa_t F_s 2^{b_{\mathrm{ADC}}}, \tag{6.1}$$

where F_s is the sample frequency of the ADC, κ_t a technology constant and b_{ADC} the number of ADC bits [37] [49]. With respect to the required resolution, it is expected that typically a wideband signal containing several users with various power levels is presented to the baseband ADC. According to commonly used standards, a receiver needs to adequately receive the desired user even if power levels of the adjacent channel users are substantially larger than the desired user. A typical value, e.g. specified by the IEEE 802.11 standard, is 40 dB. To guarantee sufficient resolution for the desired user in the presence of such large adjacent channel users, additional bits for the ADC are required. In case adjacent channel users of 40 dB larger than the desired user need to be sampled together with the desired user, an additional DR of 40 dB is required. This results via (6.1) to an overal P_{ADC} increase of 100 times and translates to an additional number of bits per ADC of $1/2\log_2(10^4) = 6.64$ bits. Not only does the ADC in a CR have to deal with interfering users inside the desired wide frequency range, but also with left over interference products outside of the desired frequency range. This poses further demands on the ADC. The number of additional headroom bits therefore depends on both the standard and the practical implementation. In this chapter the goal is to reduce the number of bits for the ADC in order to save power, while maintaining the CR system throughput.

6.2.3 Signal Model

As mentioned in Section 3.2, Orthogonal Frequency-Division Multiplexing (OFDM) is a popular modulation method in wireless communication due to its ability to cope with severe channel conditions. Opportunistic use of spectrum in CR (as proposed in the IEEE 802.22 standard) can be achieved via OFDMA. Thus we assume the CR signals are wideband OFDM. The baseband equivalent of an OFDM signal over one signal period T_s is expressed as

$$s(t) = \sum_{k=-\frac{K}{2}}^{\frac{K}{2}-1} L_k e^{i2\pi\frac{kB}{K}t}, \tag{6.2}$$

here t is time, B is the bandwidth of the signal, K is the number of OFDM frequencies, the symbol time $T_s = \frac{K}{B}$, and L_k is the data symbol of the k^{th} OFDM frequency.

6.2.4 Wide Band Multiple Antenna Channel Models

Since all users use an OFDM scheme, the receiver channelizes the spectrum through the use of an FFT. As a result, the wideband spectrum can be considered as a set of narrowband signals, but with correlated fading between subcarriers (characterized by the delay spread) and between different antennas (characterized by the angular spread) [80]. One extreme model would be to assume that all antennas and all subcarriers see fully uncorrelated fading. This results in extremely rich multipath, thus high theoretical capacity gains. However, this scenario can not be handled effectively by a frequency non-selective ACMM, except in the special case of $K = 1$ subcarrier or only very few. However, it is reasonable to claim that this scenario is too rich to be useful in a cognitive wideband setting. Another extreme occurs if all paths of one source arrive from the same direction, such that the beamformer can perform an angular separation even if the channel is frequency selective. A third extreme case occurs if the angular spread is large (independent and identically distributed (i.i.d.) fading per antenna), but the RMS delay spread is small (flat fading). In this case, a frequency non-selective ACMM, can be effective. Moreover, we claim that an ACMM can also be effective if the wanted signal sees frequency selective fading, as long as the RMS delay spread of the interference is small (flat fading). As mentioned in the introduction, the receiver needs to cope with large interferers which are typically 40 dB larger than the desired user. We consider it reasonable to assume that such a large interferer is in close proximity to the receiver, resulting in a small RMS delay spread. The RMS delay spread is defined as

$$\tau_{\mathrm{RMS}} = \sqrt{\frac{\int_0^\infty (\tau - \bar{\tau})^2 A(\tau) d\tau}{\int_0^\infty A(\tau) d\tau}}, \tag{6.3}$$

where $A(\tau)$ is the power delay profile and the mean delay of the channel is

$$\bar{\tau} = \frac{\int_0^\infty \tau A(\tau) d\tau}{\int_0^\infty A(\tau) d\tau}. \tag{6.4}$$

In order to investigate the effects of some moderate degree of spatial and frequency correlation of indoor and urban wireless channels on system performance, we used a ray tracer to model various channel realizations. The ray tracer calculates the channel for each subcarrier corresponding to the various multi paths between each transmit and receive antenna. The uncorrelated Rayleigh Fading channel model is used as a benchmark to test the beamforming algorithms. Next we will introduce a ray tracer model based on a wideband channel model that accounts for the angular spatial correlation in the wideband channel. We analyze the special flat fading case of $K = 1$ subcarrier in combination with the uncorrelated Rayleigh Fading channel model for the beamformer first. Secondly, we analyze the effect on the beamformer of shifting from flat fading to frequency selective fading via the ray tracer channel model, by increasing the RMS delay spread of both the signal and the interferer. Finally, we analyze the ACMM with the ray tracer channel model in case of frequency selective fading of the wanted signal and flat fading of the interferer.

Independent Rayleigh Fading per Subcarrier

Consider a transmission system that consists of N_t transmit antennas and N_r receive antennas. Each transmit antenna corresponds to a primary or secondary transmitter in the CR network. If a narrowband complex signal $\mathbf{s}$ is transmitted, the received signal $\mathbf{r}$ on a specific subcarrier can be expressed as

$$\mathbf{r} = \mathbf{H}\mathbf{s} + \mathbf{n}, \tag{6.5}$$

where $\mathbf{H}$ is a $N_r \times N_t$ complex channel-gain matrix and $\mathbf{n}$ is a complex N_r-dimensional additive white Gaussian noise (AWGN) vector. For spatially-uncorrelated Rayleigh fading, the entries in $\mathbf{H}$ are independent and identically distributed (i.i.d.), complex, zero-mean Gaussian with unit magnitude variance. The results simulated for this case are valid for $K = 1$ subcarriers per primary or secondary transmitter (flat fading), but also if all subcarriers see the same channel $\mathbf{H}$ (flat fading, small delay spread).

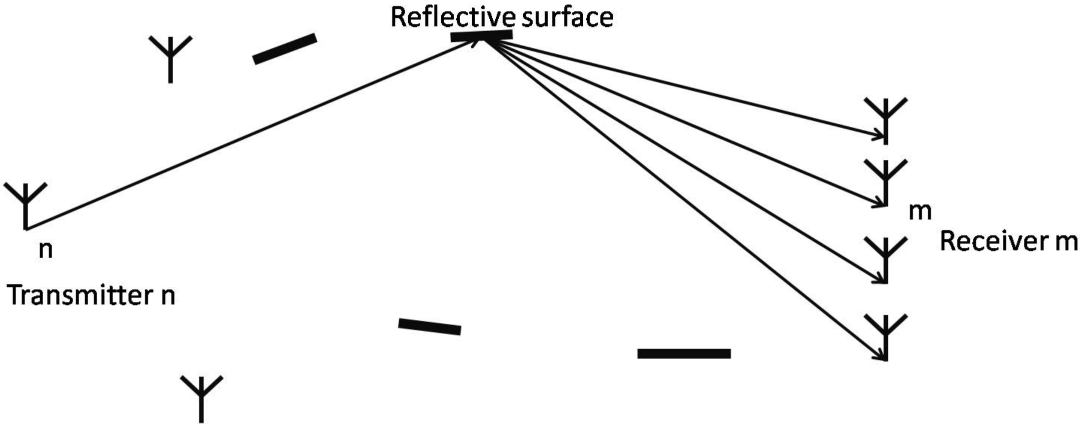

Figure 6.1: *SIMO wideband channel model consisting of N_t transmit antennas, each with P reflectors, and a receiver array of N_r receive antennas.*

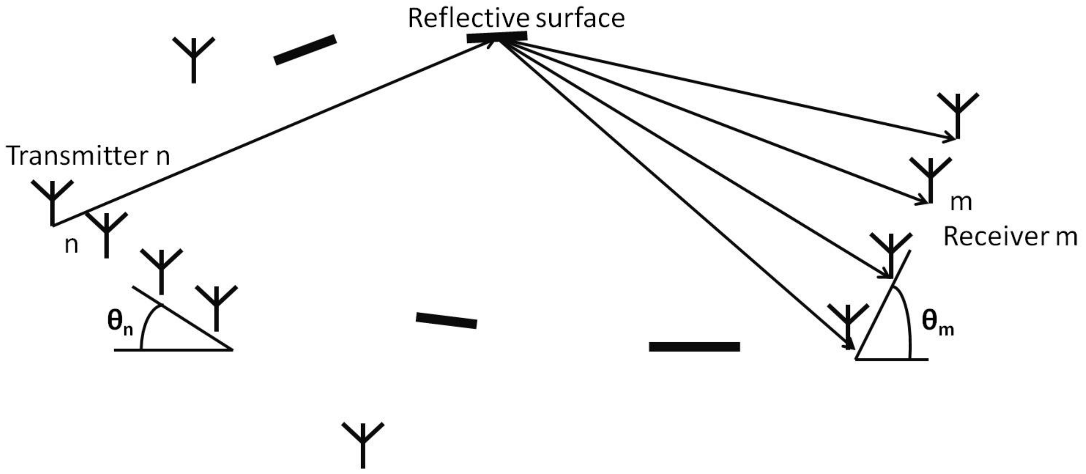

Figure 6.2: *Full MIMO wideband channel model consisting of N_t transmit antennas of which the desired transmitter is an antenna array of size N_{td}, P reflectors per transmitter, and a receiver array of N_r receive antennas.*

Ray Tracer

To study cases with moderate degrees of correlation, we used a wideband channel model [81], based on ray tracing [82]. The proposed model is depicted for the SIMO beamforming architecture of Figure 5.3 in Figure 6.1 and for the full MIMO architecture of Figure 5.4 in Figure 6.2. The beamforming model consists of N_t transmit antennas, each with P multipath components and a receiver array consisting of N_r receive antennas. Each N_t transmit antenna corresponds to a primary or secondary transmitter in the CR network. The full MIMO wideband channel model consists of N_t transmit antennas of which the desired user is a transmitter with an antenna array of size N_{td}, the undesired users are transmitters with one antenna, each of the $N_t - N_{td} + 1$ transmitting users has P multipath components, and the receiver array consists of N_r receive antennas. In the ray tracer model each channel for each OFDM subcarrier for each transmit and receive antenna is calculated. The baseband equivalent of the received signal without noise

$$\mathbf{y} = \mathbf{H}\mathbf{s} \tag{6.6}$$

at the m^{th} antenna of the wideband channel models is given in time domain by

$$y_m(t) = \sum_{p=1}^{P} a_{n,m,p} e^{-i2\pi f(t-\tau_{n,m,p})} s_n(t) \tag{6.7}$$

where $s_n(t)$ is the transmitted signal of the n^{th} transmit antenna, P is the number of multipath components, and $\{a_{n,m,p}\}$ and $\{\tau_{n,m,p}\}$ are the random complex amplitude and random arrival time coefficient sequences of the multipath components between transmit antenna n and receive antenna m.

In the proposed SIMO ray tracer channel model, each transmit source has a unique set of reflectors. The transmit antennas and corresponding reflectors are randomly placed in a two dimensional space according to a Gaussian distribution with a variance of σ_n^2 and $\sigma_{n,p}^2$ in each dimension of a Cartesian coordinate system, respectively. The center of the receiver array is randomly placed in the two dimensional space according to a Gaussian distribution in each dimension of the Cartesian coordinate system with a variance of σ_m^2; the antennas are spaced in a uniform lineair array according to an inter element distance of half the wavelength of the carrier frequency λ_{car}; the carrier frequency is the center frequency of the considered RF band; and the angle of the receiver array θ_m in respect to the origin is randomly set according to a uniform distribution over all angles $\theta_m \in [0, 2\pi]$. In the full MIMO case the transmitter consists of more transmit antennas. The center of the transmitter array is randomly placed in the two dimensional space according to a Gaussian distribution in each dimension of a Cartesian coordinate system with a variance of σ_n^2; the antennas are spaced in a linear array according to an inter element distance of half the wavelength of the carrier frequency λ_{car}; the carrier frequency is the center frequency of the considered RF band; and the angle of the transmitter array θ_n in respect to the origin is randomly set according to a uniform distribution over all angles $\theta_n \in [0, 2\pi]$.

The path signal strength coefficients are defined as

$$a_{n,m,p} = r_{n,p} \left(\frac{c}{f 4\pi d_{n,m,p}} \right) \tag{6.8}$$

and the delays as

$$\tau_{n,m,p} = \frac{d_{n,m,p}}{c} \tag{6.9}$$

were $r_{n,p}$ is complex, zero-mean Gaussian with unit magnitude variance, c is the speed of light, f is frequency, $d_{n,m,p}$ is the distance between transmitter n and reflective surface p plus the distance between reflective surface p and receive antenna m. In case the p^{th} multipath is a line of sight (LOS) signal, $d_{n,m,p}$ is the distance between transmitter n and receive antenna m and $r_{n,p} = 1$.

The baseband equivalent of the received OFDM signal without noise is now expressed as

$$y_m(t) = \sum_{k=-\frac{K}{2}}^{\frac{K}{2}-1} \sum_{p=1}^{P} L_k a_{n,m,p} e^{-i2\pi \frac{kB}{K}(t-\tau_{n,m,p})} \tag{6.10}$$

were $a_{n,m,p}$ is a function of subcarrier index k and the carrier frequency.

6.3 Spatial Filtering Approach

6.3.1 Problem statement

Our goal is to quantify the potential power savings of spatial filtering in terms of number of ADC bits. To this aim we maximize the throughput that is achievable for a given ADC resolution in combination with a spatial filter. This throughput calculation has to account for the quantization effect of the ADC, because we are assuming that the ADC is the bottleneck. In the presence of strong in-band interference, we would like to utilize the ADC resolution as effectively as possible for the desired user. Firstly we will model the quantization noise, secondly we insert the quantization model in the throughput calculation. The model will be a generalized model to enable analysis of both the vector SIMO beamformer and the full MIMO spatial filter architectures. Then, we proceed with the development of the spatial algorithms, and evaluate their performance throughput. We assume perfect channel state information (CSI) at the receiver Rx. On the other hand, the transmitter Tx does not know CSI and therefore cannot optimize the transmission based on the interference. Note that CSI at Tx requires feedback, which is complex to implement in practice. In addition, we assume perfect channel knowledge at Rx, as opposed to estimated, in order to study performance of the spatial filter independently from the channel estimation algorithm.

Quantization Noise

The input signal is quantized in the time domain, while the OFDM symbols are extracted after an FFT of the input signal. The received signal after the analog spatial filter $\mathbf{U}$ (which is a complex valued matrix of size $(N_r \times N_r)$ in the MIMO case, and a complex valued vector of size $(1 \times N_r)$ in the beamforming case), is now modeled in the frequency domain for all K frequency components as

$$\mathbf{r_k} = \mathbf{U_k}(\mathbf{H_k}\mathbf{s_k} + \mathbf{n_{th,k}}) \tag{6.11}$$

were

$$\mathbf{s_k} = \mathbf{x_k} + \mathbf{n_{int,k}} \tag{6.12}$$

Here $\mathbf{r_k}$ is the complex valued received signal vector of size $(N_t \times 1)$ in the full MIMO case and a complex valued scalar in the beamforming case, $\mathbf{x_k}$ is a complex valued transmit vector of size $(N_t \times 1)$ containing the complex components corresponding to the transmitted desired user, $\mathbf{n_{int,k}}$ is a complex valued transmit vector of size $(N_t \times 1)$ containing the non zero complex components corresponding to the interfering users, $\mathbf{H_k}$ is the complex current channel state matrix of size $N_r \times N_t$, $\mathbf{U_k}$ is a complex valued matrix of size $(N_r \times N_r)$ in the MIMO case, and a complex valued vector of size $(1 \times N_r)$ in the beamforming case of the analog spatial filter, and $\mathbf{n_{th,k}}$ is a complex valued thermal noise vector of size $N_r \times 1$ at the k^{th} frequency. According to the central limit theorem we can model the quantization noise in the frequency domain as AWGN [83] [84]. To simplify the mathematics, the AGC sets the variance of the combined input signals equal to the variance of the input signal for an idealized ADC, which only generates quantization noise. With a unit magnitude scaling the boundary condition for the AGC is

$$\sum_{k=1}^{K} \mathbb{E}\left[\mathbf{r_k}\mathbf{r_k}^*\right] = \rho_{\mathrm{ADC}} \sum_{k=1}^{K} \mathbb{E}\left[\mathbf{n_{q,k}}\mathbf{n_{q,k}}^*\right], \tag{6.13}$$

where K is the total number of unique OFDM frequencies of $\mathbf{x}$ and $\mathbf{n_{int}}$, $\mathbf{n_{q,k}}$ is the quantization noise at the k^{th} subcarrier, and $\rho_{\mathrm{ADC}} = 2^{2b_{\mathrm{ADC}}} - 1$ is the SNR of an idealized complex input ADC. Due to considerations such as large peak to average power ratios and clipping prevention, the input signal could have a different scaling than the unitary scaling that is now applied in (6.13) [83].

Throughput model

By modeling the quantization noise as AWGN we can use the capacity equation to calculate the throughput [83] [84]. Since this is an approximation, this throughput should not be interpreted as the Shannon capacity given by [3] [2]. Lacking a better model we use the capacity equation as a proportional measure of achievable throughput. The throughput is derived via similar steps as in [3] [2] [85], and the result is given by

$$T = \max_{\mathbf{K}_x:\mathrm{Tr}[\mathbf{K}_x]\leq P} \mathbb{E}_{\mathbf{H}} \left[\log\det \left(\mathbf{I}_{N_r} + \sum_{k=k_1}^{k_\mathrm{K}} (\mathbf{U_k H_k K_{x,k} H_k^* U_k^*}) \left[\sum_{k=k_1}^{k_\mathrm{K}} (N_{th,k}\mathbf{U_k U_k^* I}_{N_r} + \mathbf{N_{q,k}}) \right]^{-1} \right) \right] \tag{6.14}$$

where $k_1 \dots k_\mathrm{K}$ are the frequency components of the OFDM symbols of the desired user $\mathbf{x}$; $\mathbf{K_{x,k}} = \mathbb{E}[\mathbf{x_k x_k^*}] = P/(N_{td}K)\mathbf{I}_K$ is the expected transmit power matrix of size $N_t \times N_t$; $N_{th,k}\mathbf{I}_{N_r} = \mathbb{E}[\mathbf{n_{th,k} n_{th,k}^*}]$ is the expected thermal noise at the receiver of size $N_r \times N_r$; and $\mathbf{N_{q,k}} = \mathbb{E}\left[\mathbf{n_{q,k} n_{q,k}}^*\right]$ is the expected quantization noise matrix of size $N_r \times N_r$ in the full MIMO case and a scalar in the beamforming case. Due to the AGC constraint of (6.13) the expected quantization noise can be written as

$$\mathbf{N_{q,k}} = \mathrm{diag}\left(\frac{1}{\rho_{ADC}} \frac{1}{K} \sum_{k=1}^{K} (\mathbf{U_k H_k K_{x,k} H_k^* U_k^*} + \mathbf{U_k H_k K_{int,k} H_k^* U_k^*} + N_{th,k}\mathbf{U_k U_k^* I}_{N_r}) \right), \tag{6.15}$$

where $\mathbf{K_{int,k}} = \mathbb{E}[\mathbf{n_{int,k} n_{int,k}^*}]$ is the expected interference power matrix of size $N_t \times N_t$ of the k^{th} subcarrier. The throughput is defined for complex input signals. An ADC can only sample a real input signal. In a zero intermediate frequency (IF) architecture this is solved by using a quadrature ADC (Figure 5.3). Another commonly used method is to use an adequately large IF receiver and use an ADC which samples at, at least, twice the wide bandwidth of the input signals.

Independent Rayleigh Fading per Subcarrier

In the commonly used narrowband Rayleigh fading model, the SNR per receive antenna (when all transmit antennas transmit an equal amount of power), is defined as the sum of the received power of the desired user by all receive antennas, divided by the number of desired user transmit antennas and the power of the corresponding channel noise

$$\mathrm{SNR} = \frac{\sum_{k=k_1}^{k_K} \mathrm{Tr}[\mathbf{K}_{\mathbf{x},\mathbf{k}}]}{N_{td} \sum_{k=k_1}^{k_K} N_{th,k}}, \tag{6.16}$$

where $k_1, \ldots, k_K$ are the frequency components of the OFDM symbols of the desired user $\mathbf{x}$, where the channel noise components are defined as $N_{th,k} = \frac{1}{k_K - k_1} N_{th}$, with $N_{th} = k_b T B$, here T is the temperature, B is the bandwidth of the user, and Boltzmann's constant k_b equals $1.38 \cdot 10^{-23}$. Further, the interference to carrier ratio (ICR) of the i^{th} individual interferer is defined as

$$\mathrm{ICR} = \frac{\sum_{k=k_{i,1}}^{k_{i,K}} \mathrm{Tr}[\mathbf{K}_{\mathbf{int},\mathbf{k},\mathbf{i}}]}{N_{td} \sum_{k=k_1}^{K_K} \mathrm{Tr}[\mathbf{K}_{\mathbf{x},\mathbf{k}}]}, \tag{6.17}$$

where $k_{i,1}, \ldots, k_{i,K}$ are the frequency components of the OFDM symbols of $\mathbf{n}_{\mathbf{int},\mathbf{k},\mathbf{i}}$, were $\mathbf{K}_{\mathbf{int},\mathbf{k},\mathbf{i}} = \mathbb{E}[\mathbf{n}_{\mathbf{int},\mathbf{k},\mathbf{i}} \mathbf{n}^*_{\mathbf{int},\mathbf{k},\mathbf{i}}]$, and $\mathbf{n}_{\mathbf{int},\mathbf{k}} = \sum_{i=1}^{N_t - 1} \mathbf{n}_{\mathbf{int},\mathbf{k},\mathbf{i}}$.

Ray Tracer

The elements of the channel matrix $\mathbf{H}$ of the wideband channel model do not have a unit magnitude variance. To compare the wideband model with narrowband Rayleigh fading the SNR at each receive antenna is now defined as,

$$\mathrm{SNR} = \frac{N_r \sum_{k=k_1}^{k_K} \mathrm{Tr}[\mathbf{H}_\mathbf{k} \mathbf{K}_{\mathbf{x},\mathbf{k}} \mathbf{H}_\mathbf{k}^*]}{\sum_{k=k_1}^{k_K} N_{th,k}}, \tag{6.18}$$

here $k_1, \ldots, k_K$ are the frequency components of the OFDM symbols of $\mathbf{x}$, were the channel noise components are defined as $N_{th,k} = \frac{1}{k_K - k_1} N_{th}$, with $N_{th} = k_b T B$. In the wideband channel model, the interference to carrier ratio (ICR) of the i^{th}

individual interferer is defined as

$$\mathrm{ICR} = \frac{\sum_{k=k_{i,1}}^{k_{i,K}} \mathrm{Tr}[\mathbf{H_k K_{int,k,i} H_k^*}]}{\sum_{k=k_1}^{K_K} \mathrm{Tr}[\mathbf{H_k K_{x,k} H_k^*}]}, \tag{6.19}$$

here $k_{i,1}, \ldots, k_{i,K}$ are the frequency components of the OFDM symbols of $\mathbf{n_{int,k,i}}$, were $\mathbf{K_{int,k,i}} = \mathbb{E}[\mathbf{n_{int,k,i} n_{int,k,i}^*}]$, and $\mathbf{n_{int,k}} = \sum_{i=1}^{N_t-1} \mathbf{n_{int,k,i}}$.

6.3.2 Proposed Beamforming Algorithms

We have now defined the achievable throughput for a given receive matrix $\mathbf{U_k}$. In the SIMO beamforming case, $\mathbf{U_k}$ is a vector. We can use the achievable throughput to quantify the potential gain of spatial filtering in terms of bits/s/Hz, and use it to indicate the potential conversion bit reduction, and thus via (6.1) the potential power reduction of the ADC. In this section we will introduce two algorithms from [18], which strive to exploit the spatial correlation in a single-carrier signal, and the AOA information of an OFDM signal in combination with the wideband channel of Figure 6.1.

Single-Carrier Signal

Two scenarios are considered for the nonselective case. We model this as OFDM with a single subcarrier. The first scenario consists of adjacent channel interference, where each user has a single unique subcarrier. The second scenario consists of co-channel interference, where all N_t users have the same subcarrier. Further we assume that $N_r \geq N_t$. The current channel state vector of size $N_r \times 1$ per transmit antenna per subcarrier, between each transmit antenna and the N_r receive antennas is defined as $\mathbf{M}$. The $N_r \times N_t$ size channel matrix $\mathbf{H}$ is stacked by current channel state $\mathbf{M}$ vectors, for each transmitter, of size $N_r \times 1$ according to $\mathbf{H} = [\mathbf{M_1}, \mathbf{M_2}, \ldots, \mathbf{M_{N_t}}]$. Via a singular value decomposition (SVD) the Eigen values are derived. The SVD is given by $\mathbf{H} = \mathbf{U_H \Lambda_H V_H^*}$, here $\mathbf{U_H}$ and $\mathbf{V_H^*}$ are unitary matrices, and $\mathbf{\Lambda_H} = \mathrm{diag}(\lambda_1, \lambda_2, \ldots, \lambda_{N_r})$, were λ_k^2 is the k^{th} Eigen values of $\mathbf{HH}^*$. The matrix $\mathbf{U}_\mathbf{H}^*$ contains N_r conjugated Eigenvectors of size $1 \times N_r$, from these N_r vectors the vector that maximizes (6.14) is chosen for $\mathbf{U_k}$. The receiver array is now beamforming into the direction of the desired user, while nulling the other sources.

OFDM Signal

For the wideband channel of Figure 6.1 all OFDM subcarriers of $\mathbf{x}$ and $\mathbf{n_{int}}$ each have a unique frequency. The $N_r \times N_t$ size channel matrix $\mathbf{H}$ is stacked by current channel state $\mathbf{M}$ vectors, for each transmitter, of size $N_r \times 1$ according to $\mathbf{H} = [\mathbf{M_1}, \mathbf{M_2}, \ldots, \mathbf{M_{N_t}}]$. The aim is to find an appropriate setting for a common vector $\mathbf{U_k}$ across all frequency components such that the throughput T is maximized. Ideally, the spatial filter should preserve all the desired user information while simultaneously nulling the interferers. In reality however, there is a trade-off between these two requirements, and perfect nulling across the entire frequency range cannot be achieved by a common matrix setting. In order to find an appropriate setting for $\mathbf{U_k}$ we propose two different estimation algorithms. The first algorithm is comparable to maximum ratio combining, and primarily strives to maximize the SNR of the desired user. The second algorithm primarily strives to minimize the noise contribution of $\mathbf{N_q} = \sum_{k=1}^{K} \mathbf{N_{q,k}}$, which is a scalar in the beamforming case, by suppressing the interferers.

The first algorithm (WB Method 1) is a least squares algorithm which tries to maximize the power of the desired user and mitigate the power of the interfering users. The algorithm iteratively solves the equality

$$||\mathbf{AU} - \mathbf{b}||_2^2 = 0 \tag{6.20}$$

here $\mathbf{A}$ is a $K \times N_r$ size matrix containing the channel components of $1 \times N_r$ size transposed non zero channel vector $\mathbf{M_k}$ of each k^{th} frequency, $\mathbf{b}$ is a $K \times 1$ vector containing zeros on the frequency components of $\mathbf{n_{int}}$ and ones on the frequency components of $\mathbf{x}$, $\mathbf{U}$ is a complex $N_r \times 1$ size vector and its transpose is used as a common $\mathbf{U_k}$ in (6.14).

The second algorithm (WB Method 2) is a least squares algorithm which first estimates a channel vector $\mathbf{U_n}$ for each user. The channel matrix $\mathbf{H_k}$ can be expressed as a combination of channels of both the desired user channel vector $\mathbf{M_k}$ and interfering user channel vectors $\mathbf{M_{int,k,i}}$ were $\mathbf{H_k} = [\mathbf{M_{int,k,i}}, \ldots, \mathbf{M_{int,k,(N_t - N_{td})}}, \mathbf{M_k}]$, here $(N_t - 1)$ is the number of interfering users. Since the interferers and desired user each have a unique set of non zero frequencies we do an estimate per appropriate frequency set of the channels. To obtain a common desired user vector the algorithm iteratively solves

$$\| \sum_{k=k_1}^{k_K} (\mathbf{U_{N_t}} - \mathbf{M_k}) \|_2^2 = 0 \tag{6.21}$$

here $k_1, \ldots, k_K$ are the frequency components of the OFDM symbols of $\mathbf{x}$, $\mathbf{M_k}$ is the $N_r \times 1$ size channel vector of each k^{th} frequency, and $\mathbf{U_{N_t}}$ is a $N_r \times 1$ size vector containing the estimated common channel components. To map the i^{th} interfering user channel vector $\mathbf{M_{int,k,i}}$ to $\mathbf{U_i}$ the algorithm iteratively solves the equality

$$\| \sum_{k=k_{i,1}}^{k_{i,K}} (\mathbf{U_i} - \mathbf{M_{int,k,i}}) \|_2^2 = 0 \tag{6.22}$$

here $k_{i,1}, \ldots, k_{i,K}$ are the frequency components of the OFDM symbols of $\mathbf{n_{int,k,i}}$, $\mathbf{M_{int,k,i}}$ is the $N_r \times 1$ size channel vector of each k^{th} frequency, and $\mathbf{U_i}$ is a $N_r \times 1$ size vector containing the estimated common interferer channel components. The mapped channel vectors $\mathbf{U_k}$ are stacked in a matrix according to $\mathbf{M'} = [\mathbf{U_1}, \mathbf{U_2}, \ldots, \mathbf{U_{N_t}}]$. As in the single-carrier case, the Eigen values are derived via a singular value decomposition (SVD). The SVD is given by $\mathbf{M'} = \mathbf{U_{M'}} \mathbf{\Lambda_{M'}} \mathbf{V^*_{M'}}$, here $\mathbf{U_{M'}}$ and $\mathbf{V^*_{M'}}$ are unitary matrices, and $\mathbf{\Lambda_{M'}} = \mathrm{diag}(\lambda_1, \lambda_2, \ldots, \lambda_{N_r})$, were λ_k^2 is the k^{th} Eigen values of $\mathbf{M'M'^*}$. The matrix $\mathbf{U^*_{M'}}$ contains N_r conjugated Eigenvectors of size $1 \times N_r$, from these N_r vectors the vector that maximizes (6.14) is chosen for $\mathbf{U_k}$. The receiver array is now beamforming into the direction of the desired user, while nulling the other users.

6.3.3 Proposed Full MIMO Spatial Filter Algorithms

In the Full MIMO Spatial filter, the wideband input signal is processed in front of the ADCs via a single common analog matrix as depicted in Figure 5.4, and $\mathbf{x}$ and $\mathbf{n_{int}}$ are on separate frequencies. In the channel model of Figure 6.2, we assume a full rank MIMO system, $N_{td} = N_r$. Therefore, there is a larger number of transmit antennas than receive antennas (i.e., $N_t > N_r$) in the channel model. Since the channel matrix is rank deficient, it acts as a rank reduction matrix on the system. In the system depicted in Figure 5.4 the $N_r \times N_t$ channel matrix is processed in front of the ADCs via a smaller $N_r \times N_r$ matrix.

The aim is to find an appropriate setting for the common $N_r \times N_r$ matrix $\mathbf{U_k}$ across all frequency components such that the throughput T of (6.14) is maximized. In an appropriate setting for the common channel spatial filter matrix, each row of $\mathbf{U_k}$ should beamform in an independent direction such that $\mathbf{U_k}\mathbf{U_k^*} = \mathbf{cI}$ (here $\mathbf{c}$ is a non zero scalar), this in order to prevent correlation in (6.14). Correlation in (6.14) negatively impacts the throughput by decreasing the value of the determinant. Simultaneously, the AOAs of the interferers should be suppressed as such that the value of the components of $\mathbf{N_q} = \sum_{k=1}^{K} \mathbf{N_{q,k}}$, which is a diagonal matrix in the full MIMO case, in (6.14) is minimized.

Since the wideband channel matrix $\mathbf{H}$ is rank deficient and the received signal includes strong interference, standard estimation methods based on SVD are not applicable. An SVD on a rank deficient channel matrix yields fewer Eigenvalues than transmit antennas and the largest Eigenvalues will correspond to the interferers. Therefore, we propose a new approach to find a setting for the common matrix $\mathbf{U_k}$. In the first step we map the channel matrices of the separate OFDM symbols on a common channel matrix for all frequencies. In the second step we will use the mapped common channel matrix to estimate a common matrix setting of $\mathbf{U_k}$ across all frequency components. The algorithm primarily strives to minimize the noise contribution of the components of diagonal matrix $\mathbf{N_q}$ by suppressing the interferers.

For the mapping we estimate a common channel matrix $\mathbf{H'}$ from all $\mathbf{H_k}$ channels.

The channel matrix $\mathbf{H_k}$ can be expressed as a combination of channels of both the desired user channel matrix $\mathbf{M_k}$ and interfering user channel vectors $\mathbf{M_{int,k,i}}$ were $\mathbf{H_k} = [\mathbf{M_{int,k,i}}, \ldots, \mathbf{M_{int,k,(N_t-N_{td})}}, \mathbf{M_k}]$, here $(N_t - N_{td})$ is the number of interfering users. Since the interferers and desired user each have a disjoint set of non zero frequencies the mapping to a common channel across all frequencies per user is only performed per appropriate non zero frequency set of the channels. To map the desired user channel matrix $\mathbf{M_k}$ to $\mathbf{M}'$ the algorithm iteratively solves the equality

$$\| \sum_{k=k_1}^{k_K} (\mathbf{M}' - \mathbf{M_k}) \|_2^2 = 0 \tag{6.23}$$

here $k_1, \ldots, k_K$ are the frequency components of the OFDM symbols of $\mathbf{x}$, $\mathbf{M_k}$ is the $N_r \times N_{td}$ size channel matrix of each k^{th} frequency, and $\mathbf{M}'$ is a $N_r \times N_{td}$ size matrix containing the estimated common channel components. To map the i^{th} interfering user channel vector $\mathbf{M_{int,k,i}}$ to $\mathbf{M}'_{\mathbf{int,i}}$ the algorithm iteratively solves the equality

$$\| \sum_{k=k_{i,1}}^{k_{i,K}} \left(\mathbf{M}'_{\mathbf{int,i}} - \mathbf{M_{int,k,i}}\right) \|_2^2 = 0 \tag{6.24}$$

here $k_{i,1}, \ldots, k_{i,K}$ are the frequency components of the OFDM symbols of $\mathbf{n_{int,k,i}}$, $\mathbf{M_{int,k,i}}$ is the $N_r \times 1$ size channel vector of each k^{th} frequency, and $\mathbf{M}'_{\mathbf{int,i}}$ is a $N_r \times 1$ size matrix containing the estimated common interferer channel components.

The spatial filter should minimize the components of diagonal matrix $\mathbf{N_q}$ in (6.14), while preserving the desired user information. To find an appropriate setting for $\mathbf{U_k}$, first each Eigenvalue vector of $\mathbf{M}'$ is combined with the AOAs of the interferers to form separate matrices. On each resulting matrix an SVD is performed to find a $1 \times N_r$ sized row vector for each row of $N_r \times N_r$ sized spatial filter matrix $\mathbf{U_k}$ as such that each row vector of matrix $\mathbf{U_k}$ beamforms towards a separate Eigenvalue vector of the common desired user channel state matrix $\mathbf{M}'$ while nulling the AOAs of common channel state vectors $\mathbf{M}'_{\mathbf{int,i}}$ of each interferer.

To find the common AOAs of $\mathbf{M}$ that contain most of the desired user power (which we want to preserve in the setting of the common spatial filter matrix $\mathbf{U_k}$) we search for the common Eigenvalue vectors corresponding to $\mathbf{M}'$. The Eigenvalue vectors of $\mathbf{M}'$ are obtained via an SVD. The SVD is given by $\mathbf{M}' = \mathbf{U_{M'}}\mathbf{\Lambda_{M'}}\mathbf{V}^*_{\mathbf{M'}}$, here $\mathbf{U_{M'}}$ and $\mathbf{V^*_{M'}}$ are unitary matrices, and $\mathbf{\Lambda_{M'}} = \text{diag}(\lambda_1, \lambda_2, \ldots, \lambda_{N_r})$, were λ_k^2 is the k^{th} Eigenvalues of $\mathbf{M'M'^*}$. From $\mathbf{U_{M'}}$, every column is taken and set in a separate vector $\mathbf{U_{M',m}}$, as such that $\mathbf{U_{M'}} = [\mathbf{U_{M',1}}, \ldots, \mathbf{U_{M',N_r}}]$. The vectors $\mathbf{U_{M',m}}$ now correspond to the dominant AOAs at the receiver of the Eigenvalues of $\mathbf{M'}$.

Now that the Eigenvalue vectors of $\mathbf{M'}$ are found, these are combined with the AOAs of $\mathbf{M'_{int,i}}$ of each interferer to find a setting for $\mathbf{U_k}$ that maximizes (6.14). In this maximum, the receiver beamforms towards the Eigenvalue vectors of $\mathbf{M'}$ while nulling the AOAs of $\mathbf{M'_{int,i}}$ of each interferer. Under the constraint that $(N_t - N_{td}) < N_r$, each vector $\mathbf{U_{M',m}}$ is stacked in a matrix $\mathbf{Q_m}$ with the common interferer channel vectors such that $\mathbf{Q_m} = [\mathbf{M'_{int,i}}, \ldots, \mathbf{M'_{int,(N_t-N_{td})}}, \mathbf{U_{M',m}}]$. We now take an SVD of $\mathbf{Q_m}$. The SVD is given by $\mathbf{Q_m} = \mathbf{U_{Q,m}\Lambda_{Q,m}V^*_{Q,m}}$, here $\mathbf{U_{Q,m}}$ and $\mathbf{V^*_{Q,m}}$ are unitary matrices, and $\mathbf{\Lambda_{Q,m}} = \text{diag}(\lambda_1, \lambda_2, \ldots, \lambda_{N_r})$, were λ_k^2 is the k^{th} Eigenvalues of $\mathbf{Q'_m Q'^*_m}$. There are N_r matrices $\mathbf{U_{Q,m}}$ of size $N_r \times N_r$ containing N_r Eigenvectors $\mathbf{U_{Q,d,m}}$ of size $N_r \times 1$. The total number of N_r^2 vectors $\mathbf{U_{Q,d,m}}$ are stacked in $N_r^{N_r}$ unique matrices $\mathbf{U_t}$ of the form $\mathbf{U_t} = [\mathbf{U_{Q,d,1}}, \ldots, \mathbf{U_{Q,d,N_r}}]$. From the $N_r^{N_r}$ unique matrices $\mathbf{U_t}$ the matrix $\mathbf{U^*_t}$ that maximizes (6.14) is chosen for $\mathbf{U_k}$. The resulting matrix setting now nulls the interferers, while beaming into the Eigenvalues of the desired user. Nulling the interference is a good strategy when the number of ADC steps is small. When more steps are available in the ADC a compromise between interference suppression and maximum ratio combining is needed.

6.4 Numerical Results

In this Section we start by simulating the vector beamforming architecture of Figure 5.3 in combination with single-carrier signals and a Rayleigh fading channel example. Secondly we use OFDM signals and the wideband channel model of Figure 6.1 to show the potential benefit of spatial filtering in a wideband regime and to quantify the potential gain in terms of ADC power reduction and ADC bits. Then, we extend the simulation to show the effect of the RMS delay spread

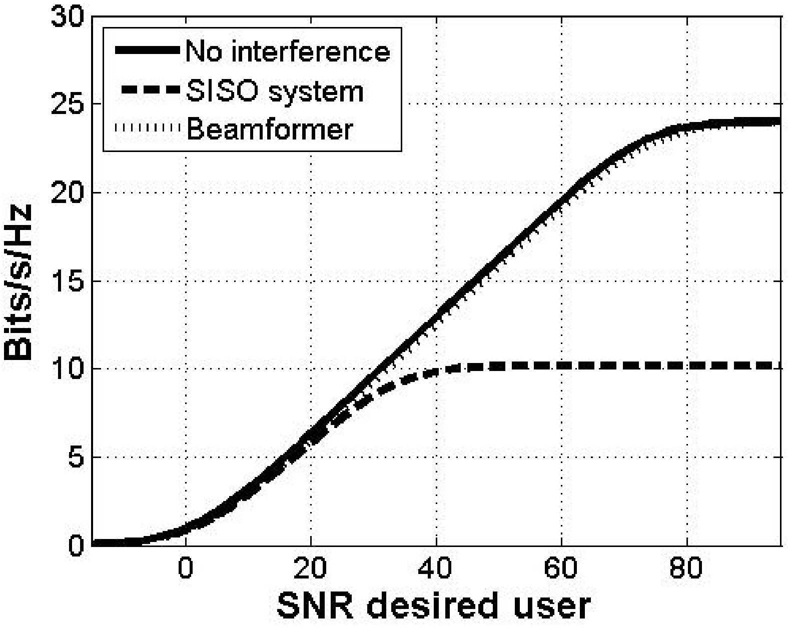

Figure 6.3: *Throughput of beamformer compared to a SISO system, for a Rayleigh fading channel model and single carrier signals (all signals are flat fading), for two 12 bit ADCs in the I and Q path. Single-carrier signals. ICR of co-channel interferer one is 40 dB and of co-channel interferer two is 30 dB.*

and the finite resolution of the coefficients of the beamformer. Finally we simulate the architecture of Figure 5.4 in combination with the wideband channel model of Figure 6.2 to show the benefits of combining full MIMO spatial filtering while still allowing for all MIMO data streams.

6.4.1 Beamforming Flat Fading

We start with an example of the co-channel interference case. We assume $N_t = 3$, $N_r = 3$, the ADCs have 12 bits, and the ICR = 40dB for interferer 1 and ICR = 30dB for interferer 2. Since our receiver has two ADCs, one in the I-path and one in the Q-path, the combined resolution is 24 bits per sample. Figure 6.3 and 6.4 depict the results averaged over 100 Monte Carlo simulations. As can be seen in the graphs, beamforming in the direction of the eigenvector corresponding to the eigenvalue of the desired user, yields a result which is close to the interference free

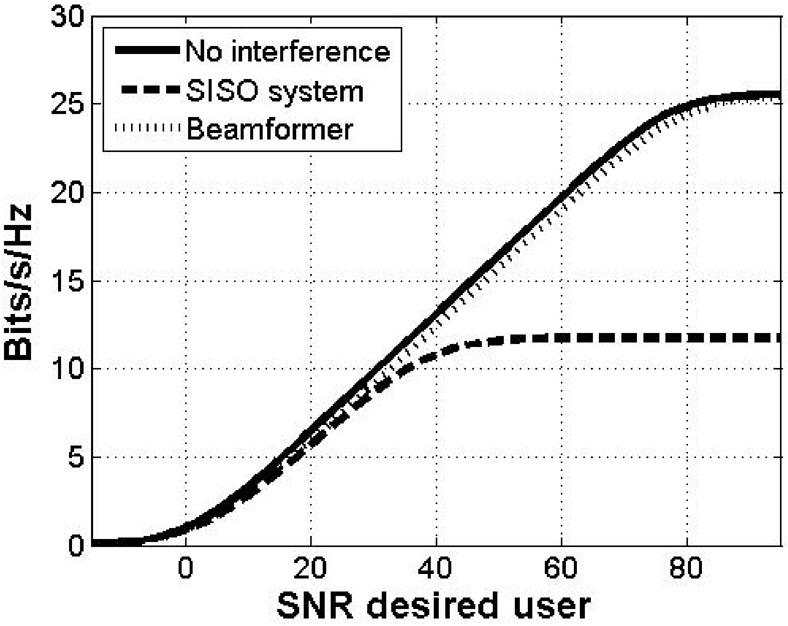

Figure 6.4: *Throughput of beamformer compared to a SISO system, for a Rayleigh fading channel model and single carrier signals (all signals are flat fading). For two 12 bit ADCs in the I and Q path. Single-carrier signals. ICR of adjacent channel interferer one is 40 dB and of adjacent channel interferer two is 30 dB.*

case. Figure 6.4 depicts the results of the adjacent channel interferer simulations. Here the interferers are on adjacent OFDM subcarriers, but still in band for the CR ADC. Therefore, the ADC is required to sample at three times the rate as in the co-channel case. The desired user can benefit from the over sampling ratio and achieve a higher throughput. The throughput for the desired user can be above 24 bits/s/Hz, because the quantization noise is spread over more subcarriers than are used by the desired user.

6.4.2 Beamforming OFDM Signals

Now we will analyze our algorithms over several examples of the wideband channel. First we will present results of the proposed algorithms for various SNR, secondly the ICR is varied, and finally the number of bits of the individual ADCs is swept.

Impact of SNR

We assume $N_t = 3$, $N_r = 3$, the ADC has 8 bits, and the ICR = 40dB for interferer 1, ICR = 30dB for interferer 2. Each user has 20 OFDM subcarriers, of which the 2 on either side of the spectrum contain zeros and the 16 OFDM subcarriers in the middle contain OFDM data symbols. The zeros are included to mimic the channel separation that is common in standards such as IEEE 802.11 and needed to satisfy the spectral mask (in IEEE 802.11 between commonly used non overlapping channels 1, 6, and 11). The carrier frequency is 2.45 GHz, the bandwidth $B = 5$ MHz per user, $\sigma_n = 10$ m, $\sigma_{n,p} = 5$ m, $\sigma_m = 10$ m, $c = 3 \cdot 10^8$ m/s, T = 295 K, and the number of multipaths $P = 5$, including a LOS. Figure 6.5 depicts the results for an 8 bit ADC, and Figure 6.6 for a 12 bit ADC per I and Q path for 100 Monte Carlo simulations. As can be seen in Figures 6.5 and 6.6, WB method 2 outperforms WB method 1, and vastly improves the throughput at higher SNR, when compared to the SISO case, up to 8 bits/s/Hz. At lower SNR WB method 1 outperforms WB method 2 and the SISO case, and is close to the interference free scenario, improving the throughput with up to 2 bits/s/Hz. WB method 1 performs well when thermal noise is dominant, because it mainly beamforms in the

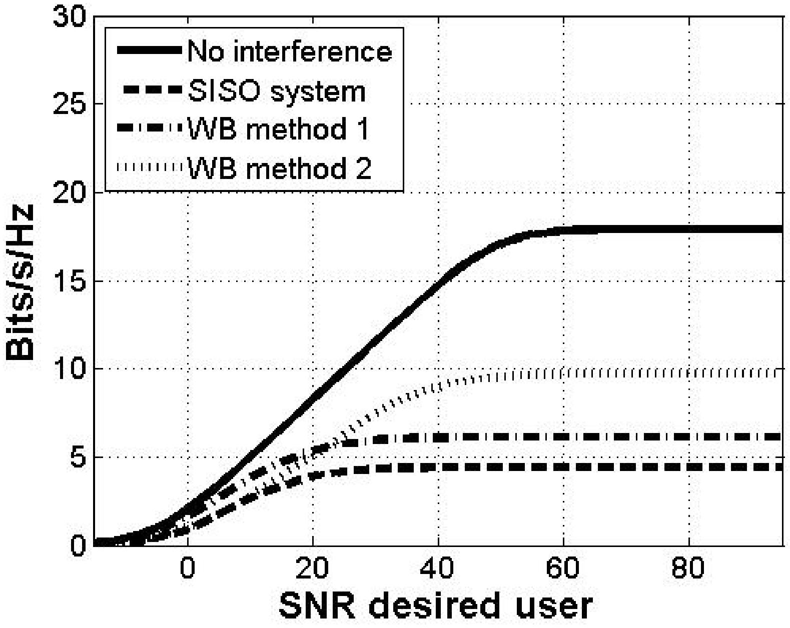

Figure 6.5: *OFDM signals and wideband ray tracing channel model (all signals are frequency selective). Throughput of beamformer compared to a SISO system. For two 8 bit ADCs in the I and Q path. ICR of interferer one is 40 dB and of interferer two is 30 dB.*

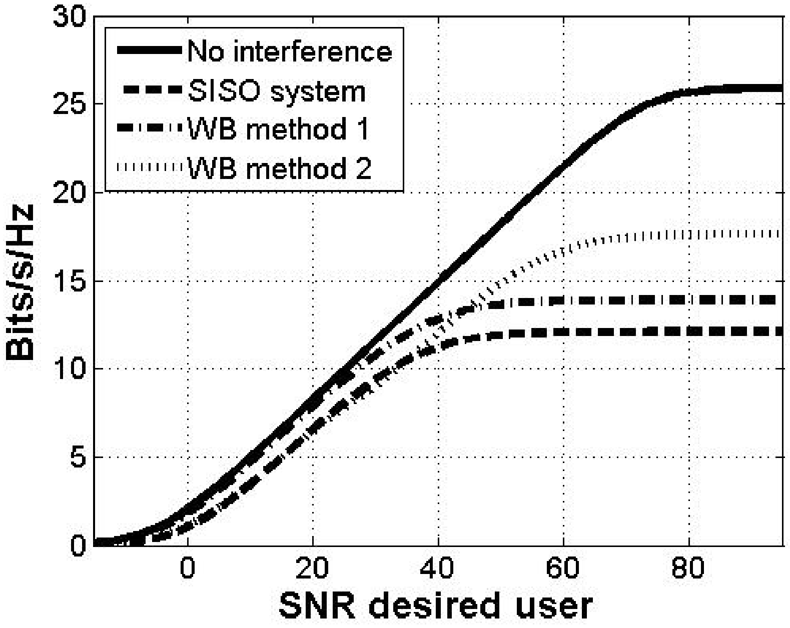

Figure 6.6: *OFDM signals and wideband ray tracing channel model (all signals are frequency selective). Throughput of beamformer compared to a SISO system. For two 12 bit ADCs in the I and Q path. ICR of interferer one is 40 dB and of interferer two is 30 dB.*

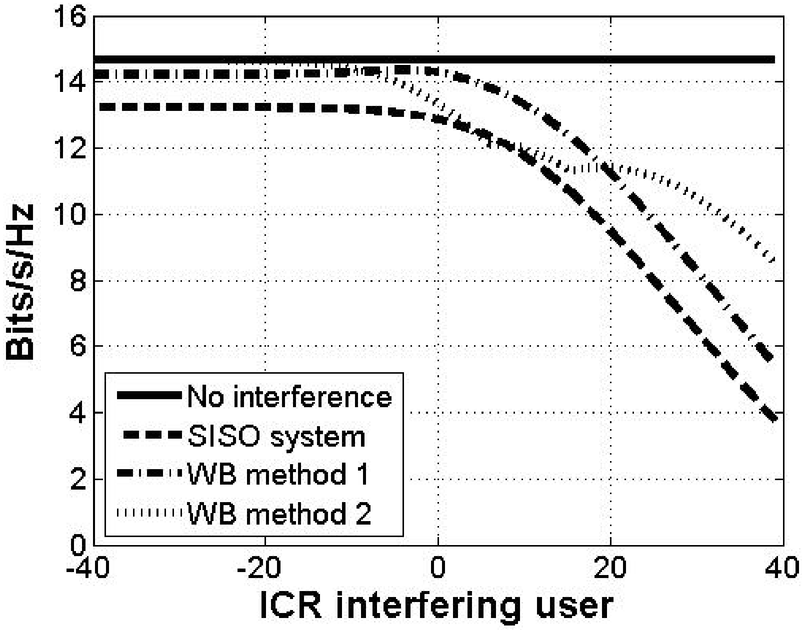

Figure 6.7: *OFDM signals and wideband ray tracing channel model (all signals are frequency selective). Throughput of beamformer compared to a SISO system. For two 8 bit ADC in the I and Q path and SNR=* $40dB$*.*

direction of the desired user, which increases the SNR and thus throughput. WB method 2 is a good strategy in the quantization noise limited regime, because it emphasizes interference suppression above beamforming towards the desired user. Decreasing the power of the interferers in the quantization noise limited regime, results in more ADC resolution for the desired user, and thus a higher throughput.

Impact of ICR

We will now vary the ICR and assume that both interferers have an equal ICR. Further, we assume the SNR = 40 dB, and the ADCs each have 8 bits. Figure 6.7 shows the results for 100 Monte Carlo simulations. In Figure 6.7 it can be seen that relatively small ICR, low interference levels, can be prohibitive even at large SNR. Furthermore, analog beamforming has the potential to improve the throughput both in the presence of small and large interferers, when compared to a SISO system.

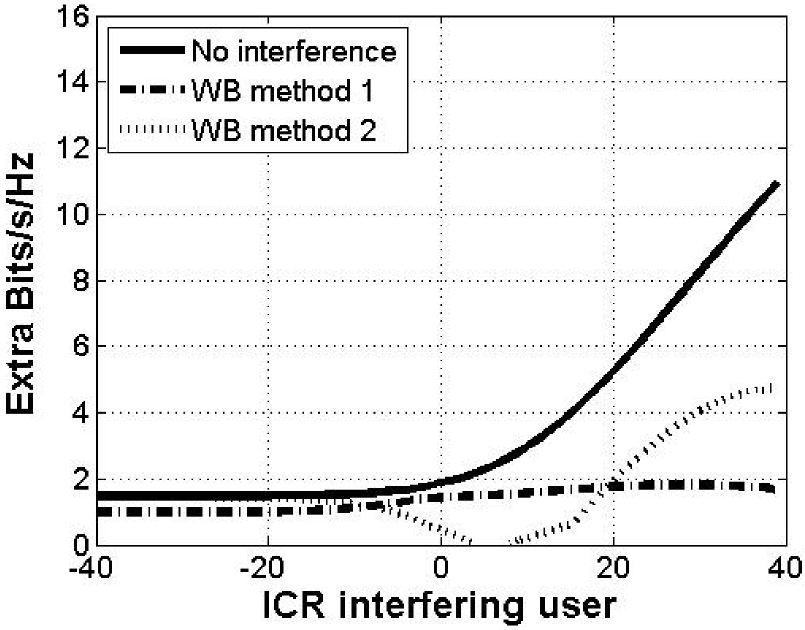

Figure 6.8: *OFDM signals and wideband ray tracing channel model (all signals are frequency selective). Difference in Throughput of beamformer compared to a SISO system. For two 8 bit ADC in the I and Q path and SNR=* $40dB$.

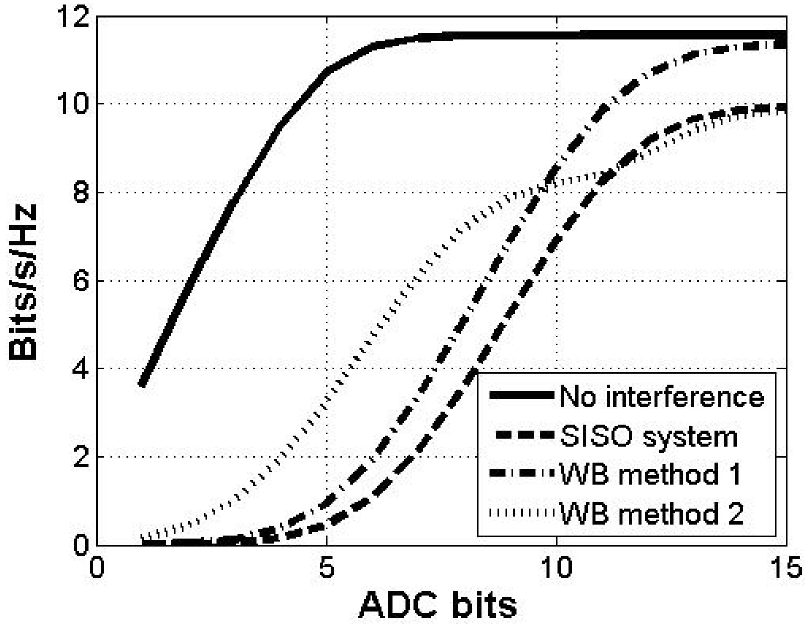

Figure 6.9: *OFDM signals and wideband ray tracing channel model (all signals are frequency selective). Throughput of beamformer compared to a SISO system. For two 8 bit ADC in the I and Q path and two interferers with ICR=* $40dB$ *and SNR=* $30dB$.

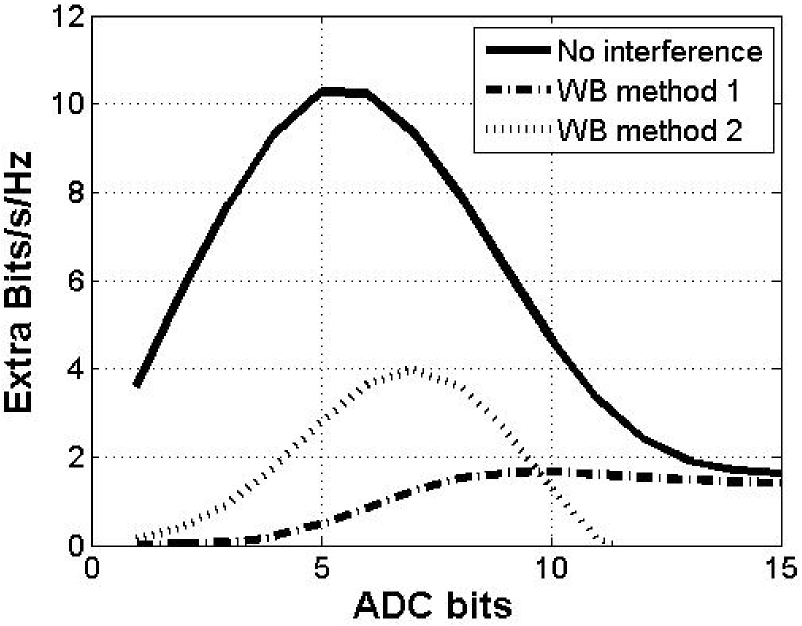

Figure 6.10: *OFDM signals and wideband ray tracing channel model (all signals are frequency selective). Difference in Throughput of beamformer compared to a SISO system. For two 8 bit ADC in the I and Q path and two interferers with ICR=* $40dB$ *and SNR=* $30dB$*.*

Table 6.1: *SNR versus number of bits required to achieve a given throughput in the beamformer case $T = 2$ bits/s/Hz. OFDM signals and wideband ray tracing channel model (wanted signal is frequency selective and interferers are flat fading).*

SNR [dB]	**Analog Array** [bits]	**SISO** [bits]	**Difference** [bits]
10	5.0	7.5	2.5
20	3.1	7.1	4.0
30	2.4	6.8	4.4
40	2.4	6.7	4.3

Impact of Number of ADC Bits

Compared to the previous section we will now vary the number of ADC bits and assume both the I and Q ADC have an equal number of bits. Further, we assume the ICR = 40 dB for interferer 1 and 2. Figure 6.8 shows that the throughput gain compared to a SISO system is largest in a quantization noise limited scenario. From Figure 6.9 we can derive that at a throughput of 2 bits/s/Hz, an analog spatial filtering system can equal a SISO system with 3 bits per ADC less. Since we assume a large ICR of 40 dB we consider it reasonable to assume the interference is in close proximity to the receiver. Therefore the delay spread of the interferer will be much smaller than that of the desired user. To take this into account, the significant multipaths for the interferers are set to two and for the desired user to five in (6.10). Results are shown in Table 6.1. This result is significant since this indicates that the power savings for the ADC can potentially be an order of magnitude. Since the power of ADC converters reduces with approximately 90% every decade, analog spatial filtering has the potential to accelerate the reduction of overall system power reduction.

Impact of Finite Resolution Phase Shifters

Up until now we have considered the phase shifters to have floating point precision. In practical systems the analog phase shifters have discrete steps. A common implementation of a phase shifter is a VGA in the I and a VGA in the Q path. We realized an IC implementation in [72], where an RF polyphase filter after the

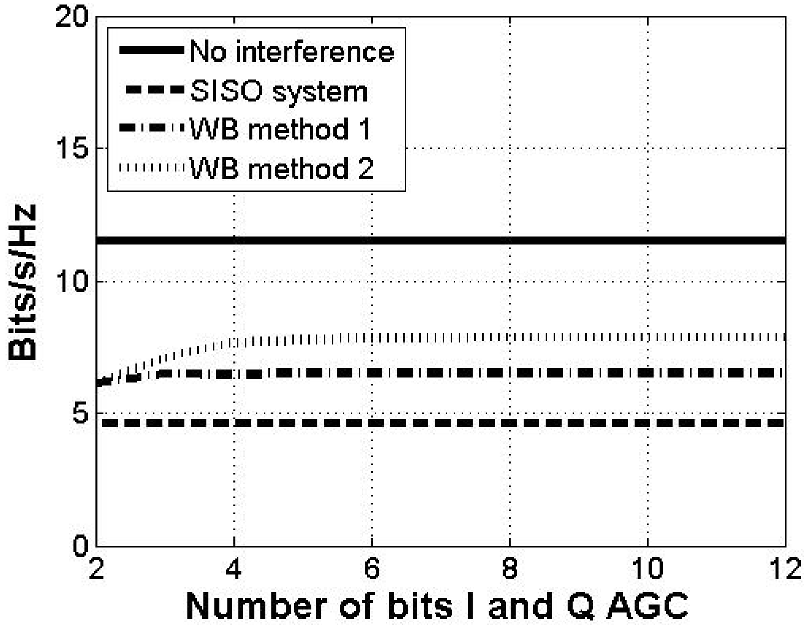

Figure 6.11: *OFDM signals and wideband ray tracing channel model (all signals are frequency selective). Throughput of beamformer compared to a SISO system for different amount of bits per RF phase shifter VGA in the RF I and Q path. For two 8 bit BB ADCs in the BB I and Q receiver path. SNR is 30 dB and the ICR of interferer one is 40 dB and of interferer two is 30 dB.*

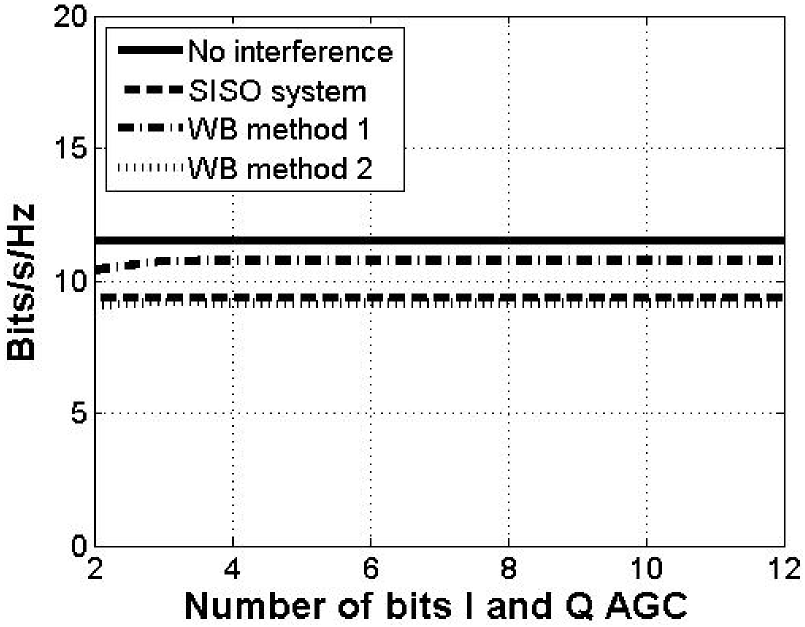

Figure 6.12: *OFDM signals and wideband ray tracing channel model (all signals are frequency selective). Throughput of beamformer compared to a SISO system for different amount of bits per RF phase shifter VGA in the RF I and Q path. For two 12 bit BB ADCs in the BB I and Q receiver path. SNR is 30 dB and the ICR of interferer one is 40 dB and of interferer two is 30 dB.*

LNA which splits the RF signal in an I and a Q path. These are each followed by a VGA and than added at RF before down converting. Figures 6.11 and 6.12 depict the effect of a different resolution per I and Q VGA for an SNR of 30 dB and two interferers with ICR = 40 dB and SNR = 30 dB. The effect of the resolution of the phase shifters on the throughput depends on the number of ADC levels in the baseband receiver chain. If there are ample levels in the baseband ADC, the phase shifter does not need to be accurate. On the other hand, if we want to reduce baseband ADC power consumption, and thus the amount of levels, the phase shifters require a higher resolution. Figures 6.11 and 6.12 depict the effects of the phase shifter accuracy when the baseband ADC in the I and Q path has 8 bits , and 12 bits, respectively. As can be seen in these figures, the impact of phase shifter accuracy is higher when the number of levels in the baseband ADC is smaller. Furthermore, we can conclude from Figures 6.11 and 6.12 that for our channel parameters, an AGC accuracy of above 5 bits results in a negligible improvement of the average throughput for a vector beamformer.

Impact of RMS Delay Spread

The number of multipaths per transmitter has been set to 5 in the simulations of Figure 6.9. We experimented with up to 500 reflections, but the impact on the throughput appeared to be minimal. This is because the scattering of the channel is rich enough with 5 multipaths per transmitter for the number of receive antennas that we consider in the simulations. A more important impact on throughput is due to the RMS delay spread and the corresponding coherence bandwidth as is depicted in Figure 6.13. At sufficiently large RMS delay spread, say $\tau_{\mathrm{RMS}} > 4\mu$s in Figure 6.13 the coherence bandwidth is in the order of a single frequency bin. Even at these small coherence bandwidths the spatial filter appears to still provide a significant gain. This result may be counter intuitive, as one might expect that a common, i.e. channel average, spatial filter setting for seemingly i.i.d. random frequency bins would have no significant effect. Our observation that spatial filtering is nonetheless effective can be explained because the system can still exploit the non uniformity of the angular spread if dominant signals arrive from particular angles. Moreover, although the correlation of all channel realizations between

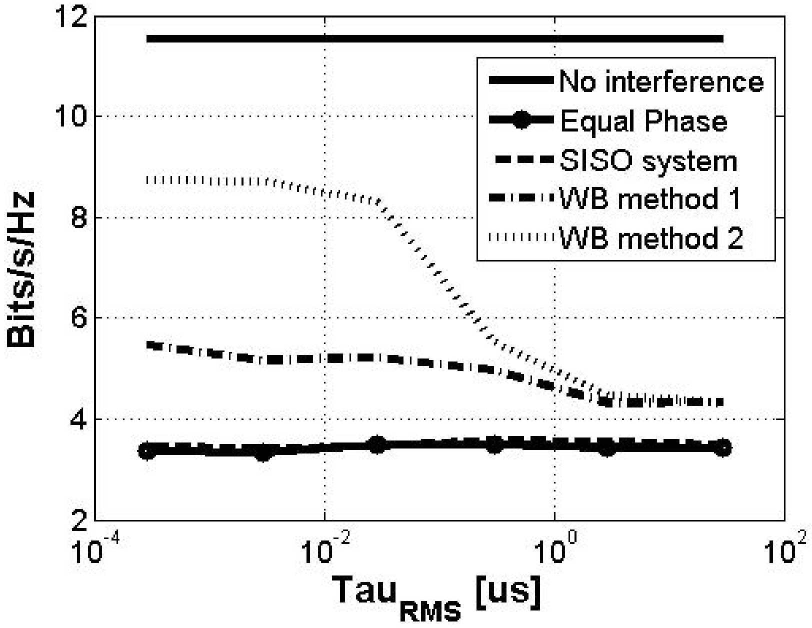

Figure 6.13: *OFDM signals and wideband ray tracing channel model (all signals are frequency selective). Effect of changing delay spread on throughput for 400 reflective surfaces, SNR is 30 dB. For two 8 bit ADCs in the I and Q path. ICR of interferer one is 40 dB and of interferer two is 30 dB.*

frequency bins will approach zero at large RMS delay spread, the instantaneous signal correlation for a specific channel realization is not necessarily zero, in which case it can be exploited by the spatial filter.

Although our focus here is primarily on indoor environments, spatial filtering can also be effective in other propagation environments. In the IEEE 802.22 standard, which is primarily designed for low populated rural areas [86], most primary users, such as TV broadcasters and FM radio stations, which interfere with the secondary CR tend to have a small RMS delay spread and a small AOA spread [87].

6.4.3 Full MIMO Spatial Filtering Wideband Channel

Now we will give several examples of the full MIMO case. In the full MIMO case, the ACMM performs spatial filtering while allowing for all data streams. For simulations we will use the channel model depicted in Figure 6.2.

Impact of Number of ADC Bits

We will now vary the number of ADC bits and assume both the I and Q ADC have an equal number of bits. Since we assume a large ICR of 40 dB we consider it reasonable to assume the interference is in close proximity to the receiver. Therefore the delay spread of the interferer will be much smaller than that of the desired user. To account for this effect, we assume that in the MIMO wideband channel model there are 2 reflections per interferer and 40 reflection for the desired user. Figures 6.14 and 6.15 show that the throughput gain compared to a regular MIMO system is largest in a quantization noise limited scenario. In Table 6.2 it can be seen that the difference between the ACMM and regular MIMO is smaller at lower SNR values. This is because our algorithm is trying to null the interferers, at lower SNR values it may be more effective to focus more on maximum ratio combining than nulling. From Figures 6.14 and 6.15 we can derive that at a throughput of 5 bits/s/Hz, an analog spatial filtering system can equal a 4×4 MIMO system with 3 bits per ADC less (Table 6.2). We believe this result is significant since

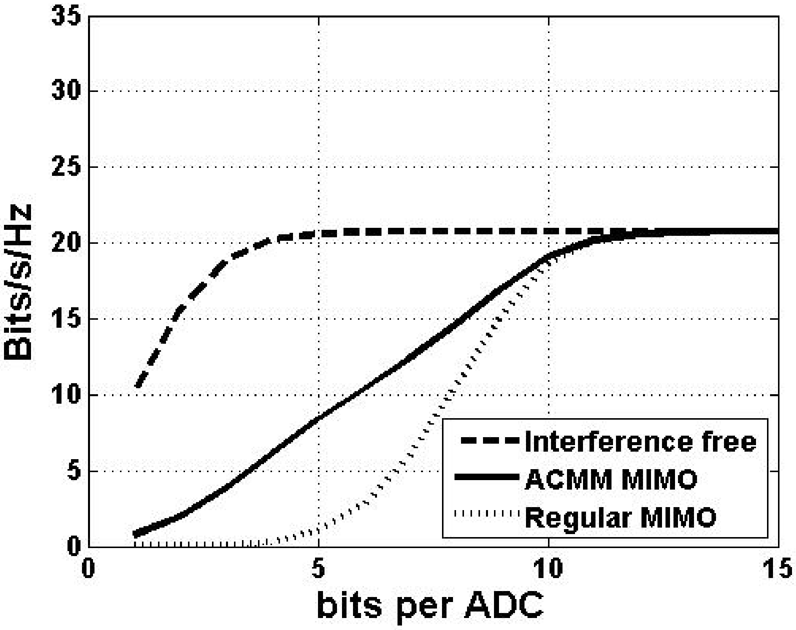

Figure 6.14: *OFDM signals and wideband ray tracing channel model (wanted signal is frequency selective and interferers are flat fading). Throughput of ACMM-MIMO compared to a regular and interference free MIMO system at SNR is 20dB, for a 4×4 MIMO system. Two interferers at ICR = 40 dB.*

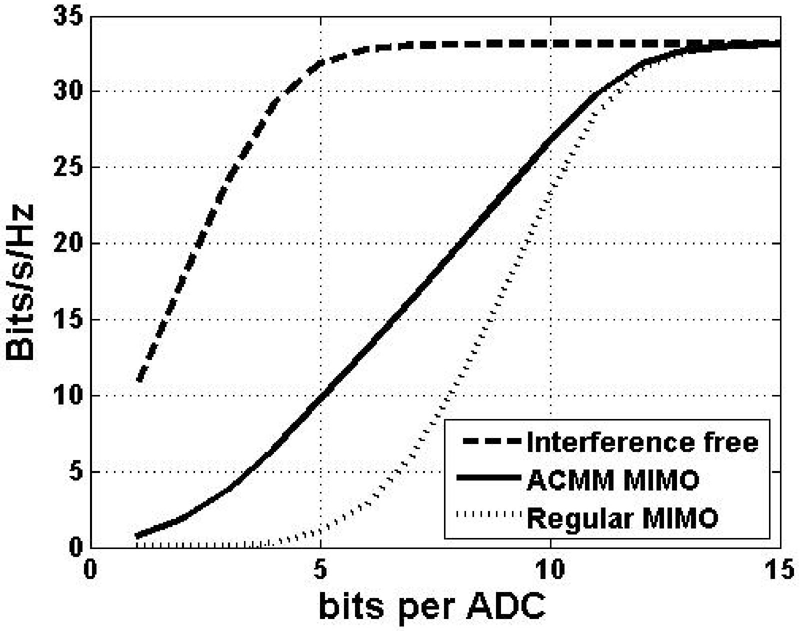

Figure 6.15: *OFDM signals and wideband ray tracing channel model (wanted signal is frequency selective and interferers are flat fading). Throughput of ACMM-MIMO compared to a regular and interference free MIMO system at SNR is 30 dB, for a 4×4 MIMO system. Two interferers at ICR = 40 dB.*

Table 6.2: *SNR versus number of bits required to achieve a given throughput for a* 4×4 *MIMO system in the full MIMO spatial filtering case* $T = 5$ *bits/s/Hz. OFDM signals and wideband ray tracing channel model (wanted signal is frequency selective and interferers are flat fading).*

SNR [dB]	**ACMM MIMO** [bits]	**Regular MIMO** [bits]	**Difference** [bits]
10	4.9	6.9	2.0
20	3.5	6.7	3.2
30	3.4	6.7	3.3
40	3.3	6.6	3.3

this indicates that the power consumption of the MIMO ADCs can potentially be reduced with over 85%. Therefore, full MIMO analog spatial filtering has the potential to accelerate the overall system power consumption reduction.

Comparing Full MIMO Spatial Filtering to Beamforming

In Figure 6.16 a 4×4 full MIMO spatial filter is compared to a 4×1 beamformer. We assume that in the MIMO wideband channel model there are 2 reflections per interferer and 40 reflection for the desired user. The figure shows that at low ADC bits, when the quantization noise is dominant, the beamformer and ACMM have a comparable performance. However, at higher ADC bits the MIMO receiver clearly outperforms the beamformer. The performance is comparable at low ADC bits because the quantization noise is so dominant that only the strongest Eigen value contributes to the throughput. Since the beamfomer focuses mainly on the strongest Eigen value its performance is similar to the ACMM, but with 3 ADCs less. From this example it can be seen that at channel realizations were there is a large variation in the dynamic range of the Eigen values, it is beneficial to switch off branches in the ACMM opportunistically to safe power, since they do not contribute to the overall system throughput. The empirical distribution function of the eigenvalues of Wishart matrices has an asymptotic distribution. This implies a large condition number and thus often leads to a large difference in the dynamic range of the eigenvalues for a given channel state. After evaluating the eigenvalue distribution of the channel, the signal to thermal and quantization noise ratio at the receiver can be used by the receiver as a measure to decide to switch on and off branches. Another option is to dynamically allocate the total amount of quantization levels in the receiver across the ADCs to further minimize the quantization noise contribution. This may allow for a reduction in the total amount of levels used and thus in the total ADC requirements.

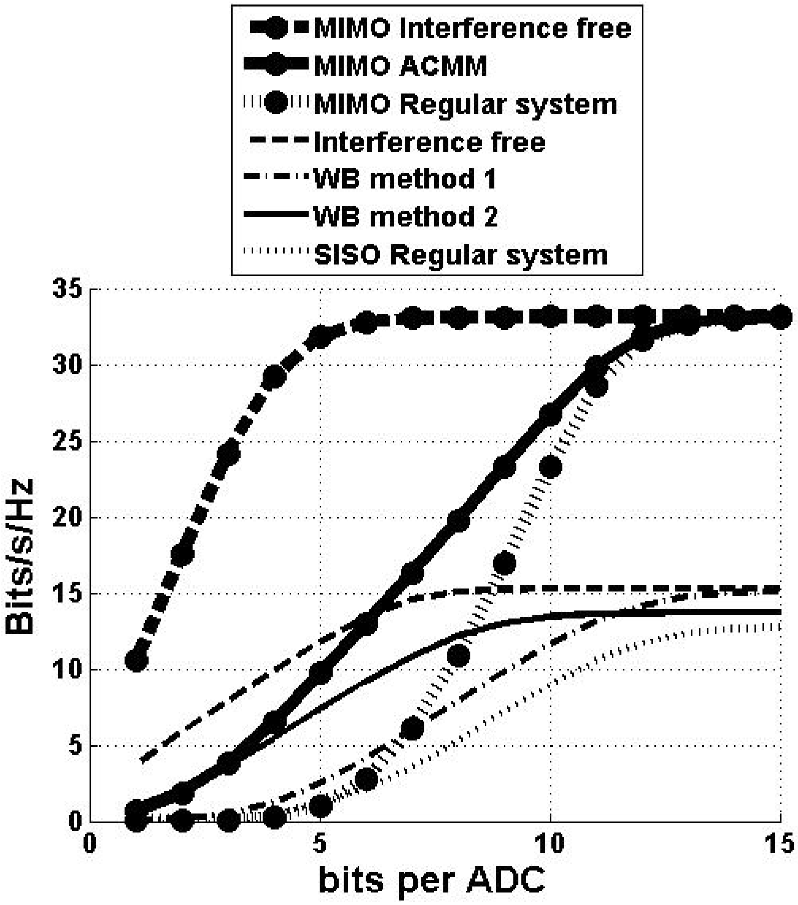

Figure 6.16: *Throughput of beamformer and ACMM-MIMO compared to a regular and interference free SISO and MIMO system at SNR is 30 dB, for a 4×4 MIMO system and* 4 *Rx Beamformer. OFDM signals and wideband ray tracing channel model (wanted signal is frequency selective and interferers are flat fading). Two interferers at ICR = 40 dB.*

6.5 Conclusions

In wideband cognitive radio (CR), analog spatial filtering can achieve similar system throughput as systems without spatial filtering with significantly less quantization bits in the baseband ADC. Simulations show that for realistic indoor scenarios with an SNR of 20 dB and two interferers with an ICR of 40 dB, a receiver using analog vector beamforming spatial filtering can achieve similar throughput compared to SISO with 4 ADC bits less, corresponding to a power reduction of over 90%. Further, simulations indicate that a MIMO system with an analog complex matrix multiplier that allows for full MIMO spatial filtering can achieve a similar throughput as a regular MIMO system with 3 ADC bit less, corresponding to a power reduction of over 85%. Opportunistic on and off switching of branches in the ACMM given a large variety in the dynamic range of the Eigen values of the current channel state and under low SNR can contribute to further power reduction. Another option is to dynamically allocate quantization levels among branches to further minimize the quantization noise contributed by the ADCs and thus their requirements. Since ADC power consumption reduces at a rate of an order of magnitude per decade, we believe that the algorithms and architectures for spatial filtering we proposed in this chapter, and submitted to [88], can largely contribute to overall system power reduction, and accelerate the introduction of CR in the handheld market.

Chapter 7

Conclusions and Recommendations

7.1 Conclusions

Most wireless devices such as laptops and mobile phones are battery powered. To extend battery lifetime the power consumption of the wireless transceivers needs to be reduced. Currently, we observe two opposing trends in new generations of mobile phones. Despite the ongoing miniaturization of existing functionality and its corresponding power reduction in handheld devices, the vast increase in number of applications and the subsequent demands on hardware in new generations of smart phones has offset and for now halted the overall trend of weight and size reduction of mobile phones. Furthermore, the available battery energy in smart phones has remained constant over time. Each battery power density improvement has resulted in a shrinking phone to appeal to consumers. With the addition of new functionalities, the power budget of existing wireless transceivers is still reducing. The current rate of power reduction of the RF front end and ADC is one order of magnitude per decade.

To increase the data rate of new wireless devices more new standard are using

MIMO techniques, such as LTE advance for mobile phones and IEEE 802.11n for WLAN. Because MIMO systems require multiple transceiver front ends and ADCs they consume more power and alone can drain a smart phone battery in under 4 hours. Therefore, reducing MIMO power consumption in handheld devices is of prime importance to increase battery lifetime.

Due to an increase in the number of users, the amount of interference is increasing. To cope with the rise in interference, new generations of mobile devices have to comply with more stringent requirements. The more stringent requirements come at a cost of increased power consumption. In Chapter 2 it is shown that the RF front end and ADC power consumption are the future bottlenecks in terms of extending battery lifetime. Mitigating the interferers and thus the dynamic range requirements of the RF front end and ADC has the potential to vastly reduce the power consumption of the ADC and RF front end.

The closed form solution we presented in Chapter 4 allows us to formalize the relation between interference power and achievable throughput for a given available receiver circuit power budget. Importantly, with the closed form solution we can show that a 20 dB reduction in CIR requirements results in a 30 dB reduction in receiver circuit power consumption. This means that a little interference suppression can already substantially reduce the required power budget. Another interesting result of the closed form solution in Chapter 4 is that for large SNR the optimal throughput per unit of receiver circuit power is 2.3 bits/s/Hz, irrespective of interference power level. Interestingly this limit is also independent of the used IC technology. However, the optimum power efficiency for lower SNR values does depend on IC technology. Furthermore, it can be shown that a duty cycling strategy at low power consumption level can result in a higher average system throughput than a continuously operating receiver consuming a similar time averaged power.

In Chapter 5 a novel ACMM building block that can suppress interference in the MIMO analog front ends, to alleviate the DR requirements of the RF front ends and ADCs, is proposed and introduced. A key feature of the ACMM is that it allows for all MIMO data streams, this in contrast to regular beamforming. The ACMM IC has been implemented in 65 nm CMOS and operates in the 2.4 GHz band. The control accuracy of the ACMM is 5 bits I and 5 bits Q per matrix element over a 100 MHz band. Measured CIR improvement is 37 dB at an AOA difference of 45°. The ACMM concept has been simulated in Chapter 6, and the substantial performance gain has been confirmed by our test. The measurements confirm that the expected time average power consumption reduction of a MIMO system including an ACMM building block can potentially be over 90%.

Next to MIMO techniques, CR is a method to increase the average data rate. CR achieves this by optimizing the spectral use. The theory in Chapter 6 sows that in wideband CR, analog spatial filtering can achieve similar system throughput as systems without spatial filtering with significantly less quantization bits in the baseband ADC. Simulations show that for realistic indoor scenarios, a CR receiver using analog vector beamforming spatial filtering can achieve similar throughput compared to CR SISO with 4 ADC bits less. Furthermore, simulation indicate that a CR MIMO system with an analog complex matrix multiplier that allows for full MIMO spatial filtering can achieve a similar throughput as a regular CR MIMO system with 3 ADC bit less, corresponding to a power reduction of over 85%. Since ADC power consumption reduces at a rate of an order of magnitude per decade, we think that the algorithms and architectures for spatial filtering can largely contribute to overall system power reduction, and accelerate the introduction of CR in the handheld market.

The ACMM building block proposed in this thesis, exploits the presence of multiple receive antennas and the spatial selectivity of the channel. The overall effectiveness of the ACMM depends on several parameters, such as e.g.:

- The RF bandwidth of the system, which contains desired users and interferers.
- The delay spread of each user and interferer channel, which determines the coherence bandwidth of each channel and thus the effectiveness of a common preconditioning matrix over the relevant part of the RF bandwidth
- The accuracy of the elements of the ACMM over the RF frequency band.
- The number of receiver antenna elements.

We found that, for a 4x4 MIMO system operating in an indoor environment containing the designed 65nm CMOS ACMM IC, overall front end and ADC power consumption can potentially be reduced with an order of magnitude.

7.2 Recommendations

In this thesis we presented an analog MIMO spatial filter. The analog spatial filter increases interference robustness and allows for significant power consumption reduction of wireless receivers. Reducing the power consumption of wireless receivers is of prime importance, since it will be the major bottleneck in the battery lifetime of future mobile devices. In this section we would like to give several recommendations and propose several potential next steps based on this research.

- The decorrelation of the input signals of the MIMO ADCs by the ACMM IC allows for further bit reduction still. In this thesis we have reduced the bits of all the ADCs simultaneously. However, it is also possible to reduce the bits per individual ADC and reduce overall power consumption further. Initial tests on a 4 x 4 MIMO system indicate this can reduce the total number of ADC levels by another 50% while achieving a similar data rate.

- Making the IP3 adaptable to the current channel state can help to vastly reduce the receiver circuit power consumption of MIMO and SISO receivers. The IP3 requirement is a dominant factor in receiver circuit power consumption. A reduction of the IP3 requirement of 20 dB has the potential to reduce receiver circuit power consumption by 30 dB. Currently, IP3 is defined for the worst case in which the receiver should still operate. As such, the IP3 of the receiver is often over dimensioned for what is actually required given the actual channel state.

- The effectiveness of the ACMM can be increased at a cost of more receiver antennas. An increase in receive antennas increases the receiver spatial resolution and thus the accuracy with which interference can be suppressed.

- Large vector beamformers such as are proposed for e.g. the 60 GHz band can increase their data rate by using an ACMM like structure which allows for more than just one data stream. This while still fully benefitting from analog maximum ratio combining.
- The channel matrices of for example large sensor systems tend to have a Wishart distribution. This means that the combined information content of these sensor systems is mainly concentrated in several large Eigenvalues. To capture most information in the digital domain it is therefore not necessary to sample every sensor with an individual ADC. Rather, an ACMM like structure with a reduced number of outputs similar to the number of relevant Eigenvalues with each ACMM output connected to an ADC is in essence sufficient to capture all information in the digital domain.
- To allow for more users per square meter, interference robustness needs to increase. The addition of analog spatial filtering to MIMO systems helps to make those systems more robust to interference. However, the effect on the number of users per square meter that are allowed before interference levels desensitize the entire wireless system have not been investigated.

References

[1] C. E. Shannon, “A Mathematical Theory of Communication,” *The Bell System Technical Journal*, vol. 27, pp. 379–423, 623–656, October 1948.

[2] I. Telatar, “Capacity of Multi-Antenna Gaussian Channels,” *European Transactions on Telecommunications*, vol. 10, pp. 585–595, Nov-Dec 1999.

[3] G. Foschini and M. Gans, “On Limits of Wireless Communications in a Fading Environment When Using Multiple Antennas,” *Wireless Personal Communications*, vol. 6, pp. 233–235, March 1998.

[4] D. Tse and P. Viswanath, *Fundamentals of Wireless Communication*. Cambridge University Press, 2005.

[5] P. Smulders, “Exploiting the 60 GHz Band for Local Wireless Multimedia Acces: Prospects and Future Directions,” *IEEE Communications Magazine*, pp. 140–147, January 2002.

[6] D. Cabric, M. S. Chen, D. A. Sobel, S. Wang, J. Yang, , and R. W. Brodersen, “Novel Radio Architectures for UWB, 60 GHz, and Cognitive Wireless Systems,” *EURASIP Journal on Wireless Communications and Networking, Special Issue on CMOS RF Circuits for Wireless Applications*, vol. 2006, Apr 2006.

[7] B. Razavi, “Challenges in Portable RF Transceiver Design,” *Circuits and Devices Magazine, IEEE*, vol. 12, pp. 12–25, Sep 1996.

[8] A. Stelzer and R. Weigel, "Communication ICs- Market Leaders in Microelectronics," *e & i Elektrotechnik und Informationstechnik*, vol. 118, pp. 481–486, Oct 2001.

[9] P. Baltus and R. Dekker, "Optimizing RF Front Ends for Low Power," *Proceedings of the IEEE*, vol. 88, pp. 1546–1559, Oct 2000.

[10] B. Razavi, "Challenges in the Design of Cognitive Radios," *IEEE 2009 Custom Intergrated Circuits Conference (CICC)*, pp. 391–398, Sept 2009.

[11] B. Razavi, "CMOS RF Receiver Design for Wireless LAN Applications," *Radio and Wireless Conference, 1999. RAWCON 99. 1999 IEEE*, pp. 275 – 280, Aug 1999.

[12] J. Liu and L. Zhong, "Micro Power Management of Active 802.11 Interfaces," *MobiSys08*, June 2008.

[13] R. Krashinsky and H. Balakrishnan, "Minimizing Energy for Wireless Web Access with Bounded Slowdown," *MOBICOM02*, Sep 2002.

[14] J. van den Heuvel, J.-P. Linnartz, and P. Baltus, "Optimizing Throughput for Limited Receiver Circuit Power," *IEEE International Symposium on Circuits and Systems 2010, ISCAS 2010*, May 2010.

[15] J. van den Heuvel, J.-P. Linnartz, and P. Baltus, "Theoretical Model For Maximum Throughput of a Radio Receiver with Limited Battery Power," *31st WIC Symposium on Information Theory in the Benelux,IEEE Benelux Information Theory Chapter and WIC SITB 2010*, May 2010.

[16] J. van den Heuvel, J.-P. Linnartz, and P. Baltus, "Optimal Transmission Rate for Ultra Low-Power Receivers," *21st Annual IEEE International Symposium on Personal, Indoor and Mobile Radio Communications, PIMRC 2010*, Sep 2010.

[17] P. Baltus, *Minimum Power Design of RF Front Ends*. PhD thesis, Eindhoven University of Technology, September 2004. `http://library.tue.nl/catalog/LinkToVubis.csp?DataBib=6:580521`.

[18] J. van den Heuvel and D. Cabric, "Spatial Filtering Approach for Dynamic Range Reduction in Cognitive Radios," *21st Annual IEEE International Symposium on Personal, Indoor and Mobile Radio Communications, PIMRC 2010*, Sep 2010.

[19] B.-U. Klepser, M. Punzenberger, T. Ruhlicke, and M. Zannoth, "5-GHz and 2.4-GHz dual-band RF-transceiver for WLAN 802.11a/b/g applications," in *Radio Frequency Integrated Circuits (RFIC) Symposium, 2003 IEEE*, pp. 37 – 40, Jun 2003.

[20] G. Chien, W. Feng, Y. Hsu, and L. Tse, "A 2.4GHz CMOS transceiver and baseband processor chipset for 802.11b wireless LAN application," in *Solid-State Circuits Conference, 2003. Digest of Technical Papers. ISSCC. 2003 IEEE International*, pp. 358 – 499 vol.1, 2003.

[21] W. Kluge, L. Dathe, R. Jaehne, S. Ehrenreich, and D. Eggert, "A 2.4GHz CMOS transceiver for 802.11b wireless LANs," in *Solid-State Circuits Conference, 2003. Digest of Technical Papers. ISSCC. 2003 IEEE International*, pp. 360 – 361 vol.1, 2003.

[22] K. Vavelidis, I. Vassiliou, T. Georgantas, A. Yamanaka, S. Kavadias, G. Kamoulakos, C. Kapnistis, Y. Kokolakis, A. Kyranas, P. Merakos, I. Bouras, S. Bouras, S. Plevridis, and N. Haralabidis, "A dual-band 5.15-5.35-GHz, 2.4-2.5-GHz 0.18- μm CMOS transceiver for 802.11a/b/g wireless LAN," *Solid-State Circuits, IEEE Journal of*, vol. 39, pp. 1180 – 1184, Jul 2004.

[23] Y.-J. Jung, H. Jeong, E. Song, J. Lee, S.-W. Lee, D. Seo, I. Song, S. Jung, J. Park, D.-K. Jeong, S.-I. Chae, and W. Kim, "A 2.4-GHz 0.25- μm CMOS dual-mode direct-conversion transceiver for bluetooth and 802.11b," *Solid-State Circuits, IEEE Journal of*, vol. 39, pp. 1185 – 1190, Jul 2004.

[24] R. Ahola, A. Aktas, J. Wilson, K. Rao, F. Jonsson, I. Hyyrylainen, A. Brolin, T. Hakala, A. Friman, T. Makiniemi, J. Hanze, M. Sanden, D. Wallner, Y. Guo, T. Lagerstam, L. Noguer, T. Knuuttila, P. Olofsson, and M. Ismail, "A single chip CMOS transceiver for 802.11 a/b/g WLANs," in *Solid-State Circuits Conference, 2004. Digest of Technical Papers. ISSCC. 2004 IEEE International*, pp. 92 – 515, Feb 2004.

[25] L. Perraud, C. Pinatel, M. Recouly, J.-L. Bonnot, N. Sornin, F. Benoist, M. Massei, and O. Gibrat, “A dual-band 802.11a/b/g radio in 0.18 μm CMOS,” in *Solid-State Circuits Conference, 2004. Digest of Technical Papers. ISSCC. 2004 IEEE International*, vol. 1, pp. 94 – 515, Feb 2004.

[26] M. Zargari, M. Terrovitis, S.-M. Jen, B. Kaczynski, M. Lee, M. Mack, S. Mehta, S. Mendis, K. Onodera, H. Samavati, W. Si, K. Singh, A. Tabatabaei, D. Weber, D. Su, and B. Wooley, “A single-chip dual-band tri-mode CMOS transceiver for IEEE 802.11a/b/g wireless LAN,” *Solid-State Circuits, IEEE Journal of*, vol. 39, pp. 2239 – 2249, Dec 2004.

[27] Z. Xu, S. Jiang, Y. Wu, H. yu Jian, G. Chu, K. Ku, P. Wang, N. Tran, Q. Gu, M. zhi Lai, C. Chien, M. Chang, and R. Chow, “A compact dual-band direct-conversion CMOS transceiver for 802.11a/b/g WLAN,” in *Solid-State Circuits Conference, 2005. Digest of Technical Papers. ISSCC. 2005 IEEE International*, vol. 1, pp. 98 – 586, Feb 2005.

[28] S. Mehta, D. Weber, M. Terrovitis, K. Onodera, M. Mack, B. Kaczynski, H. Samavati, S.-M. Jen, W. Si, M. Lee, K. Singh, S. Mendis, P. Husted, N. Zhang, B. McFarland, D. Su, T. Meng, and B. Wooley, “An 802.11g WLAN SoC,” *Solid-State Circuits, IEEE Journal of*, vol. 40, pp. 2483 – 2491, Dec 2005.

[29] O. Charlon, M. Locher, H. Visser, D. Duperray, J. Chen, M. Judson, A. Landesman, C. Hritz, U. Kohlschuetter, Y. Zhang, C. Ramesh, A. Daanen, M. Gao, S. Haas, V. Maheshwari, A. Bury, G. Nitsche, A. Wrzyszcz, W. Redman-White, H. Bonakdar, R. E. Waffaoui, and M. Bracey, “A low-power high-performance SiGe BiCMOS 802.11a/b/g transceiver IC for cellular and bluetooth Co-existence applications,” *Solid-State Circuits, IEEE Journal of*, vol. 41, pp. 1503–1512, Jul 2006.

[30] M. Simon, P. Laaser, V. Filimon, H. Geltinger, D. Friedrich, Y. Raman, and R. Weigel, “An 802.11a/b/g RF Transceiver in an SoC,” in *Solid-State Circuits Conference, 2007. ISSCC 2007. Digest of Technical Papers. IEEE International*, pp. 562–622, Feb 2007.

[31] O. Degani, M. Ruberto, E. Cohen, Y. Eilat, B. Jann, F. Cossoy, N. Telzhensky, T. Maimon, G. Normatov, R. Banin, O. Ashkenazi, A. Ben Bassat, S. Zaguri,

G. Hara, M. Zajac, E. Shaviv, S. Wail, A. Fridman, R. Lin, and S. Gross, "A 1x2 MIMO Multi-Band CMOS Transceiver with an Integrated Front-End in 90nm CMOS for 802.11a/g/n WLAN Applications," in *Solid-State Circuits Conference, 2008. ISSCC 2008. Digest of Technical Papers. IEEE International*, pp. 356 –619, Feb 2008.

[32] L. Nathawad, M. Zargari, H. Samavati, S. Mehta, A. Kheirkhahi, P. Chen, K. Gong, B. Vakili-Amini, J. Hwang, M. Chen, M. Terrovitis, B. Kaczynski, S. Limotyrakis, M. Mack, H. Gan, M. Lee, S. Abdollahi-Alibeik, B. Baytekin, K. Onodera, S. Mendis, A. Chang, S. Jen, D. Su, and B. Wooley, "A Dual-Band CMOS MIMO Radio SoC for IEEE 802.11n Wireless LAN," *Solid-State Circuits Conference, 2008. ISSCC 2008. Digest of Technical Papers. IEEE International*, pp. 358 –619, Feb 2008.

[33] Y.-M. Chiu, T.-M. Chen, P.-Y. Chen, R. Kuan, Y.-C. Shih, Y.-J. Lin, C.-L. Li, Y.-S. Jean, K.-Y. Huang, S.-M. Lin, C.-K. Chien, P.-C. Lin, W.-S. Wang, H.-T. Hsu, M.-C. Huang, C.-H. Lu, H.-J. Shih, K.-U. Chan, and Y.-H. Lin, "A 65nm Low-power CMOS Transceiver for 802.11n Portable Application," *Radio Frequency Integrated Circuits Symposium, 2008. RFIC 2008. IEEE*, pp. 97 –100, Jun 2008.

[34] L. Lin, N. Wongkomet, D. Yu, C.-H. Lin, M. He, B. Nissim, S. Lyuee, P. Yu, T. Sepke, S. Shekarchian, L. Tee, P. Muller, J. Tam, and T. Cho, "A fully integrated 2x2 MIMO dual-band dual- mode direct-conversion CMOS transceiver for WiMAX/WLAN applications," in *Solid-State Circuits Conference - Digest of Technical Papers, 2009. ISSCC 2009. IEEE International*, pp. 416 –417,417a, Feb 2009.

[35] M. Terrovitis, M. Mack, J. Hwang, B. Kaczynski, G. Tseng, B. Wang, S. Mehta, and D. Su, "A 1x1 802.11n WLAN SoC with fully integrated RF front-end utilizing PA linearization," in *ESSCIRC, 2009. ESSCIRC '09. Proceedings of*, pp. 224 –227, Sep 2009.

[36] S. Gross, T. Maimon, F. Cossoy, M. Ruberto, G. Normatov, A. Rivkind, N. Telzhensky, R. Banin, O. Ashckenazi, A. Ben-Bassat, S. Zaguri, G. Hara, M. Zajac, N. Shahar, S. Shahaf, H. Yousef, E. Mor, Y. Eilat, A. Nazimov, Z. Beer, A. Fridman, and O. Degani, "Dual-band CMOS transceiver with

highly integrated front-end for 450Mb/s 802.11n systems," in *Radio Frequency Integrated Circuits Symposium (RFIC), 2010 IEEE*, pp. 431 –434, May 2010.

[37] R. Walden, "Analog-to-Digital Converter Survey and Analysis," *Selected Areas in Communications, IEEE Journal on*, vol. 17, pp. 539–550, Apr 1999.

[38] R. Walden, "Performance trends for analog to digital converters," *Communications Magazine, IEEE*, vol. 37, pp. 96 –101, Feb 1999.

[39] R. Walden, "Analog-to-digital converters and associated ic technologies," in *Compound Semiconductor Integrated Circuits Symposium, 2008. CSIC '08. IEEE*, pp. 1 –2, Oct 2008.

[40] B. Murmann, "LIMITS ON ADC POWER DISSIPATION," in *Analog Circuit Design* (M. Steyaert, J. H. Huijsing, and A. H. van Roermund, eds.), pp. 351–367, Springer Netherlands, 2006.

[41] B. Murmann, "A/D converter trends: Power dissipation, scaling and digitally assisted architectures," in *Custom Integrated Circuits Conference, 2008. CICC 2008. IEEE*, pp. 105 –112, Sep 2008.

[42] B. Murmann, "Trends in Low-Power, Digitally Assisted A/D Conversion," *IEICE Transactions on Electronics*, vol. 93, pp. 718–729, 2010.

[43] B. Murmann, "ADC Performance Survey 1997-2010," *[Online]. Available:* *`http://www.stanford.edu/~murmann/adcsurvey.html`*.

[44] G. E. Moore, "Cramming more components onto integrated circuits, Reprinted from Electronics, volume 38, number 8, April 19, 1965, pp.114 ff.," *Solid-State Circuits Newsletter, IEEE*, vol. 20, pp. 33 –35, Sep 2006.

[45] K. Rupp and S. Selberherr, "The Economic Limit to Moore's Law [Point of View]," *Proceedings of the IEEE*, vol. 98, pp. 351 –353, Mar 2010.

[46] J. Powell, "The Quantum Limit to Moore's Law," *Proceedings of the IEEE*, vol. 96, pp. 1247 –1248, aug 2008.

[47] R. Rietman and J.-P. Linnartz, "Peak restoration in ofdm receiver with clipping a/d converter," *Wireless Communications, IEEE Transactions on*, vol. 7, pp. 5177 –5181, Dec 2008.

[48] T. Schenk, P. Smulders, and E. Fledderus, “Estimation and Compensation of Frequency Selective TX/RX IQ Imbalance in MIMO OFDM systems,” in *Communications, 2006. ICC ’06. IEEE International Conference on*, vol. 1, pp. 251 –256, Jun 2006.

[49] B. Le, T. Rondeau, J. Reed, and C. Bostian, “Analog-to-Digital Converters,” *Signal Processing Magazine, IEEE*, vol. 22, pp. 69–77, Nov 2005.

[50] “The Effects of Adjacent Channel Rejection and Adjacent Channel Interference on 802.11 WLAN Performance,” tech. rep., Texas Instruments White Paper, Nov 2003. [Online]. Available: `http://focus.ti.com/pdfs/bcg/80211_acr_wp.pdf`.

[51] S. Verdú, “Spectral Efficiency in the Wideband Regime,” *IEEE Transactions on Information Theory*, vol. 48, pp. 1319–1343, June 2002.

[52] P. Baltus, “Put your power into SOA LNAs!,” *Workshop on Advances in Analogue Circuit Design*, 1998.

[53] D. Linten, S. Thijs, W. Jeamsaksiri, J. Ramos, A. Mercha, M. Natarajan, P. Wambacq, A. Scholten, and s. Decoutere, “An Integrated 5 GHz Low-Noise Amplifier with 5.5 kV HBM ESD Protection in 90 nm RF CMOS,” *VLSI Circuits, 2005. Digest of Technical Papers. 2005 Symposium on*, pp. 86–89, June 2005.

[54] M. Chen and J. Lin, “A 0.1-20 GHz Low-Power Self-Biased Resistive-Feedback LNA in 90 nm Digital CMOS,” *Microwave and Wireless Components Letters, IEEE*, vol. 16, pp. 323–325, May 2009.

[55] L. Aspemyr, H. Sjoland, H. Jacobsson, M. Bao, and G. Carchon, “A 5.8 GHz 1.7 dB NF Fully Integrated Differential Low Noise Amplifier in CMOS,” *Microwave Conference, 2006. APMC 2006. Asia-Pacific*, pp. 309–312, Dec 2006.

[56] L. Aspemyr, H. Jacobsson, M. Bao, H. Sjoland, M. Ferndahl, and G. Carchon, “A 15 GHz and a 20 GHz Low Noise Amplifier in 90 nm RF-CMOS,” *Silicon Monolithic Integrated Circuits in RF Systems, 2006. Digest of Papers. 2006 Topical Meeting on*, Jan 2006.

[57] E. Cohen, S. Ravid, and D. Ritter, “An Ultra Low Power LNA with 15dB Gain and 4.4dB NF in 90nm CMOS Process for 60 GHz Phase Array Radio,” *Radio Frequency Integrated Circuits Symposium, 2008. RFIC 2008. IEEE*, pp. 61–64, Apr 2008.

[58] D. Linten, X. Sun, S. Thijs, M. Natarajan, A. Mercha, G. Carchon, P. Wambacq, T. Nakaie, and S. Decoutere, “Low-Power Low-Noise Highly ESD Robust LNA, and VCO Design Using Above-IC Inductors,” *Custom Integrated Circuits Conference, 2005. Proceedings of the IEEE 2005*, pp. 497–500, Sep 2005.

[59] D. Linten, S. Thijs, M. Natarajan, P. Wambacq, W. Jeamsaksiri, J. Ramos, A. Mercha, S. Jenei, S. Donnay, and S. Decoutere, “A 5 GHz Fully Integrated ESD-Protected Low-Noise Amplifier in 90 nm RF CMOS,” *Solid-State Circuits Conference, 2004. ESSCIRC 2004. Proceeding of the 30th European*, pp. 291–294, Sep 2004.

[60] D. Linten, L. Aspemyr, W. Jeamsaksiri, J. Ramos, A. Mercha, S. Jenei, S. Thijs, R. Garcia, H. Jacobsson, P. Wambacq, S. Donnay, and S. Decoutere, “Low-Power 5 GHz LNA and VCO in 90 nm RF CMOS,” *VLSI Circuits, 2004. Digest of Technical Papers. 2004 Symposium on*, pp. 372–375, Jun 2004.

[61] S. Pellerano, Y. Palaskas, and K. Soumyanath, “A 64 GHz LNA With 15.5 dB Gain and 6.5 dB NF in 90 nm CMOS,” *Solid-State Circuits, IEEE Journal of*, vol. 43, pp. 1542–1552, Jul 2008.

[62] C. Kienmayer, M. Tiebout, W. Simburger, and A. Scholtz, “A Low-Power Low-Voltage NMOS Bulk-Mixer with 20 GHz Bandwidth in 90 nm CMOS,” *Circuits and Systems, 2004. ISCAS ’04. Proceedings of the 2004 International Symposium on*, vol. 4, pp. 385–388, May 2004.

[63] A. Amer, E. Hegazi, and H. F. Ragaie, “A 90-nm Wideband Merged CMOS LNA and Mixer Exploiting Noise Cancellation,” *Solid-State Circuits, IEEE Journal of*, vol. 42, pp. 323–328, Feb 2007.

[64] S. Peng, C.-C. Chen, and A. Bellaouar, “A Wide-Band Mixer for WCDMA/CDMA2000 in 90nm Digital CMOS Process,” *Radio Frequency integrated Circuits (RFIC) Symposium, 2005. Digest of Papers. 2005 IEEE*, pp. 179–182, Jun 2005.

[65] T. Hui Teo, M. W. G. Y. Annamalai Arasu, and M. Itoh, “A 90nm CMOS Variable-Gain Amplifier and RSSI Design for Wide-Band Wireless Network Application,” *Solid-State Circuits Conference, 2006. ESSCIRC 2006. Proceedings of the 32nd European*, pp. 86–89, Sep 2006.

[66] M. Elmala, B. Carlton, R. Bishop, and K. Soumyanath, “A 1.4V, 13.5mW, 10/100MHz 6th Order Elliptic Filter/VGA with DC-Offset Correction in 90nm CMOS [WLAN Applications],” *Radio Frequency integrated Circuits (RFIC) Symposium, 2005. Digest of Papers. 2005 IEEE*, pp. 189–192, Jun 2005.

[67] N. Stanic, A. Balankutty, P. Kinget, and Y. Tsividis, “A 2.4-GHz ISM-Band Sliding-IF Receiver With a 0.5-V Supply,” *Solid-State Circuits, IEEE Journal of*, vol. 43, pp. 1138–1145, May 2008.

[68] N. Stanic, A. Balankutty, P. Kinget, and Y. Tsividis, “Low-IF 90nm CMOS Receiver for 2.5G Application,” *Electrotechnical Conference, 2004. MELECON 2004. Proceedings of the 12th IEEE Mediterranean*, vol. 1, pp. 151–154, May 2004.

[69] Y. Wang, B. Afshar, T.-Y. Cheng, V. Gaudet, and A. Niknejad, “A 2.5mW Inductorless Wideband VGA with Dual Feedback DC-Offset Correction in 90nm CMOS Technology,” *Radio Frequency Integrated Circuits Symposium, 2008. RFIC 2008. IEEE*, pp. 91–94, Apr 2008.

[70] D. Cabric, I. O’Donnell, M. S.-W. Chen, and R. W. Brodersen, “Spectrum Sharing Radios,” *Circuits and Systems Magazine, IEEE*, vol. 6, p. 30, Jul 2006.

[71] J. van den Heuvel, J.-P. Linnartz, and P. Baltus, “The Effect of RMS Delay Spread on Spatial Filtering,” *32nd WIC Symposium on Information Theory in the Benelux,IEEE Benelux Information Theory Chapter and WIC SITB 2011*, May 2011.

[72] J. van den Heuvel, J.-P. Linnartz, and P. Baltus, “4x4 RF Analog Complex Matrix Multiplier Enables 90% Power Reduction in a MIMO Receiver,” *Solid-State Circuits, IEEE Journal of*, In preporation for resubmission 2011.

[73] J. Warnas, X. Shao, R. Schiphorst, and C. Slump, “MIMO System Setup and Parameter Estimation,” *19th Annual Workshop on Circuits, Systems and Signal Processing, Prorisc 2008*, Nov 2008.

[74] V. Venkateswaran and A.-J. van der Veen, “Analog Beamforming in MIMO Communications With Phase Shift Networks and Online Channel Estimation,” *Signal Processing, IEEE Transactions on*, vol. 58, pp. 4131 –4143, Aug 2010.

[75] W.-B. Chien, C.-K. Yang, and Y.-H. Huang, “Energy-Saving Cooperative Spectrum Sensing Processor for Cognitive Radio System,” *Circuits and Systems I: Regular Papers, IEEE Transactions on*, vol. 58, pp. 711 –723, april 2011.

[76] R. Mahesh and A. Vinod, “A Low-Complexity Flexible Spectrum-Sensing Scheme for Mobile Cognitive Radio Terminals,” *Circuits and Systems II: Express Briefs, IEEE Transactions on*, vol. 58, pp. 371 –375, june 2011.

[77] J. Yang, R. Brodersen, and D. Tse, “Addressing the Dynamic Range Problem in Cognitive Radios,” in *Communications, 2007. ICC ’07. IEEE International Conference on*, pp. 5183 –5188, june 2007.

[78] C. Lelandais-Perrault, T. Petrescu, D. Poulton, P. Duhamel, and J. Oksman, “Wideband, bandpass, and versatile hybrid filter bank a/d conversion for software radio,” *Circuits and Systems I: Regular Papers, IEEE Transactions on*, vol. 56, pp. 1772 –1782, aug. 2009.

[79] B. Razavi, “Design of Millimeter-Wave CMOS Radios: A Tutorial,” *Circuits and Systems I: Regular Papers, IEEE Transactions on*, vol. 56, pp. 4 –16, jan. 2009.

[80] D. Gesbert, H. Bolcskei, D. Gore, and A. Paulraj, “Outdoor MIMO wireless channels: models and performance prediction,” *Communications, IEEE Transactions on*, vol. 50, pp. 1926 – 1934, dec 2002.

[81] H. Hashemi, “The Indoor Radio Propagation Channel,” *Proceedings of the IEEE*, vol. 81, pp. 943–968, July 1993.

[82] G. E. Athanasiadou, A. R. Nix, and J. P. McGeehan, “A Microcellular Ray-Tracing Propagation Model and Evaluation of its Narrow-Band and Wide-Band Predictions,” *IEEE Journal on Selected Areas in Communications*, vol. 18, pp. 322–335, March 2000.

[83] X. Shao and C. H. Slump, “Quantization Effects in OFDM Systems,” *WIC Symposium on Information Theory in the Benelux (IEEE Benelux Information Theory Chapter and WIC SITB 2008)*, May 2008.

[84] X. Shao, R. Schiphorst, and C. H. Slump, “Energy Efficient Error Correction in Mobile TV,” *IEEE International Conference on Communications, ICC 2009*, June 2009.

[85] A. Goldsmith, S. Jafar, N. Jindal, and S. Vishwanath, “Capacity limits of MIMO channels,” *Selected Areas in Communications, IEEE Journal on*, vol. 21, pp. 684 – 702, june 2003.

[86] Y.-C. Liang, A. T. Hoang, and H.-H. Chen, “Cognitive Radio on TV Bands: A New Approach to Provide Wireless Connectivity for Rural Areas,” *Wireless Communications, IEEE*, vol. 15, pp. 16 –22, Jun 2008.

[87] A. Molisch, L. Greenstein, and M. Shafi, “Propagation issues for cognitive radio,” *Proceedings of the IEEE*, vol. 97, pp. 787 –804, May 2009.

[88] J. van den Heuvel, J.-P. Linnartz, P. Baltus, and D. Cabric, “Full MIMO Spatial Filtering Approach for Dynamic Range Reduction in Wideband Cognitive Radios,” *IEEE Transactions on Circuits and Systems I*, Accepted with minor revisions 2011.

List of Publications

Journals

J. van den Heuvel, J.-P. Linnartz, and P. Baltus, “4x4 RF Analog Complex Matrix Multiplier Enables 90% Power Reduction in a MIMO Receiver,” *Solid-State Circuits, IEEE Journal of*, In preporation for resubmission 2011.

J. van den Heuvel, J.-P. Linnartz, P. Baltus, and D. Cabric, “Full MIMO Spatial Filtering Approach for Dynamic Range Reduction in Wideband Cognitive Radios,” *IEEE Transactions on Circuits and Systems I*, Accepted with minor revisions 2011.

J. van den Heuvel, Y. Wu, P. Baltus, and J.-P. Linnartz, “Power Dissipation Minimization and Optimal Transmission Rate for Low-Power RF Receivers,” *IEEE Transactions on Circuits and Systems I*, Planned for submission 2011.

Conference Proceedings

J. van den Heuvel, J.-P. Linnartz, and P. Baltus, “The Effect of RMS Delay Spread on Spatial Filtering,” *32nd WIC Symposium on Information Theory in the Benelux,IEEE Benelux Information Theory Chapter and WIC SITB 2011*, May 2011.

J. van den Heuvel and D. Cabric, "Spatial Filtering Approach for Dynamic Range Reduction in Cognitive Radios," *21st Annual IEEE International Symposium on Personal, Indoor and Mobile Radio Communications, PIMRC 2010*, Sep 2010.

J. van den Heuvel, J.-P. Linnartz, and P. Baltus, "Optimal Transmission Rate for Ultra Low-Power Receivers," *21st Annual IEEE International Symposium on Personal, Indoor and Mobile Radio Communications, PIMRC 2010*, Sep 2010.

P. Baltus, Y. Wu, J. van den Heuvel, and J.-P. Linnartz, "Power Dissipation Minimization in RF Front Ends," *21st Annual IEEE International Symposium on Personal, Indoor and Mobile Radio Communications, PIMRC 2010*, Sep 2010.

J. van den Heuvel, J.-P. Linnartz, and P. Baltus, "Optimizing Throughput for Limited Receiver Circuit Power," *IEEE International Symposium on Circuits and Systems 2010, ISCAS 2010*, May 2010.

J. van den Heuvel, J.-P. Linnartz, and P. Baltus, "Theoretical Model For Maximum Throughput of a Radio Receiver with Limited Battery Power," *31st WIC Symposium on Information Theory in the Benelux,IEEE Benelux Information Theory Chapter and WIC SITB 2010*, May 2010.

J. van den Heuvel, J.-P. Linnartz, P. Baltus, and F. Willems, "A first analysis of MIMO communication as a basis for low power wireless," *3rd IEEE BENELUX/DSP Valley Signal Processing Symposium SPS-DARTS 2007, Antwerp*, Mar 2007.

Summary

Analog MIMO Spatial Filtering

In this thesis we study the potential of MIMO systems as a basis for low power high data rate wireless systems. One of the major benefits of multiple input antennas, is the potential to mitigate interference in the analog domain via analog spatial filtering. Regular MIMO systems handle the interference via additional linearity in the front end, and additional quantization bits in the ADC. By suppressing the interference early in the front end, the required linearity of the front end and the number of ADC bits can be opportunistically reduced. This leads to reduced power consumption of the front end and ADC.

In Chapter 2 it is shown that in the absence of disruptive new technologies, the RF front end and ADC power consumption are the future bottlenecks of MIMO transceivers in terms of extending battery lifetime. Since interference poses strong dynamic range requirements on the front-end and ADC, mitigating the interference has the potential to vastly reduce the power consumption of the ADC and RF front end.

The design considerations of OFDM MIMO systems are studied in Chapter 3. OFDM is a popular modulation scheme due to its ability to cope with extreme channel conditions. A downside of the OFDM modulation scheme is the PAPR. The PAPR of OFDM requires a power back-off in the receiver chain, which reduces the overall system efficiency. Next to the PAPR of OFDM, interferers impose

strong dynamic range requirements on the RF front end and ADC. This, in turn makes the front end and ADC power hungry.

In Chapter 4 the relation between interference and receiver circuit power consumption is formalized. Formalizing this relation is helpful in quantifying the amount of receiver circuit power that can be reduced via interference mitigation. To establish the relation between interference power and receiver circuit power, a closed form analytical solution has been presented which maximizes the throughput efficiency per unit of available receiver circuit power. Via the MTCO all other receiver system specifications such as $IP3$ and F can be derived from the maximized throughput efficiency. Moreover, it is shown that a 20 dB reduction in CIR requirements results in a 30 dB reduction in receiver circuit power consumption. Making the $IP3$ adaptive can therefore substantially improve the power efficiency. Via the limit of the MTCO it is shown that for large SNR the optimal throughput per unit of receiver circuit power approaches 2.3 bits/s/Hz, irrespective of the interference power level. Since in typical applications most energy in mobile devices is consumed by the receiver chain, this result can aid in the design of new standards and wireless networks to extend battery lifetime. Effectively, transmit power is exchanged for receiver circuit power reduction. Furthermore, the results indicate that a duty cycling strategy results in a higher system throughput at low power consumption levels. Interestingly, our analysis can be used as a method to determine whether duty cycling is a good design strategy for low power fixed receivers in a given technology.

In Chapter 5, a MIMO receiver architecture has been introduced which contains a novel ACMM building block. The ACMM building block exploits the spatial selectivity of the MIMO channel in the analog domain to allow for interference mitigation at RF. The ACMM IC has been implemented in 65 nm CMOS and operates in the 2.4 GHz band. To the best of our knowledge the ACMM is the first realization of an analog spatial filtering of interference at RF to alleviate the DR requirements of the receiver and ADC in a MIMO system. The concept of interference suppression at RF has been simulated earlier, and the substantial performance gain have now been confirmed by our test. In contrast to regular beamforming the ACMM allows for all MIMO data streams. The control accuracy of the ACMM is 5 bits I and 5 bits Q per matrix element over a 100 MHz band.

Measured CIR improvement is 37 dB at an AOA difference of 45°. The measurements confirm that the expected average power consumption reduction over time of a MIMO system including an ACMM building block is over 90%.

In a typical CR scenario there are multiple primary and secondary user transmissions over a wide bandwidth, and the desired user only occupies a small portion of the band. The presence of multiple users poses strong dynamic range requirements on the receiver of the CR, making the RF front end and in particular the ADC power hungry. Therefore, undesired user suppression via spatial filtering can relax the CR system requirements. In Chapter 6 DSP algorithms for computation of both vector SIMO beamformer and MIMO spatial filter coefficients are proposed. The focus is on the ADC power consumption and the ADC power reduction is quantified in terms of ADC bit reduction. In Chapter 6 it is shown that in a wideband CR, analog spatial filtering can achieve similar system throughput as systems without spatial filtering with significantly less quantization bits in the baseband ADC.

Simulations show that a receiver using analog vector beamforming spatial filtering can achieve similar throughput compared to SISO with 4 ADC bits less, for realistic indoor scenarios with an SNR of 20 dB and two interferers with an ICR of 40 dB. The 4 bits ADC reduction corresponds to a power reduction of over 90%. Further, simulation indicate that a MIMO system with an analog complex matrix multiplier that allows for full MIMO spatial filtering can achieve a similar throughput as a regular MIMO system with 3 ADC bit less. This corresponds to a power reduction of the MIMO ADCs of over 85%. Since ADC power consumption reduces at a rate of an order of magnitude per decade, we think that the algorithms and architectures for spatial filtering we proposed, can largely contribute to overall system power reduction, and accelerate the introduction of CR in the handheld market.

The ACMM building block proposed in this thesis allows for interference mitigation at RF. The ACMM block exploits the presence of multiple receive antennas and the spatial selectivity of the channel. The overall effectiveness of the ACMM depends on several parameters. One of the parameters is the RF bandwidth of the system, which contains desired users and interferers. Another one is the delay spread of each user and interferer channel, which determines the coherence bandwidth of each channel and thus the effectiveness of a common preconditioning matrix over the relevant part of the RF bandwidth. One more parameter is the accuracy of the elements of the ACMM over the RF frequency band. And finally the number of receiver antenna elements. For a 4x4 MIMO system operating in an indoor environment containing the designed 65nm CMOS ACMM IC, we found that overall front end and ADC power consumption can potentially be reduced with an order of magnitude.

Samenvatting

Analoge MIMO Spatiële Filtering

In dit proefschrift bestuderen we de mogelijkheden van MIMO-systemen als basis voor lage vermogens en hoge data snelheid draadloze systemen. Een van de belangrijkste voordelen van meerdere ontvangst antennes is het potentieel om interferentie te onderdrukken in het analoge domein via analoge spatiële filtering. Normale MIMO systemen gaan met interferentie om door middel van extra lineariteit in de front end en extra quantisatie bits in de ADC. Door het onderdrukken van de interferentie vroeg in het front end, kan de vereiste lineariteit van het front end en het aantal ADC bits opportunistisch worden verminderd, wat weer leidt tot een verminderd stroomverbruik van de front ends en de ADCs.

In hoofdstuk 2 wordt aangetoond dat, bij het uitblijven van ontwrichtende nieuwe technologische ontwikkelingen, het vermogensverbruik van de RF front end en de ADC de toekomstige knelpunten zijn van een verbetering in de batterij levensduur van MIMO transceivers. Omdat interferentie hoge eisen stelt aan het dynamisch bereik van de front end en de ADC, kan het onderdrukken van de interferentie het energieverbruik van de ADC en de RF front end potentieel sterk verminderen.

De ontwerp overwegingen van OFDM MIMO systemen zijn bestudeerd in hoofdstuk 3. OFDM is een populaire modulatie techniek, vanwege zijn vermogen om te kunnen gaan met extreme kanaal omstandigheden. Een nadeel van de OFDM modulatie techniek is de PAPR. Door de PAPR van OFDM is er een power back-

off in de ontvanger keten nodig waardoor de totale systeem efficiëntie verminderd. Naast de PAPR van OFDM, stellen interferers hoge dynamisch bereik eisen aan de RF front end en ADC. Dit verhoogt het vermogensverbruik in de front end en ADC.

In hoofdstuk 4 wordt de relatie tussen interferentie en het vermogensverbruik van het ontvanger circuit geformaliseerd. Het formaliseren van deze relatie is belangrijk voor het kwantificeren van de hoeveelheid ontvanger circuit vermogen dat kan worden verminderd via interferentie onderdrukking. Om de relatie tussen het interferentie vermogen en het vermogensverbruik van het ontvanger circuit vast te stellen, wordt een analytische gesloten vorm oplossing gepresenteerd die de efficiëntie van de throughput maximaliseert per eenheid van het beschikbare ontvanger circuit vermogen. Van de gemaximaliseerde throughput efficiëntie kunnen via de MTCO alle andere ontvanger systeem specificaties zoals $IP3$ en F worden afgeleid. In hoofdstuk 4 wordt aangetoond dat 20 dB vermindering van de CIR eisen resulteert in een 30 dB vermindering van het vermogensverbruik van het ontvanger circuit. Het adaptief maken van de $IP3$ kan dus leiden tot een aanzienlijke verbetering van de vermogensverbruik efficiëntie. Via de limiet van de MTCO kan worden aangetoond dat ongeacht het interferentie vermogen voor grote SNR de optimale throughput per eenheid van het ontvanger circuit vermogensverbruik 2,3 bits/s/Hz benadert. Omdat in typische toepassingen de meeste energie in mobiele apparaten wordt verbruikt door de ontvanger-keten, kan dit helpen bij het ontwerpen van nieuwe standaarden en draadloze netwerken teneinde de levensduur van de batterij te verlengen. Effectief wordt dan zendvermogen uitgewisseld voor ontvanger circuit vermogensverbruik reductie. Verder geven de resultaten aan dat een duty-cycling strategie kan resulteren in een hogere throughput voor lagere vermogensverbruik niveaus. Ook is het interessant dat onze analyse kan worden gebruikt als een methode om te bepalen of duty-cycling van ontvangers, geïmplementeerd in een bepaalde technologie, met een laag vermogensverbruik een goede ontwerp strategie is.

In hoofdstuk 5 wordt een MIMO ontvanger architectuur geïntroduceerd met een nieuwe ACMM bouwsteen. De ACMM bouwsteen onderdrukt interferentie op RF door in het analoge domein gebruik te maken van de spatiële selectiviteit van het MIMO kanaal. Het ACMM IC is geïmplementeerd in 65 nm CMOS en werkt in de 2,4 GHz-band. Voor zover bij ons bekend is het ACMM IC de eerste realisatie van een analoog spatiële filter van interferentie op RF met als doel om de vereiste DR van de ontvanger en ADC in een MIMO-systeem te verminderen. Het concept van interferentie onderdrukking van RF is eerder gesimuleerd en de aanzienlijke prestatie verbetering is bevestigd door onze metingen. In tegenstelling tot reguliere beamforming ondersteunt de ACMM alle MIMO data streams. De aansturing nauwkeurigheid van de ACMM is omgerekend 5 bits I en 5 bits Q per matrix element over een 100 MHz band. De gemeten CIR verbetering is 37 dB bij een AOA verschil van 45°. De metingen bevestigen dat de verwachte gemiddelde vermogensgebruik vermindering van een MIMO systeem inclusief een ACMM bouwsteen over de tijd meer dan 90% is.

In een typisch CR scenario zenden meerdere primaire en secundaire gebruikers over een grote bandbreedte, maar de gewenste gebruiker neemt slechts een klein deel van de band in. De aanwezigheid van meerdere gebruikers stelt sterke DR eisen aan de ontvanger van de CR, waardoor het benodigde vermogensverbruik van de RF front end en in het bijzonder de ADC sterk toeneemt. Daardoor kan het onderdrukken van ongewenste gebruikers door middel van spatiële filtering helpen bij het versoepelen van de CR systeem eisen. In hoofdstuk 6 worden DSP-algoritmes voorgesteld voor de berekening van de coëfficiënten van zowel de vector SIMO beamformer als de MIMO spatiële filter. De focus ligt op het ADC vermogensverbruik. De reductie van het ADC vermogensverbruik wordt gekwantificeerd door middel van de reductie in het aantal ADC bits. In hoofdstuk 6 wordt aangetoond dat in een breedband CR met analoge spatiële filtering een vergelijkbare systeem throughput kan worden bereikt met significant minder bits in de baseband ADC dan in een systeem zonder spatiële filtering.

Simulaties laten zien dat een ontvanger met een analoge vector beamformer als spatieel filter een equivalente throughput kan bereiken in vergelijking tot een SISO met 4 bits minder in de ADC, voor realistische indoor scenario's met een SNR van 20 dB en twee interferers met een ICR van 40 dB. De 4 bits ADC reductie komt overeen met een vermogensreductie van meer dan 90%. Verder geven de simulatie resultaten aan dat een MIMO systeem met een analoge complexe matrix vermenigvuldiger, wat volledige MIMO spatiële filtering mogelijk maakt, een equivalente throughput in vergelijking tot een regulier MIMO systeem kan bereiken met

3 ADC bits minder. Dit komt overeen met een vermogensreductie van de MIMO ADC's van meer dan 85%. Omdat het ADC vermogensverbruik vermindert met een orde van grootte per decennium, denken wij dat de voorgestelde algoritmen en architecturen voor spatiële filtering in belangrijke mate kunnen bijdragen aan de algehele systeem vermogensreductie en dat dit de introductie van CR in de de handheld markt kan versnellen.

De in dit proefschrift voorgestelde ACMM bouwsteen zorgt voor interferentie onderdrukking op RF. Het ACMM blok maakt daarbij gebruik van de aanwezigheid van meerdere ontvangst antennes en de spatiële selectiviteit van het draadloze kanaal. De effectiviteit van de ACMM hangt echter af van verschillende parameters. Een van deze parameters is de RF-bandbreedte van het systeem dat zowel de gewenste gebruikers als de interferers bevat. Een andere parameter is de delay spread van elk gebruiker en elk interferer kanaal. De delay spread bepaalt de correlatie bandbreedte van elk kanaal en daarmee de effectiviteit van een gemeenschappelijke preconditionering matrix over het relevante deel van de RF bandbreedte. Nog een parameter is de nauwkeurigheid van de elementen van de ACMM over de gehele RF frequentieband. De laatste parameter is het aantal antenne elementen van de ontvanger. Voor een 4x4 MIMO systeem met het ontworpen 65nm CMOS ACMM IC werkend in een indoor omgeving, hebben we vastgesteld dat het totale front end en ADC vermogensverbruik potentieel kan worden verminderd met een orde van grootte.

Acknowledgements

Contrary to popular believe most science is not done in isolation. Often scientists are portrayed in popular culture as reclusive and performing their magic in isolation, only for the world to see their final eureka achievement. However, my personal experience while working on this thesis has been very different. I am sure this thesis would not have reached its current form without the support of many people during the past years. Here I would like to thank all those who gave me this opportunity to learn, and who were kind enough to support and provide feedback while I was working on this Ph.D. project. Without them and without the work of other scientists, on whose work I have build, I would never have been able to write this thesis.

Firstly, I would like to thank my two promotors prof.dr.ir. Peter Baltus and prof.dr.ir Jean-Paul Linnartz for giving me the opportunity to do my Ph.D. research. When I first met Peter I was a blank slate when it comes to RF design. The stories Peter told me in our first meetings captured my imagination and I knew then I wanted to learn more about RF design. Back then we were sitting in opposite offices in a hallway at Philips Research were I was conducting my M.Sc thesis. To my personal delight Peter gave me the opportunity to do my Ph.D. under his supervision and it has been a partnership I have enjoyed very much ever since. Peter, you are an excellent supervisor and I really enjoyed working with you very much. You have been very supportive and your door was always open for me when I needed help or guidance. I am also truly grateful to my second promotor prof.dr.ir Jean-Paul Linnartz. I was conducting my M.Sc thesis in his group at Philips Research. Jean-Paul, you have always been very constructive, very helpful, friendly and an outstanding supervisor. Your technical knowledge

and feedback have always been excellent and inspiring. You have been very supportive throughout my Ph.D. and have helped me on many occasions far beyond what can normally be expected from a supervisor. Therefore, I am very grateful and happy that both you and Peter were my supervisors. Personally, I do not think I could have wished for two better supervisors.

Furthermore, I wish to thank prof.dr.ir Arthur van Roermund for the opportunity to conduct my Ph.D. within the MsM group and for giving me the trust to learn RF design. Thank you for your constructive and positive feedback over the past years and thank you for your efforts in creating a cosy atmosphere in the MsM group. Very often your office light was the first one burning and one of the last to go out. During the past years I have often wondered how you combined all your different tasks while you were running in the hallway and answering emails at crazy hours. I will never forget our dinner in France during a conference were I convinced the French waiter to bring me the vegetarian menu.

I would like to thank prof.dr.ir. Liesbet van der Perre and prof.dr.ir Bram Nauta for being a committee member. Thank you very much for your time and effort. Furthermore, I would like to thank the dean prof.dr.ir. Ton Backx for the permission of my Ph.D. promotion.

I wish to thank all the members of the MIMO in a Mass Market project team and the people involved in organizing the project such as Fred Snijders and Job Oostveen. I also wish to thank prof.dr.ir. Kees Slump, Xiaoying Shao and Harm Cronie from the SAS group of the University of Twente. Kees, you have been very supportive enthusiastic and stimulating during the project. You were especially helpful when we needed to order the PCB and when we needed to arrange progress meetings. I would also like to thank the people from the SPS group of the Eindhoven University of Technology and in particular prof.dr.ir. Jan Bergmans, Frans Willems, Wu Yan, and Peng Zang. Especially the discussions with Frans Willems have been very instrumental in formulating my ideas about information theory. I also wish to thank prof.dr.ir. Alle-Jan van der Veen and Vijay Venkateswaran from the Circuits and Systems group of the Delft University of Technology for their insights into MIMO signal processing and their very helpful and useful conversations. The discussions I had with Vijay have always been very stimulating

and fruitful.

I want to thank all members and students of the MsM group, for the discussions and the friendly atmosphere. The positive and friendly atmosphere in the group have been very helpful during my Ph.D. I want to thank Margot van den Heuvel and Piet Klessen. Not only do Margot and I share the same family name, we also share the same birthday. This little fact has caused quite some confusion among senders of mail during the past few years. Luckily, now there is a student who shares my name for people to send mail to. Dear Margot, I have often wondered how you managed to administer the agendas of both Arthur and Peter. The word magic comes to mind. Dear Piet, I am very grateful for your positive attitude and your hands on help in the lab and your great help with Cadence problems. I do not think I could have managed without you. I wish to thank Charl Linssen and Zhe Chen for their excellent work under my supervision. Charl, your work on the LNA board was excellent and I was pleasantly surprised with your help on the ACMM board. You did much more than what Peter and I thought was to be expected from a student. The work you put in easily shaved months of my Ph.D. and I thank you for that. Dear Zhe Chen, you worked hard and focused and showed excellent research skills and broad electrical engineering knowledge. You managed to do a difficult task in a short time frame while getting familiar with the circuits and systems. Without your input I would not have been able to solve those issues during my Ph.D. Furthermore, I would like to thank my office mates Xia Li, Hao Gao and Yi Wang for the friendly atmosphere in our office and the many discussions. I really enjoyed our office diners. Especially Xia, your artwork has been a source of wonder and entertainment for me and I enjoyed your creations very much. I also want to thank Hans Hegt and Eugenio Cantatore for your supportive attitude and helpful feedback during the past years. Furthermore, I would like to thank all the members of the MsM group and the CWTe, Dusan Milosevic, Reza Mahmoudi, Jan Haagh, Pieter Harpe, Georgi Radulov, Pooyan Sakian Dezfuli, Wei Deng, Yikun Yu, Hammad M. Cheema, Erwin Janssen, Maarten Lont, Yu Lin, Mehdi Sarkeshi, Jaap Essing, Foad Arfei Malakzadeh, Chuang Lu, Elbert Bechthum and so on. Dear Piet, Margot, Reza, Jan, Hans, etc. I really enjoyed our daily coffee breaks and the many discussions away from science. Thank you for making me feel at home in the University.

I would like to thank all my former colleagues from the Philips Research CoSiNe Group who have been instrumental in shaping my views about signal processing. I especially wish to thank Ronald Rietman without whom I probably would not have started a Ph.D. Ronald was my supervisor during my M.Sc and gave me the courage and the encouragement to pursue a Ph.D. Furthermore, Ronald also acted as a daily supervisor during the first months of my Ph.D. I can sincerely say I learned more about research and electrical engineering in those years from you and the colleagues in the CoSiNe group than I did in the four years before. Therefore I wish to thank all the members in the CoSiNe group who created that friendly, supportive and learning atmosphere, Maurice Draaijer, Tim Schenk, Yvonne Lansink-Stroeve, Ludo Tolhuizen, Maurice Stassen, Joop Talstra, Hongming Yang, Xiangyu Wang, Stan Baggen, Semih Serbetli, Peter Rutten, Eric Penning de Vries, Lorenzo Feri, Alessio Felippi, Yonggang Du, Dee Denteneer, Sri Andari Husen, Luc Tan an so on. Thank you for making me feel at home and for the discussions during lunch time. Tim, the book you gave me at the start of my Ph.D. proved to be very helpful the past years. Special thanks go to Peter Rutten for supervising Char Linssen while he was within MiPlaza. Peter your input was very constructive and helpful.

I also wish to thank all the members of the ESSI group of Philips Research for support during tapeout and PCB design and for making me feel welcome in your group. I want to thank Lennart Yseboodt for his help during the PCB design. Furthermore, I wish to thank Henry van der Zanden for his help in layouting and debugging of the circuits. I also wish to thank Bob Theunissen for his support during tapeouts and his advice during design reviews. I also want to thank Marleen Duizer-Heijmans for arranging meetings and for her support. Furthermore, I wish to thank Hugo Veenstra for his constructive feedback and raising valid questions. I enjoyed my stay in the ESSI group and the discussions during lunch and coffee breaks. Moreover, I would like to thank Nienke Bruinsma of Philips Research for her creative help in bonding the IC to the PCB.

I would like to thank prof. Danijela Čabrić for allowing me to spend several months in her Cores group at the University of California, Los Angeles. Danijela, I always looked forward to our weekly discussions. You were very positive and supportive even long after I left your group. I really enjoyed working together with you.

Moreover, I wish to thank all the members of the Cores group for their positive attitude and for making me feel welcome and at home for this period, Paulo Isagani Urriza, Jung-Mao Lin, Jun Wang, Przemyslaw Pawelczak, Jihoon Park, Tsung-Han Yu, Jared Dulmage, Oussama Sekkat, Kun Zeng, Wesam Gabran, Alican Gök, Lucas Araki, Pål Grønsund, and so on. The lunches with you and Shaunak Joshi were always a delight.

I am grateful to the WATS team at IMEC for offering me a job on the basis of this work. I would like to thank the current team members who make me feel at home and have a positive attitude, Hans Pflug, Jac Romme, Xiaoyan Wang, Georgios Selimis, Yao-Hong Liu, Yan Zhang, Nauman Kiyani, Alex Young, Victor van Acht, Benjamin Busze, Cui Zhou, Kathleen Philips, Maja Vidojkovic, Li Huang, Coby Huang, Ming Ding, Ao Ba, Mario Konijnenburg, Christian Bachmann, Guido Dolmans, Martijn Hijdra, Jef van de Molengraft, Lindsay Brown, Siebren Schaafsma, Harmke de Groot, Huib Visser, and so on.

I would also like to thank all my friends who have distracted me from work an helped me relax, Christian Brands, Vincent Almering, Arnout van den Bosch, Pieter van den Akker, Sven Stringer, Jorg van Orsouw, Michel van Eerd, and so on. Michel thank you for your help with the interface PCB for my measurements. I also wish to thank all my friends at the rowing club for their support and friendship, Tom van Rijsewijk, Basjan Schouwenaars, Bert Knegtering, Tom Corstjens, Boudewijn Deurloo, Teun Lijnkamp, Floor Luub, and so on. I also want to thank my former house mates for their support over the years, Daan Alberga, Frank van de Sande, Annet Aarts, and so on.

Many thanks go to my entire family. Special thanks go to my parents, sister and grandmother who have supported me throughout my studies. Also I wish to thank my uncle Theo who had the patience to listen to "my new inventions" when I was a kid.

Finally, I would like to thank Petra for sharing our lives, for supporting me throughout, and for working together on this thesis.

Biography

Johannes H.C. van den Heuvel was born on Febuary 5th 1981 in Oss, the Netherlands. He received his Ir. and M.Sc. degree in Electrical Engineering, from the Eindhoven University of Technology, the Netherlands, in 2006. In 2007 he started working towards the Ph.D. degree at the Eindhoven University of Technology, where he was a member of the Mixed-signal Microelectronics group. Since april 2011 he moved to IMEC-NL. There he is working as a wireless research scientist. His current research interests include low-power and high-speed mixed signal circuits and architectures, multiple antennas system implementations, and digital baseband algorithms.